



**Technische Universität München**

Wissenschaftszentrum Weihenstephan für Ernährung, Landnutzung und Umwelt  
Experimentelle Radioonkologie und Strahlentherapie

**The cellular responses  
to focused low LET proton irradiation  
in comparison to high LET irradiation**

Katarina Ilicic

Vollständiger Abdruck der von der Fakultät Wissenschaftszentrum Weihenstephan für Ernährung, Landnutzung und Umwelt der Technischen Universität München zur Erlangung des akademischen Grades eines  
**Doktors der Naturwissenschaften**  
genehmigten Dissertation.

Vorsitzender: Prof. Dr. Johann J. Hauner

Prüfer der Dissertation:

1. Prof. Dr. Gabriele Multhoff
2. Prof. Angelika Schnieke, Ph.D.

Die Dissertation wurde am 20.12.2017 bei der Technischen Universität München eingereicht und durch die Fakultät Wissenschaftszentrum Weihenstephan für Ernährung, Landnutzung und Umwelt am 21.03.2018 angenommen.



## Abstract

The clinical use of high linear energy transfer (LET) particles in radiotherapy offers many benefits in comparison to conventional photon radiotherapy, particularly due to an enhanced biological effect, which is often expressed as the relative biological effectiveness (RBE). This increased RBE of high LET radiation is attributed mostly to their highly inhomogeneous dose deposition, which leads to the formation of complex DNA damage which is difficult for the cell to repair. In comparison, a quasi-homogeneous DNA damage induced by low LET particles can be easily repaired. This work gives new insight into the dependence of the RBE on spatial dose distribution and thus LET.

The effects of different spatial dose and DNA damage distributions on the RBE was analyzed with respect to biological endpoints of cell survival, induction of apoptosis and DNA double strand break (DSB) repair. For this purpose, Chinese hamster ovary (CHO-K1) cells were irradiated using a unique experimental approach at the ion microbeam SNAKE with low LET protons and high LET lithium and carbon ions. The cells were exposed either to a grid-like irradiation pattern (with pattern width of 3.8  $\mu\text{m}$ , 5.4  $\mu\text{m}$ , 7.6  $\mu\text{m}$  and 10.8  $\mu\text{m}$ ) where a certain number of particles were focused to sub-micrometer spots or to a homogeneous particle irradiation. The mean dose was the same in all irradiation patterns, only the spatial dose distribution was varied. For each particle type the RBE values for the cell survival were calculated and experimental cell survival data were compared with the predictions obtained from the biophysical local effect model (LEM).

The experiments demonstrated novel evidence that focusing of low LET protons to sub-micrometer spots result in a significant increase in RBE for the cell survival similar to that observed with high LET particles. DNA damage repair after grid-like focused irradiation is hypothesized to result in more lethal chromosome aberrations, and thus decreased cell survival. This decrease in cell survival is presumed to be due to an increased local density of DSBs caused by focused dose deposition. The importance of the interaction of DSBs on the micrometer scale was herewith confirmed. Additionally, the exposure of cells to a grid-like irradiation pattern of high LET lithium or carbon ions resulted in an increased RBE as compared to the focused low LET protons. These results demonstrated the importance of DNA damage distribution on the nanometer scale, since the single strand breaks (SSBs) induced in close proximity (nm) to one

another lead to the formation of additional DSBs. Moreover, the experimental data were in a good agreement with the LEM calculations, and support the existence of different spatial scales of DNA damage. A higher fraction of the residual unrepaired DSBs was found by measuring the mean  $\gamma$ -H2AX fluorescence intensity after focused proton irradiation as compared to homogeneous proton irradiation. This result indicated that a focused dose deposition may induce more complex DNA damage, which is more difficult to repair and thus more harmful to cells. Additionally, the results from this work with respect to the apoptosis induction suggested that changing spatial dose distribution by focusing low LET protons might efficiently trigger an early apoptotic response and an overall higher apoptotic rate as compared to a homogeneous irradiation.

In conclusion, the results have shown that a sub-micrometer focused proton deposition is significantly more efficient than a homogeneous dose application with respect to cell killing, the induction of apoptosis and the formation of complex DNA damage. The results of this work present novel evidence that the increased RBE of high LET particles can be approached by spot application of low LET protons.

## Contents

<b>1. Introduction</b> .....	1
1.1 Motivation .....	1
1.2 Physical characteristics of charged particle radiation .....	4
1.2.1 Dose deposition of photons and charged particles.....	5
1.2.2 Linear energy transfer (LET) .....	6
1.2.3 Radial dose distribution and track structure.....	7
1.3 Biological effects of ionizing radiation .....	9
1.3.1 Ionizing radiation induced DNA damage .....	9
1.3.2 DNA damage repair .....	12
1.3.3 DNA damage induced apoptosis.....	13
1.3.4 Cell survival .....	14
1.4 Relative biological effectiveness (RBE) and its characteristics .....	16
1.5 Local Effect Model (LEM).....	18
<b>2. Materials and Methods</b> .....	21
2.1. Cell culture: Chinese Hamster Ovary cells CHO-K1 .....	21
2.2. Cell cultivation on a well-defined restricted area.....	22
2.3. Cell irradiation.....	24
2.3.1. Reference irradiation with X-rays .....	24
2.3.2. Particle irradiation at the ion microbeam SNAKE .....	25
2.3.3. Geometrical measurement of cell nucleus area for calculation of the hit statistics.	27
2.4. DNA DSB repair .....	28
2.4.1. Immunofluorescence staining of $\gamma$ -H2AX.....	28
2.4.2. $\gamma$ -H2AX repair kinetics measured by flow cytometry.....	29

2.5. Analysis of caspase 3/7 activity using flow cytometry .....	30
2.6. Modified colony forming assay for cell irradiation at SNAKE .....	32
2.6.1. Statistical analysis of cell survival .....	33
2.6.2. RBE calculation for cell survival .....	34
<b>3. Results</b> .....	<b>35</b>
3.1. Hit statistics .....	35
3.2. Analysis of DNA DSB repair after microbeam particle irradiation at SNAKE.....	37
3.2.1. Immunofluorescence staining of $\gamma$ -H2AX.....	37
3.2.1.1. Flow cytometric analysis of $\gamma$ -H2AX repair kinetics.....	39
3.2.1.2. Effects of focused low LET proton irradiation on $\gamma$ -H2AX repair kinetics	39
3.2.1.3. Effects of high LET carbon ion irradiation on $\gamma$ -H2AX repair kinetics .....	41
3.3. Analysis of radiation induced apoptosis by flow cytometric measurement of Caspase 3/7 activity .....	43
3.3.1. Measurement of Caspase 3/7 activity after X-ray irradiation .....	44
3.3.2. Measurement of Caspase 3/7 activity after irradiation with 20 MeV protons .....	46
3.3.3. Measurement of Caspase 3/7 activity after irradiation with 55 MeV carbon ions ..	48
3.3.4. Comparison of measured apoptosis induction using different radiation qualities ..	49
3.4. Clonogenic cell survival .....	50
3.4.1. Dose response curve with X- rays .....	51
3.4.2. Microbeam particle irradiation at SNAKE.....	52
3.4.2.1. Proton irradiation .....	53
3.4.2.2. Lithium ion irradiation .....	54
3.4.2.3. Carbon ion irradiation .....	55
3.4.2.4. Determination of the RBE for cell survival .....	56
3.4.2.5. LEM prediction in comparison to experimental data.....	58
<b>4. Discussion</b> .....	<b>61</b>

4.1. Increased RBE for cell survival after focused particle irradiation .....	61
4.1.1. Influence of the nuclear size distribution on the cell survival .....	63
4.1.2. Comparison of experimental cell survival data with LEM predictions.....	64
4.2. DNA DSB repair after low LET proton irradiation and high LET carbon ion irradiation	66
4.3. Induction of apoptosis in cells using microbeam particle irradiation.....	69
<b>5. Conclusion and Outlook.....</b>	<b>75</b>
Bibliography .....	77
List of publications .....	87
Appendix .....	91
Acknowledgments .....	93
Curriculum vitae.....	95





## List of Abbreviations

Alt-EJ	Alternative end-joining
CHO-K1	Chinese hamster ovary cells
DAPI	4',6-diamidino-2-phenylindole
DNA	Deoxyribonucleic acid
DSB	Double strand break
FI	Fluorescence intensity
HR	Homologous recombination
LEM	Local effect model
LET	Linear energy transfer
NHEJ	Non-homologous end-joining
PE	Plating efficiency
RBE	Relative biological effectiveness
SNAKE	Superconducting nanoprobes for applied nuclear physics experiments
SSB	Single strand break
$\gamma$ -H2AX	Phosphorylated form of the histone H2AX



## List of Figures

Figure 1.1: The distribution of dose after irradiation with focused high LET carbon ions, randomly applied low LET protons and focused low LET protons.....	3
Figure 1.2: Microdose distribution after irradiation with focused high LET carbon ions, randomly applied low LET protons and focused low LET protons.....	4
Figure 1.3: Depth-dose profiles of 21 MeV photons, 148 MeV/u protons and 270 MeV/u carbon ions. ....	5
Figure 1.4: Linear energy transfer (LET) as a function of particle energy for different ions..	7
Figure 1.5: Simulation of $\delta$ - electron emission by 1 MeV protons and 1 MeV/u carbon ions..	8
Figure 1.6: Schematic figure of two DNA strands and examples of radiation induced DNA damage lesions. ....	10
Figure 1.7: RBE dependence with differing LETs.....	18
Figure 2.1: Adherent CHO-K1 cells in culture flask. ....	21
Figure 2.2: Cell cultivation setup used for irradiation experiments at SNAKE.....	22
Figure 2.3: Stitched microscope image of CHO-K1 cells stained with DAPI.....	23
Figure 2.4: Experimental setup for X-ray irradiation of cells seeded on Mylar foil in cell containers used for SNAKE microbeam irradiation. ....	24
Figure 2.5: Set-up of the ion microprobe SNAKE at the Munich tandem accelerator.....	25
Figure 2.6: $\gamma$ -H2AX fluorescence intensity histograms of unirradiated and proton irradiated cells. ....	30
Figure 2.7: Dot plot representation of data obtained after irradiation using Caspase 3/7 and SYTOX cell staining.....	31
Figure 3.1: Nuclear size distribution of CHO-K1 cells.....	35
Figure 3.2: Distribution of number of hits using different grid pattern in CHO-K1 cells..	36
Figure 3.3: $\gamma$ -H2AX immunofluorescence staining after exposure to quasi-homogeneous and focused MeV protons. ....	38
Figure 3.4: The relative mean $\gamma$ -H2AX fluorescence intensity after quasi-homogeneous and focused proton irradiation. ....	40

Figure 3.5: The ratio of the relative mean $\gamma$ -H2AX fluorescence intensity of focused to homogeneous proton irradiation. ....	41
Figure 3.6: Time-dependence of $\gamma$ -H2AX fluorescence intensity after focused carbon ion irradiation. ....	42
Figure 3.7: Biphasic repair kinetics of CHO-K1 cells after carbon ion radiation.....	43
Figure 3.8: Percentage of caspase 3/7 positive, double positive and SYTOX positive cells at different time points after X-Ray irradiation.. ....	44
Figure 3.9: Relative percentage of caspase 3/7 positive, double positive and SYTOX positive cells at different time points after X-Ray irradiation. ....	45
Figure 3.10: Percentage of caspase 3/7 positive, double positive and SYTOX positive cells after irradiation with 20 MeV protons.....	46
Figure 3.11: Relative percentage of caspase 3/7 positive, double positive and SYTOX positive cells after irradiation with 20 MeV protons.....	47
Figure 3.12: Percentage of caspase 3/7 positive, double positive and SYTOX positive cells after irradiation with 55 MeV carbon ions. ....	48
Figure 3.13: Relative percentage of caspase 3/7 positive, double positive and SYTOX positive cells after irradiation with 55 MeV carbon ions. ....	49
Figure 3.14: Comparison of the relative percentage of caspase 3/7 positive, double positive and SYTOX positive cells after irradiation with a mean radiation dose of 3.4 Gy using different radiation qualities. ....	50
Figure 3.15: Dose-response cell survival curves after X-Ray irradiation. ....	51
Figure 3.16: Cell survival after exposure to quasi-homogeneous and focused 20 MeV protons ..	54
Figure 3.17: Cell survival after exposure to quasi-homogeneous and focused 33 MeV lithium ions .....	55
Figure 3.18: Cell survival after exposure to focused 55 MeV carbon ions.....	56
Figure 3.19: RBE values for cell survival after exposure to protons, lithium ions and focused carbon ions .....	58
Figure 3.20: Comparison of experimental vs. LEM prediction cell survival data .....	60

## List of Tables

Table 2.1: Overview of all applied particles used in SNAKE experiments and all irradiation modalities .....	27
Table 3.1: Overview of grid pattern used in the microbeam irradiation experiments at SNAKE with corresponding hit statistics.....	37
Table 3.2: Calculated linear-quadratic parameters of the dose- response cell survival curve for CHO-K1 cells.....	52
Table 3.3: Overview of grid pattern used in the microbeam irradiation experiments at SNAKE with detailed information on the number of particles per point (ppp), spot LET and the applied dose to the cell nucleus.....	53
Table 3.4: Calculated cell survival, equivalent dose of the reference radiation and RBE values for the microbeam particle radiation at SNAKE.....	57



# **1. Introduction**

## **1.1 Motivation**

Today, approximately 50 % of all cancer patients are treated with radiotherapy, mostly with X-rays, which are produced by linear accelerators (Durante, 2010). The main aim of radiotherapy is to destroy tumor cells by applying a high dose of radiation to the tumor whilst sparing the surrounding normal tissue. Technological innovations in the past several years could have improved clinical outcome. For instance, intensity-modulated radiotherapy (IMRT) is a technique which utilizes several radiation beams of inconsistent intensities in order to improve the conformation of radiation doses to the tumor, while sparing adjacent normal tissue (Cheung, 2006; Taylor and Powell, 2004). Moreover, the integration of advanced imaging techniques into the radiation treatment has led to increased precision and accuracy of radiation delivery (Jaffray, 2012). However, a selective dose application only to the tumor is not feasible using X-rays due to their physical characteristics. The surrounding healthy tissue will always be exposed to radiation, thus increasing the probability of normal tissue complications (Loeffler, 2013). Consequently, the applicable maximal radiation dose used for the treatment is limited. In general, cells in the normal tissue have the capacity to repair radiation-induced DNA damage more efficiently than tumor cells, in particular because frequently occurring mutations in tumor cells prevent them from undergoing efficient DNA damage repair and aid the propagation of the tumor. In order to better spare the surrounding healthy tissue, fractionation of the total radiation dose is required. In the case of fractionated radiotherapy, the total radiation dose has to be divided into several, smaller doses over a period of time in order to allow the normal tissue cells to repair sub-lethal DNA damage.

The radiological application of charged particle beams such as heavy ions or protons was first proposed by Charles Wilson in 1946 in order to overcome the biological as well as physical restrictions of conventional radiotherapy using X-rays (Kraft, 2000; Schardt, 2010; Wilson, 1946). Charged particles offer many advantages compared to the radiotherapy with X-rays due to a fundamental difference in their physical properties. In contrast to conventional radiotherapy with X-rays, charged particles deposit doses required for tumor control very precisely within the tumor site and better spare the surrounding healthy tissue, inducing less unwanted side effects

(Durante, 2010; Loeffler, 2013). Therefore, radiotherapy with charged particles is expected to improve clinical outcome by an improved prevention of treatment-related side effects as well as a lower induction rate of secondary tumors, which is especially important in paediatric oncology (Combs *et al.*, 2009).

Furthermore, heavy ions e.g. carbon ions, which have a high linear energy transfer (LET), have additional biological advantages over X-rays and protons due to the increased ionization density at the end of the particle range. The higher biological effectiveness of high LET radiation is attributed particularly to the non-homogeneous energy deposition, which is highly concentrated around the particle track and provides very high local doses. The dose deposition of low LET particles, e.g. protons, however is spread more uniformly and local doses are moderate. High LET radiation therefore requires a lower dose to induce the same biological responses as low LET radiation would. Furthermore, several biological advantages such as a diminished DNA damage repair capacity of irradiated cells, decreased oxygen enhancement ratio and reduced cell cycle-dependent radiosensitivity have been proposed for high LET radiation (Ohno, 2013). These advantages make carbon ions more effective in radiotherapy cancer treatment than photons or protons (Ohno, 2013).

The present work is performed as part of the BMBF funded "LET Verbund" which aims to contribute to a better understanding of the high relative biological effectiveness (RBE) of heavy ions. The microbeam particle irradiation at SNAKE was used in this work as an experimental approach to change the dose and DNA damage distribution. In this approach low LET protons have been applied to cells either randomly or focused to sub-micrometer spots, thus emulating the dose deposition of heavy ions such as carbon ions. Figure 1.1 represents a simulation of the dose deposition from irradiation patterns used in this study: high LET 55 MeV carbon ions which were applied in the (5.4 x 5.4)  $\mu\text{m}^2$  grid pattern (Figure 1.1 (a)), randomly distributed low LET 20 MeV protons (Figure 1.1 (b)) and 117 focused 20 MeV protons applied in the same grid pattern as carbon ions (Figure 1.1 (c)). For all three irradiation types the mean radiation dose of 1.7 Gy was applied.



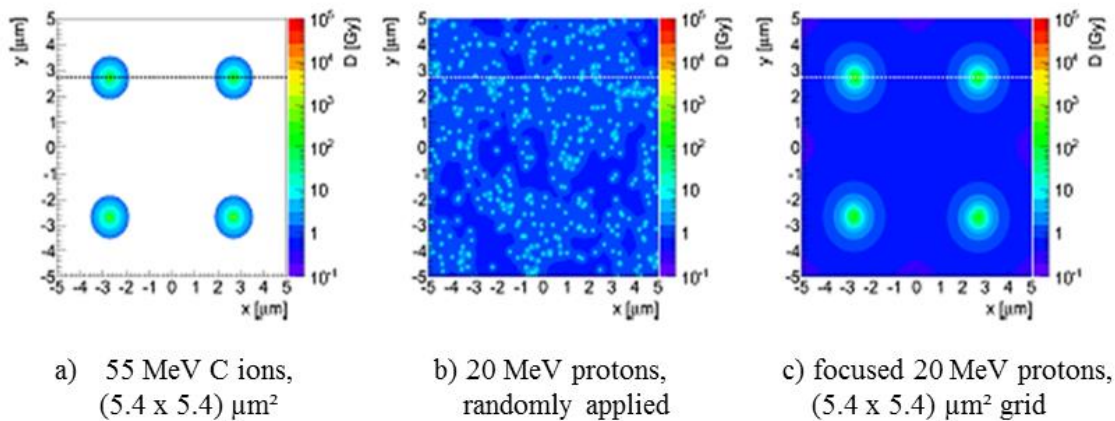


**Figure 1.1:** Simulation of two dimensional dose distribution after irradiation with 1.7 Gy of one 55 MeV carbon ion in the  $(5.4 \times 5.4) \mu\text{m}^2$  grid (a), randomly applied 20 MeV protons (b) and 117 focused protons in the same  $(5.4 \times 5.4) \mu\text{m}^2$  grid (Courtesy of Christoph Greubel).

Figure 1.2 shows the difference in the micro dose distribution along the dashed line in Figure 1.1. The dose distribution of focused proton irradiation differs from that of randomly applied protons and its macro structure looks similar to the dose distribution of the focused carbon ion irradiation. This simulation shows that by focusing low LET protons the dose deposition can be spatially concentrated and locally elevated as can be observed in the case of high LET radiation.

The dependence of the radiation effectiveness from different spatial dose depositions was investigated with respect to the biological endpoints of clonogenic cell survival, DNA DSB repair and apoptosis induction. Additionally, the experimental cell survival data have been compared with the predictions obtained using the Local Effect Model (LEM) model, which was calculated by the collaborators Dr. Michael Scholz and Dr. Thomas Friedrich from the Department of Biophysics at GSI (Helmholtz Center for Heavy Ion Research) in Darmstadt. The comparison of the measured cell survival data with the model predictions will contribute to a better insight into biological effects of different spatial distributions of DNA damage. Furthermore, precise knowledge about the relation between the RBE and dose distribution could help to improve radiotherapy with protons and heavy ions.

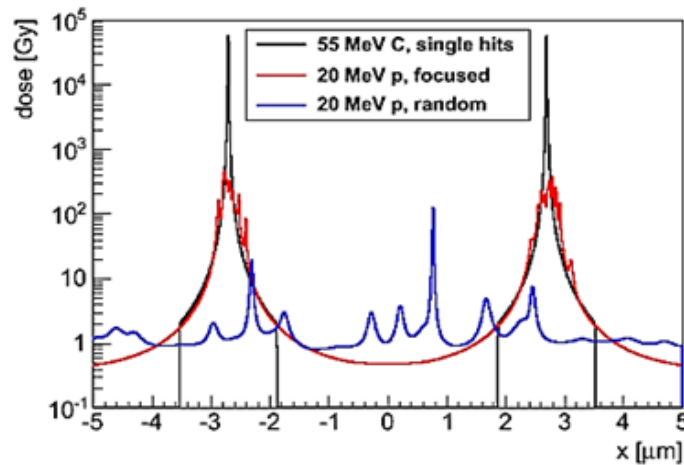


**Figure 1.2:** Microdose distribution along the dashed line through a cell nucleus after applying the same average dose of 1.7 Gy by randomly distributed 20 MeV protons, a grid-like irradiation with 55 MeV carbon ions and 117 focused protons using the same grid pattern as in the case of carbon ions (Courtesy of Christoph Greubel).

The following sections of this chapter give an overview on the physical and biological backgrounds relevant for this work. Sections 1.2 and 1.3 describe how charged particles interact with biological matter as well as the occurring biological effects, with a special focus on the DNA damage, DNA repair, apoptosis induction and the most relevant endpoint of cell survival. In Sections 1.4 and 1.5, the relative biological effectiveness and the biophysical model LEM are described in more detail.

## 1.2 Physical characteristics of charged particle radiation

There are two classes of ionizing radiation which can be applied in radiotherapy: electromagnetic radiation (i.e. photons), such as X-rays and  $\gamma$ -rays and charged particles, such as protons and heavier ions. Tissue damage is induced either directly by particles itself or by secondary electrons generated from interactions of the primary beam with matter (Scholz, 2003). The absorbed dose quantifies the energy absorption in matter caused by ionizing radiation. It is given as the energy deposited per unit mass in a target material with unit Gray ( $1\text{Gy} = 1\text{J/kg}$ ).

The local dose distribution, which is given by particles ionization density, differs among the particles themselves due to their energy and velocity. These differences in the spatial dose deposition are mainly responsible for their distinct biological effects and will be further described in the following sections.

### 1.2.1 Dose deposition of photons and charged particles

Photons at low energies interact with matter by photoelectric, Compton or pair-production processes resulting in an exponentially decreased absorbed dose with penetration depth. The dose profile of photons with higher energy shows a maximum dose, which is shifted to deeper depth (build-up effect) followed by an exponentially decreasing dose as can be seen for 21 MeV photons in Figure 1.3. Contrary to photons, charged particles like carbon ions or protons show an inverted depth-dose deposition (cf. Figure 1.3). The dose deposition of charged particles increases with penetration depth and most of the energy is deposited at the end of their range, whereas the initial energy of the particle determines their depth-dose profile. The observed peak which occurs shortly before the particle stops is the so-called Bragg peak, named after William Henry Bragg, who first described the inverse depth-dose profile of high LET alpha particles in 1904 (Brown, 2004; Kraft, 2000).

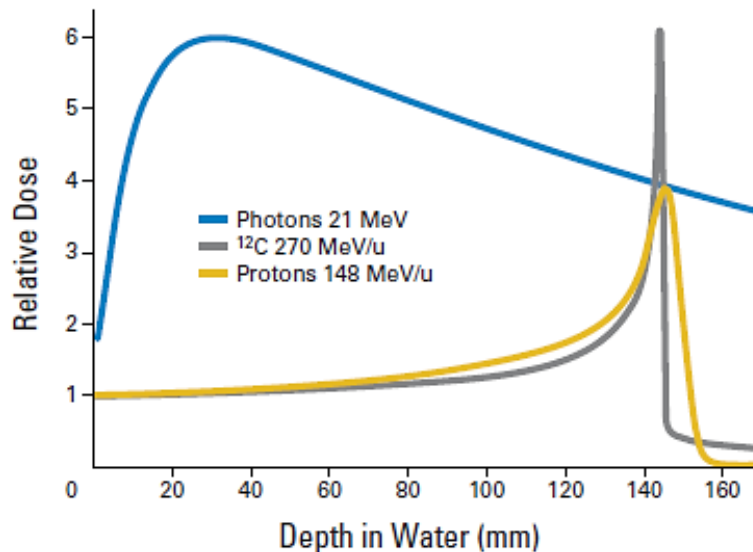


**Figure 1.3:** Depth-dose profiles of 21 MeV photons, 148 MeV/u protons and 270 MeV/u carbon ions. This figure is taken from (Schulz-Ertner, 2007) with the kind permission of the publisher. Copyright 2007 by American Society of Clinical Oncology licensed under 4190071314538.

In fact, dose is a macroscopic quantity. To describe energy absorption on small spatial scales, dose is not defined anymore and microdosimetric quantities such as linear energy loss have to be used. For radiotherapy with particle beams, the dose in Gray in a small volume can be described as:

$$D[\text{Gy}] = 1.6 \times 10^{-9} \frac{dE}{dx} \left[ \frac{\text{keV}}{\mu\text{m}} \right] \times F[\text{cm}^{-2}] \times \frac{1}{\rho} \left[ \frac{\text{cm}^3}{\text{g}} \right] \quad \text{Eq. 1.1}$$

where  $\frac{dE}{dx}$  is energy loss,  $\rho$  the density of the target material and  $F$  the fluence of the particle (Kraft, 2000; Scholz, 1996).

### 1.2.2 Linear energy transfer (LET)

In the propagation direction of the particle track, the energy loss is characterized by the linear energy transfer (LET) for particle energies used in radiotherapy. LET of charged particles is defined as:

$$\text{LET} = \frac{\Delta E}{\Delta l} \quad \text{Eq. 1.2}$$

where  $\Delta l$  is the track length traversed by the particle and  $\Delta E$  is energy loss. LET depends on the particle type and its energy.

Heavy ions lose their kinetic energy through the interaction with the target nuclei and interactions with target electrons. For charged particles at the energies used in radiotherapy, the energy transfer by interactions with target electrons is the dominated process (Kraft, 1992). The change in LET of heavy ions and protons can be approximated by the Bethe formula (Bethe, 1930):

$$-\frac{dE}{dx} = \frac{4\pi e^4 (Z_{eff})^2 ZN}{m_e v^2} \cdot \left[ \ln \left( \frac{2m_e v^2}{I} \right) \right] + \text{relativistic terms} \quad \text{Eq. 1.3}$$

with the energy loss per length  $\frac{dE}{dx}$ , the electron charge  $e$  and mass  $m_e$ , the projectile velocity  $v$ , the target atomic number  $Z$ , the electron density of the target  $N$  and the average excitation energy  $I$  of the target.

Figure 1.4 shows the dependence of LET on particle energy for different ions. Here, for higher energies, the energy loss is low. With an increasing penetration depth in matter, the ion's velocity becomes reduced and energy loss is increased up to a maximum at the end of the ion range forming the Bragg peak.

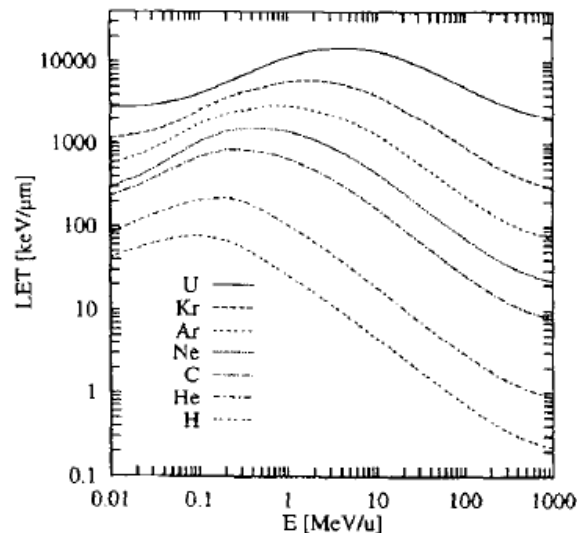


**Figure 1.4:** Linear energy transfer (LET) as a function of particle energy for different ions. The energy loss is higher at lower energies. This image is taken from (Kraft, 2000) with the kind permission of the publisher. Copyright 2000 by Elsevier licensed under 4190080021425.

The Bragg peak position depends on the initial particle energy. In general, the specific depth-dose profile makes charged particles more suitable for the radio therapeutic treatment of deep seated tumors than photon irradiation, because less energy is deposited at the entrance and in the surrounding normal tissue and the maximum of energy is deposited in the Bragg peak, whose position can be adjusted by choosing the specific ion energy.

### 1.2.3 Radial dose distribution and track structure

The internal structure of charged particles also plays an important role in the biological response. The structure of the ion track originates from electrons which are created by ionization of the target atoms by the primary ion. The traversal of these electrons through matter around ion trajectories causes secondary ionization (Kraft, 2000). The main reason for the extremely localized energy deposition along the ion trajectory is the emission of electrons which carry the

energy forwards. A predominant fraction of electrons is emitted at large angles resulting in electrons with low energies and short range (Scholz, 2003). Accordingly, only a small fraction of the emitted electrons are generated as electrons with high energies, which are capable to transport energy to places far away from the ion trajectory (Scholz, 2003).

In general, the dose distribution of emitted secondary electrons depends on the energy of the primary particle. Therefore, charged particles with low energy and high LET are densely ionizing showing a narrow track structure and very high local doses in the center of the particle track, as can be seen in Figure 1.5 in the case of carbon ion. On the contrary, particles with high energy and low LET are sparsely ionizing radiation with a wider track structure (cf. Figure 1.5).

The radial dose distribution within a particle track  $D(r)$  can be described as a function of the distance  $r$  from the center of the ion track (Scholz, 2003). Accordingly,  $D(r)$  is inversely proportional to the squared radial distance from the center of the particle track, i.e.  $D(r) \propto \frac{1}{r^2}$ .

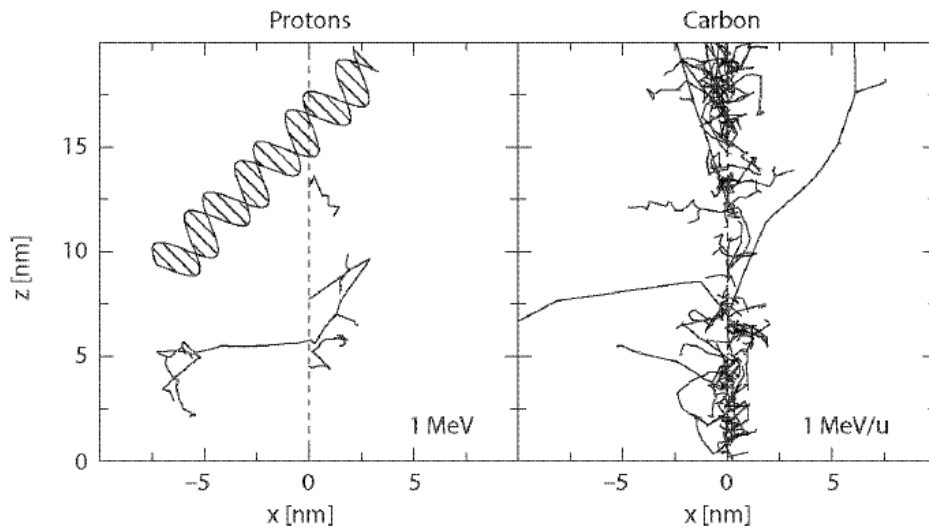


**Figure 1.5:** Simulation of secondary electron emission by 1 MeV protons (left) and 1 MeV/u carbon ions (right) when penetrating matter. This figure is taken from (Scholz, 2003) with the kind permission of the publisher. Copyright 2003 by Springer licensed under 4190080848188.

### **1.3 Biological effects of ionizing radiation**

Charged particles and photons show different biological effects as a consequence of their different physical properties. The understanding of the biological effects is of special importance since humans are exposed to different types of ionizing radiation, used for diagnostic and therapeutic purposes but also due to exposure to natural background radiation. In the following sections, the biological effects of the ionizing radiation are described with special emphasis on the biological endpoints of DNA damage repair, cell death induction and cell survival.

#### **1.3.1 Ionizing radiation induced DNA damage**

The biological effects originate mostly from damage to the deoxyribonucleic acid (DNA) which represents the most critical cellular molecule that can be affected by ionizing radiation (Hall, 2006). DNA is contained in the cell nucleus and encodes the cell's genetic information. DNA consists of two strands, which are held together by hydrogen bonds between complementary base pairs forming the well-known double helical DNA structure, which was described for the first time by Francis Crick and James Watson in 1953 (Watson, 1953). Each DNA strand consists of nucleotides made of sugar deoxyribose and phosphate group, representing the backbone of the structure and four different bases, which are attached to the DNA backbone: adenine (A), thymine (T), cytosine (C) and guanine (G). The complementary base pairs can be formed by these four bases: A is complementary to T, and G is complementary to C. This is represented in the schematic figure in Figure 1.6. The sequence of about  $3 \cdot 10^9$  base pairs specifies the genetic code of a human cell (Alberts, 2002).

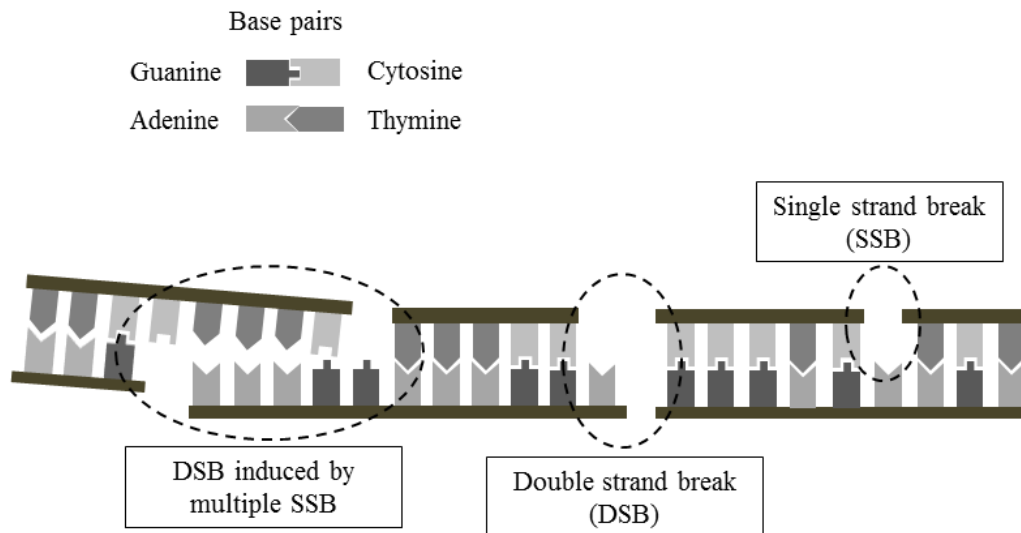


**Figure 1.6:** Schematic figure of two DNA strands, consisting of four nucleobases, which are bound together, according to the base pairing rules (A with T, C with G) in order to form double stranded DNA. The radiation induced DNA damage resulting either from the break from one DNA strand, also known as a single strand break (SSB) or from the break from both DNA strands, also called as a double strand break (DSB). A DSB can also be formed by two SSB, which lie on opposite strands and are separated by only a few base pairs.

Energy deposition by ionizing radiation can occur either directly by ionizing the DNA or indirectly by ionizing other molecules, particularly water, because approximately 80 % of a cell is composed of water. By indirect action of radiation, ionization of water molecules leads to the formation of many radicals, where production of a hydroxyl radical (OH) is most important as it damages the DNA. The direct radiation action dominates for densely ionizing radiation with high LET, whereas for sparsely ionizing radiation (e.g X-rays) about two thirds of the DNA damage is caused by the indirect radiation action (Hall, 2006).

Different types of DNA damage may be induced by ionizing radiation: single- and double strand breaks and base damages. All these DNA lesions have different severity concerning their possible repair and consequently the fate of the afflicted cell. Induction of a break in one DNA strand, also known as single strand breaks (SSB), is of little biological significance and can be easily repaired using a second DNA strand as a template. The induction of SSBs can be observed as a function of



the radiation dose. For instance, after exposure of a mammalian cell to 1 Gy of  $\gamma$ - radiation up to 1000 SSBs can be observed (Lomax, 2013).

If two or more breaks are induced in both opposite DNA strands and these breaks are separated by only a few base pairs, this may lead to the formation of a double strand break (DSB) (cf. Figure 1.6). DSBs are regarded as the most relevant lesions leading to most biological insults from radiation, since non-repaired or misrepaired DSBs can lead to the formation of unstable or stable chromosome aberrations, mutations or cell transformation. The yield of DSBs increases linearly with radiation dose, starting from a dose of a few mGy. After irradiation with 1 Gy of  $\gamma$ -rays formation of about 20-40 DSBs could be observed (Lomax, 2013). Forms of DNA damage consisting of two or more lesions on both DNA strands induced within a few base pairs, are so-called clustered damage sites or locally multiply damaged sites (Hada, 2008; Iliakis, 2015; Schipler, 2013; Ward, 1985).

Clustered DNA lesions can comprise a DSB, SSBs of varying complexity, oxidized base lesions or regular as well as oxidized abasic sites (Hada, 2008). Generally, two major groups of clustered DNA damage can be distinguished: DSBs and non-DSB oxidative clustered DNA lesions (OCDL) (Hada, 2008). If multiple DSBs are induced in close proximity these DSBs are considered to be complex DSBs (Hada, 2008; Mavragani, 2017).

Sparsely ionizing (low LET) radiation, such as X-rays, induces isolated DSBs, whereas the generation of clustered DNA damage occurs more frequently after densely ionizing (high LET) radiation particularly due to the high local energy deposition from the ion trajectory. This higher frequency of clustered DNA lesions is considered to be the main reason for the enhanced biological effects of high-LET radiation (Schipler, 2013). The formation of multiple DSBs in close proximity allows for the interaction of these DSBs to cause chromosomal aberrations more probably. In general, this would mean if two elementary lesions are formed in sufficient spatial vicinity they may result in a more complex lesion which has a larger effect than the sum of the effects of both isolated lesions, i.e. they act synergistically (Friedrich *et al.*, Submitted).

Different hypotheses exist relating to radiation induced DNA damage and the role of complexity in its repair. To date, several authors assumed that clustered or complex DNA damage is caused due to the proximity of two lesions on the level of a micrometer (Lea, 1942; Neary, 1965) or on the level of several base pairs on the nanometer scale of the DNA (Goodhead, 1989; Goodhead, 1994). Goodhead opened up the question of the association of spatial scales and their

corresponding targets. He suggested a coexistence of different scales, which seem to be relevant for radiation damaging (Goodhead, 2006). However, up to now the biological implication of DNA damage complexity is still not well understood and there are also some uncertainties in the definition of complex damage and different types of DNA damage which are responsible for the enhanced biological effectiveness of high LET radiation. Thus, the effects of different spatial dose and DSB distribution within a cell nucleus and the corresponding biological relevance were investigated in this study.

### **1.3.2 DNA damage repair**

Radiation induced DNA damage can arrest the normal progression of the cell cycle by activating several DNA damage checkpoints. This allows for the DNA damage repair, and furthermore it prevents passing of damaged DNA on the progeny (Sancar *et al.*, 2004). For the repair of the most harmful radiation induced DNA damages such as DSBs and complex DSBs, different repair mechanisms can be used by the cell. Two most important DNA repair pathways are the non-homologous end-joining (NHEJ) and the homologous recombination (HR). The choice between the two repair mechanisms depends strongly on the type of DNA damage and on the actual cell cycle position during cell irradiation (Branzei, 2008; Mladenov, 2011; Shrivastav, 2008).

DSBs induced during the G1 cell cycle phase are mainly repaired by NHEJ, a fast and an error-prone repair pathway. HR is a slower but an error-free repair process, which takes place predominantly in the late S- and G2 phase using the intact sister chromatid as a homologous template in order to restore the DNA sequence. In contrast, the NHEJ brings two ends of a DSB together by ligation regardless of whether these ends arrive from the same chromosomes, and so chromosome aberrations can occur. Recent studies indicate the presence of a third repair mechanism, used by the cell as an alternative DSB repair process, termed as the alternative end joining (alt-EJ) (Chang *et al.*, 2017; Frit *et al.*, 2014; Iliakis, 2015) in order to backup efficiently failed NHEJ but also HR, suggesting that in G1-phase, NHEJ will be chosen by cells to repair DSB and alt-EJ next, when NHEJ fails. Similarly, G2 and S- phase cells will choose HR first the repair of DSBs, followed by NHEJ and alt-EJ only as a last resort (Iliakis, 2015).

Complex DSBs are less readily corrected by cellular repair pathways due to their complexity, than the singular, well separated DSBs (Goodhead, 1994; Ward, 1994). Several studies reported that high LET particle irradiation induces more complex DNA lesions, and a greater involvement

of HR in the repair of those lesions was observed. For instance, HR is supposed to be more involved in the repair of DSBs induced by carbon ions than in the repair of those induced by photon or proton irradiation (Gerelchuluun *et al.*, 2015).

DNA DSB repair in irradiated cells can be investigated by fixation of the DNA damage at different time points after irradiation and by analyzing appearance and removal of  $\gamma$ -H2AX, a phosphorylated form of the histone H2AX which is involved in the repair of DNA DSBs after irradiation (Rogakou *et al.*, 1998). H2AX acts as DNA damage sensor protein that gets phosphorylated upon induction of DSBs in the DNA in order to signalize to other repair proteins to come to the damage site and repair the damage. The dephosphorylation of  $\gamma$ -H2AX occurs after DNA DSBs are repaired. Besides H2AX, there are several other proteins which are involved in the DNA DSB repair and their recruitment and processing of the DSBs follow biphasic repair kinetics, characterized by fast repair rates at early times and subsequent slower repair rates at later times after radiation. Correspondingly, the proportion of fast and slow repair depends on the choice of the repair pathway, on the damage complexity and chromatin density. The residual amount of  $\gamma$ -H2AX represents the unrejoined DSB or persistent DNA damage. According to DNA rejoining studies exposure to high LET radiation resulted in a significant fraction of unrejoined DSBs, indicating that DSBs generated by high LET radiation are more severe and complex than the DSBs produced by low LET radiation (Heilmann, 1996).

The main question to be solved is whether the non-homogeneous distribution of DSBs produced by focused low LET proton irradiation has any consequences for their repair and consequently the biological effectiveness.

### **1.3.3 DNA damage induced apoptosis**

Depending on the phase of the cell cycle, cell type and the DNA damage extent, p53 modulates DNA damage repair processing, or it acts as a transcription factor by activating transcription of genes which are important for the regulation of the cell cycle arrest (transient or permanent) or for the cell death. If radiation induced DNA damage cannot be properly repaired, cell death response can be triggered in order to eliminate damaged cells. Apoptosis is one of the cell death pathways which can be observed after cell exposure to ionizing radiation. In particular, the cells from lymphoid and myeloid lineages are prone to apoptosis (Eriksson, 2010). Apoptotic cells show morphological characteristics such as shrinkage of the cell, blebbing of the cell membrane

and fragmentation of the cell nucleus (Lauber *et al.*, 2012). Radiation-induced apoptosis is regulated mostly by the mitochondrial or intrinsic death pathway, which is characterized by different biochemical stages following a p53-dependent expression of pro-apoptotic proteins. The expression of pro-apoptotic proteins causes permeabilization of the mitochondrial outer membrane, which in turn induces release of cytochrome c into the cytosol. As a consequence, the apoptosome is formed and procaspase-9 is activated. The activation of caspase-9 in turn triggers the activation of the effector caspases-3 and -7, which are responsible for the execution of the apoptotic final stage and the cellular breakdown (Lauber *et al.*, 2012). Activated caspases are a hallmark of apoptosis.

As is generally known, the *p53* has an important role in the radiation-induced apoptosis (Gudkov, 2003; Polyak *et al.*, 1997). Mutated *p53* gene may contribute to radio- and chemoresistance of cancer, since the DNA damage caused by either ionizing radiation during conventional radiotherapy with X-rays or by cytotoxic drugs during chemotherapy cannot induce apoptosis without functional p53 protein (Martinez, 2010). Although it is already known that high LET radiation can more efficiently induce apoptosis than low LET radiation, little is known about the underlying mechanisms. Several studies reported that apoptosis can be induced independently of *p53* gene status in cancer cells following high LET radiation (Iwadate *et al.*, 2001; Mori *et al.*, 2009; Nakagawa *et al.*, 2012; Takahashi *et al.*, 2004). Thus, high LET radiation is expected to be an efficient alternative radiotherapy particularly for the treatment of tumor patients with the mutated *p53* gene (Iwadate *et al.*, 2001; Takahashi *et al.*, 2004). Further characterization of the molecular pathways obtained from experiments with *p53* mutated cell lines after high LET radiation revealed that high LET radiation induces higher apoptotic rates through the activation of Caspase-3 and Caspase-9 and by simultaneous suppression of the Akt-related signaling pathways (Nakagawa *et al.*, 2012).

In the present study apoptosis induction was analyzed by measuring caspase 3/7 activation in cells following focused proton irradiation in comparison to a homogeneous proton irradiation.

#### **1.3.4 Cell survival**

As described in the previous section, misrepaired or unrepaired DSBs leftover after exposure to ionizing radiation may trigger the formation of unstable or lethal chromosome aberrations, such as dicentric chromosomes, acentric chromosomes or centric rings. Such lethal chromosome

aberrations will be lost during subsequent cell divisions due to mechanical problems, thus preventing the cell from dividing into two daughter cells. Cells carrying such lethal chromosome aberrations will certainly be eliminated from the cell population, by activating different cell death pathways, such as mitotic catastrophe, apoptosis, permanent cell cycle arrest (senescence) or by necrotic cell death. In all these cases the cells will lose their reproductive integrity resulting in cell death. A surviving cell that has retained its reproductive integrity and is able to proliferate and to produce a large colony is said to be clonogenic (Hall, 2006). This biological end point of clonogenic cell survival can be measured with cells cultured *in vitro* by the colony forming assay. This assay represents a gold standard method, used to analyze the ability of single cells to grow into colonies (Franken *et al.*, 2006). Furthermore, it describes the full extent of radiation effects to the cells, because effects are observed after failing of cell repair processes, resulting in cell killing.

This technique was described first by Puck and Marcus in 1956, as a cell culture technique, which can be used to assess the ability of single cells to form colonies (Puck, 1956). Here, authors irradiated HeLa cells with X-rays and for the first time a dose-response curve was yielded. They observed that an accurate count of colony-forming survivors can be obtained after 11 days of incubation of irradiated HeLa cells if the criterion employed for cell survival is that at least 50 cells are present in the colony at the end of this period (Puck, 1956). Since then this cell number is used as a definition for a colony (Franken *et al.*, 2006).

Clonogenic cell survival can be described by a dose-response curve, representing the relationship between the fraction of cells that retained their reproductive integrity and the absorbed radiation dose. The mathematical model used in order to fit the experimental cell survival data is the linear quadratic model, which describes cell survival by a second order curve:

$$S = e^{-(\alpha D + \beta D^2)} \quad \text{Eq. 1.4}$$

where  $S$  represents the cell surviving probability,  $D$  the radiation dose,  $\alpha$  and  $\beta$  are two components that contribute to cell killing and describe the initial slope and bending of the cell survival curve. The first component  $\alpha$  is proportional to the dose, whereas  $\beta$  component is proportional to the square of the dose.

Many factors influence the shape of the cell survival curve and thus cell survival. For instance, the cells from different tumor entities show a broad range of radiosensitivities. Furthermore, radiosensitivity of cells depends strongly on the radiation quality, especially on the particle type, its energy, LET and spatial dose distribution. Increasing LET of radiation, the cell survival curve becomes steeper and the shoulder of the curve gets smaller, resulting in more cell killing. Despite radiation quality, cells in different cell cycle phases show differing radiosensitivity. In general, cells in G2 and M phase of the cell cycle are most sensitive to radiation, whereas cells from the late S phase are considered to be most resistant to radiation. This cell cycle dependency can be observed after low LET radiation, but this is not the case when high LET radiation is used. Thus, the variation in radiosensitivity through the cell cycle decreases with increasing LET (Hall, 2006). Furthermore, the presence of oxygen in cells during radiation can also influence cell survival. Higher radiosensitivity was observed in cells that were irradiated with low LET radiation in the presence of oxygen (under aerated conditions) than in its absence (hypoxic conditions). This radiosensitizing effect of oxygen is much lower after high LET radiation, because the biological damage produced by high LET radiation is mainly through direct action to the DNA and only little by the indirect action mediated by free radicals.

Cell survival is mainly used to assess the biological effectiveness of radiation and it has been used in many modelling studies, e.g. Local Effect Model (LEM) in order to give an accurate prediction of the biological effectiveness prior to radiation therapy of cancer with heavy ions.

The main question to be investigated in this work is how the cell survival is affected by spatial dose distribution and whether an increased biological effectiveness can be achieved by focusing low LET radiation using protons, in such a way that high-LET radiation effects can be mimicked.

#### **1.4 Relative biological effectiveness (RBE) and its characteristics**

When biological end points are investigated after exposing cells to low and high LET radiation, the final experimental outcome may differ between different radiation qualities due to physical doses needed to induce the same biological effect. These differences in effectiveness might be due to differences in the physical properties of the radiation qualities used, resulting in different energy depositions. In order to compare the effectiveness of different radiation qualities, e.g. particles with varying LET, the relative biological effectiveness (RBE) has been introduced. The

definition of RBE is the ratio between radiation doses applied using a reference radiation and a test radiation, resulting in the same effect, under identical conditions (Iaea, 2008):

$$RBE = \frac{D_{reference}}{D_{test}} \quad \text{Eq. 1.5}$$

As reference radiation in this work 200 kV X-ray radiation was used.

The dependency of RBE on LET is a very important aspect of this work. In general, the RBE increases with LET up to a maximum of 100 keV/μm and it decreases subsequently for higher LET values (Hall, 2006). LET at which RBE reaches the maximum is the same for a broad range of mammalian cells and for the end point of cell killing and induction of chromosome aberrations. However, the RBE value depends on the particle type used for irradiation. For instance, Figure 1.7 represents the dose response curves for the cell survival in hepatocellular carcinoma cells Hep3B cells after exposure to 200 kV X-rays and 130 MeV/u carbon ions, and it shows how the RBE can be evaluated from cell survival curves obtained after radiation with differing LET values. Unlike X-rays, carbon ions are high LET radiation. With increasing LET, the initial slope of the cell survival curve gets steeper and the shoulder gets smaller. Correspondingly, the absorbed dose of X-ray irradiation which is needed to induce 10% cell survival is 4.19 Gy, whereas the dose from carbon ion irradiation to induce the same cell survival level is 1.44 Gy. The RBE value for carbon ion irradiation needed to induce 10% cell survival can be calculated using the Eq. 1.5. The resulting RBE for carbon ion irradiation for 10% cell survival is 2.9.

Furthermore, the RBE depends on several other physical factors, e.g. particles energy or absorbed dose, and on biological factors, such as the biological end point under consideration and the cell or tissue type.

The concept of the RBE is of special importance with regard to tumor therapy with heavy ions and the use of a correct RBE represents a crucial factor. Thus, RBE values have to be used that are as realistic as possible. The RBE used for proton radiotherapy is assumed to be constantly close to one, whereas for heavy ion radiotherapy using carbon ions the dose has to be weighted by the RBE. Due to the complex RBE dependency, biophysical models are essential for the estimation of clinically relevant RBE values in treatment planning. A theoretical simulation

model which is implemented in treatment planning is the Local Effect Model (LEM). LEM has been developed at the Gesellschaft für Schwerionenforschung (GSI) as the first model for treatment planning taking into account the complex RBE dependency (Elsässer, 2008). This biophysical model is based on the notion of the distribution of DNA lesions on different spatial scales. As LEM is used in this study, it will be presented in more detail in the following section.

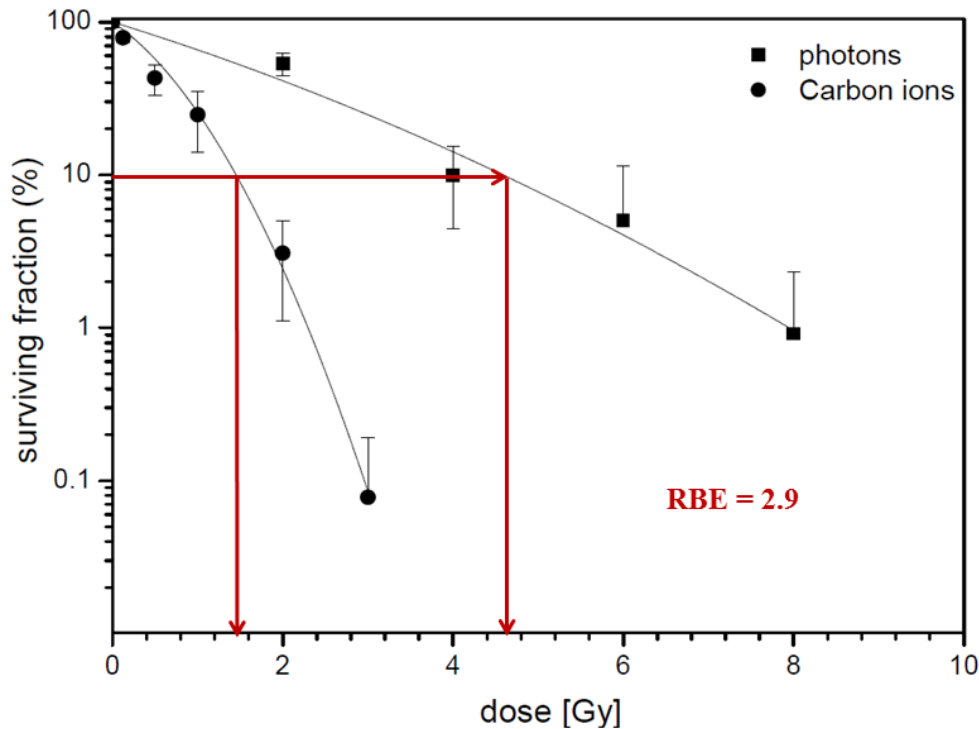


**Figure 1.7:** RBE dependency with differing LETs. Carbon ion irradiation shows higher RBE values for cell killing than X-rays (reference radiation). RBE of carbon ions in Hep3B cells is 2.9 times higher for 10% cell survival as compared to X-ray irradiation. This figure is adapted from (Habermehl *et al.*, 2014).

## 1.5 Local Effect Model (LEM)

LEM is a predicting model currently implemented in the treatment plan systems for radiotherapy with heavy ions in Europe. The model corrects for the physical dose required for the tumor by predicting the RBE for cell killing. According to LEM, the biological effects of radiation with heavy ions are derived directly from the cellular or tissue response to photon radiation and thus



the effectiveness of heavy ions can be determined by extrapolation from the dose response curve using photons, e.g. X-rays as reference radiation.

The distribution of the local dose within a particle track can be described as a function of the radial distance from the center of the ion track (Elsässer, 2008).

Accordingly, the calculation of the effectiveness of charged particles relies on the microscopic local dose distribution pattern of ion traversals within the cell nucleus (Friedrich *et al.*, 2012).

In a recent version of LEM (LEM IV), some substantial additions were introduced as compared to the prior LEM versions (LEM I-III (Elsässer, 2008; Scholz, 1996; Scholz, 1997)). Here, an intermediate step was introduced, based on the assumption that the final cellular response to radiation can be related to the distribution of the initial DNA damage (Elsässer, 2010). In accordance with this latest version of LEM, the microscopic spatial DNA DSB distribution and thus their local density within a nucleus is assumed to be the most relevant measure that determines the cell fate following radiation.

Here, the SSBs and DSBs are considered as elementary lesions that interact on different scales to form complex DNA damage. For the calculation of DSB yields based on LET, LEM assumes that if two SSBs are induced within 25 bp on opposite DNA strands that corresponds to a distance of a few nm on the DNA, these two SSBs may interact and form a DSB. This interaction of SSBs is responsible for the enhanced DSB yield in the case of high local doses in the core of ion tracks (Friedrich, 2015). Another assumption of LEM is that DSBs interact or cluster on the micrometer scale within DNA sub-compartments. Here, the cell nucleus is assumed to be compartmentalized into cubic-shaped sub-volumes of 510 nm side length, which are related to 2 Mbp DNA content. The number of DSBs in each sub-volume can be determined in order to assess the proximity of DSBs and thus the clustering of DSBs. Isolated DSBs exist if only one DSB is found in such a sub-volume, whereas in the case of two or more DSBs in a sub-volume clustered DSBs are formed (Elsässer, 2010). The mean number of DSBs in small sub-volumes stem from the cellular response to photon radiation, indicating a DSB yield of about 30 DSBs/Gy in a cell.

The LEM has been supported by various experimental findings, and it allows for RBE predictions for all clinically relevant ion types and ion energies. However, the essential question, would be, how accurate LEM can predict the biological response necessary for treatment planning. Therefore, a permanent improvement of LEM is required. In the framework of the LET project, LEM predictions on cell survival for low LET focused and random proton irradiation and high

LET lithium and carbon ion irradiation were made and compared with the experimental data in order to test the accuracy of the LEM and their assumptions regarding DNA damage complexity and its biological relevance.

## 2. Materials and Methods

### 2.1. Cell culture: Chinese Hamster Ovary cells CHO-K1

Experiments in this work were performed using the Chinese Hamster Ovary cells, CHO-K1, purchased from Deutsche Sammlung von Mikroorganismen und Zellkulturen GmbH (DSMZ) (Code ACC 110, Lot 15) (Figure 2.1). At this point, it is important to emphasize the reason for choosing CHO-K1 cell line for the experiments of this work. Firstly, the CHO-K1 cells are used in order to ensure the best possible correlation with the LEM model used here in the study. The LEM model has been validated by experimental in-vitro cell survival data obtained from CHO cells. Secondly, this cell line is a well-established cell line in the field of radiobiology and it is very suitable for cell survival experiments because of the fast proliferation and uniform colony formation.

The cells were cultivated in RPMI-1640 medium (R8758, Sigma-Aldrich) supplemented with 10% fetal calf serum (F7524, Sigma-Aldrich), 100 units of Penicillin and 100 $\mu$ g of Streptomycin (P0781, Sigma-Aldrich) per ml culture medium, 2 mM L-Glutamine (G7513, Sigma-Aldrich) and 1 mM Sodium pyruvate (S8636, Sigma-Aldrich). The cells were grown as monolayer culture and were cultivated in an incubator at 37°C, 5 % CO<sub>2</sub> and 95% humidity. Under these culture conditions the CHO-K1 cells had doubling time of 12.2 $\pm$ 0.28 hours.

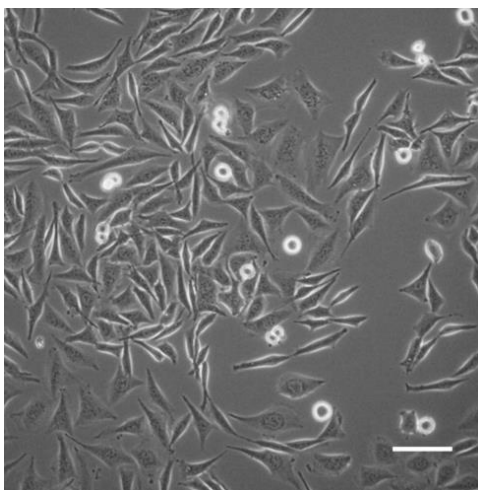


**Figure 2.1:** Adherent CHO-K1 cells in culture flask. Scale bar 50  $\mu$ m.

## 2.2. Cell cultivation on a well-defined restricted area

Several developments concerning the cell cultivation have been made in this work to allow for the investigation of the biological response to microbeam irradiation. These developmental steps are described in the following section.

Special irradiation containers were used for the particle irradiation of cells at SNAKE. These cell containers were constructed in such a way that a Mylar foil (of 6  $\mu\text{m}$  thickness) was stretched and clamped between two steel plates. The design of the irradiation containers has been described previously (Schmid *et al.*, 2012a). For the focused particle microbeam irradiation, it is of great importance that all seeded cells are irradiated, otherwise the unirradiated cells would distort the experimental outcome. To avoid this problem the established cultivation setup was modified and improved for the application in experiments with microbeam irradiation as described in detail by Greubel *et al.* (Greubel *et al.*, 2017).

About 4 hours before irradiation, the cells were seeded on the Mylar foil, which was pre-coated with Cell-TAK (Cat. No. 354240, Corning). For the procedure of cell seeding the cell cultivation setup as shown in Figure 2.2 was used.

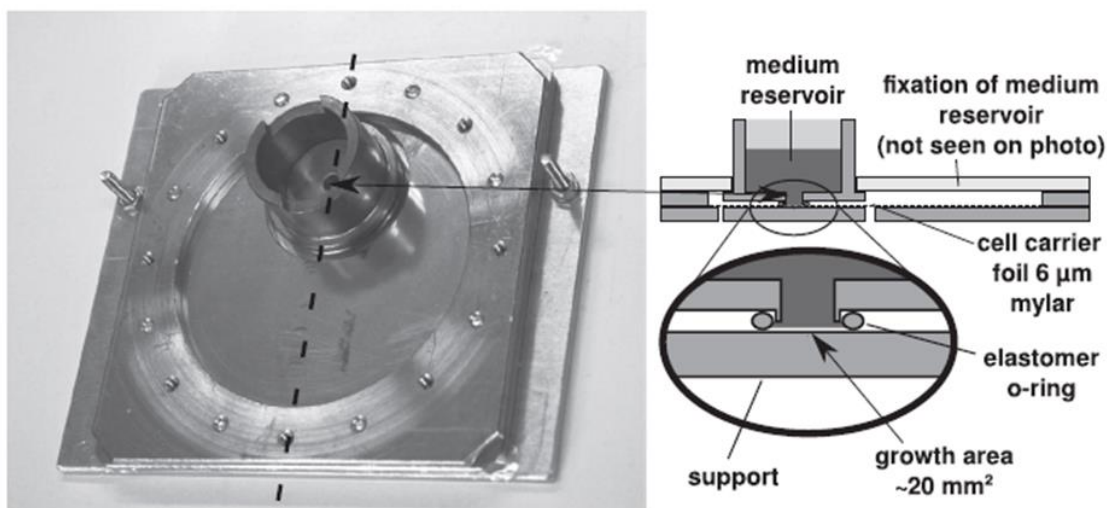


**Figure 2.2:** Cell cultivation setup used for irradiation experiments at SNAKE. This figure is taken from (Greubel *et al.*, 2017) with the kind permission of the publisher. Copyright 2016 by Elsevier licensed under 4190100051770.

For this purpose, an elastomeric O-ring was mounted at the bottom site of a medium reservoir, which was placed on the Mylar foil in order to prevent cell leakage during the incubation time of

4 hours. During this time the CHO-K1 cells were allowed to settle down and adhere to the Mylar foil. Using this cell cultivation setup cells were seeded in a well-defined area at the center, which is defined by an O-ring of 4 mm in diameter (outlined by a dashed circle in Figure 2.3) to achieve a limited cell growth area of approx. 15 mm<sup>2</sup>. This cell growth area was small enough to be irradiated as fast as possible, but it was still large enough to ensure a sufficient number of cells to perform the experiments.

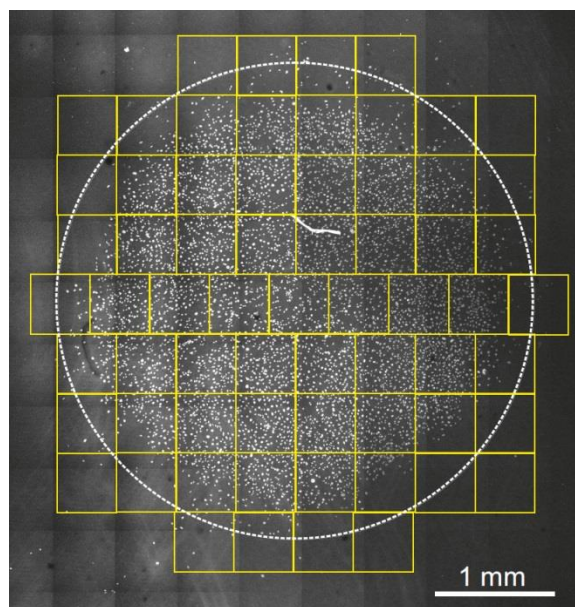


**Figure 2.3:** Stitched microscope image of CHO-K1 cells stained with DAPI after being cultivated using the described cell cultivation setup. The dashed white circle represents the cell growth area consisting of 65 square fields of (500 x 500) μm<sup>2</sup> which would be chosen for microbeam irradiation.

The cell growth area and the irradiation area comprised approximately 10.000-20.000 cells. Directly before irradiation, the cell cultivation setup consisting of medium reservoir with O-ring and it's support plates was removed and the cell sample was washed once with culture medium to remove all non-adherent cells. After this, the cell container was filled with 5 ml of culture medium, closed by another stainless steel plate, and was positioned vertically in front of the beam exit nozzle, with cells facing the microbeam. At this position, cells were not covered by culture medium, but the medium in the cell container prevented cells from drying out by ensuring a saturated atmosphere (Greubel *et al.*, 2008; Hauptner *et al.*, 2004).

## 2.3. Cell irradiation

### 2.3.1. Reference irradiation with X-rays

The irradiation of CHO-K1 cells was carried out at the X-ray irradiation facility (RS225, Gulmay Medical, UK) of the Department of Radiation Oncology, Technical University in Munich, in order to obtain a reference dose–response curve for cell survival. For irradiation experiments the same cell irradiation containers under identical cell culture conditions were used as for particle irradiation at SNAKE (as described in detail in section 2.2). For the irradiation, the cell monolayer was covered with 6 ml culture medium. To ensure that culture medium in the cell container will not be spilled during the transport to the irradiation facility, a cover was used screwed on the top of the cell container. A plexiglas disc was placed underneath the foil and cells were exposed to 200 kV X-rays at room temperature using a dose rate of  $1.21 \text{ Gy min}^{-1}$  (15 mA) and a source-cell distance of 42 cm in a field of  $20 \times 20 \text{ cm}^2$ . The experimental setup is shown in Figure 2.4.

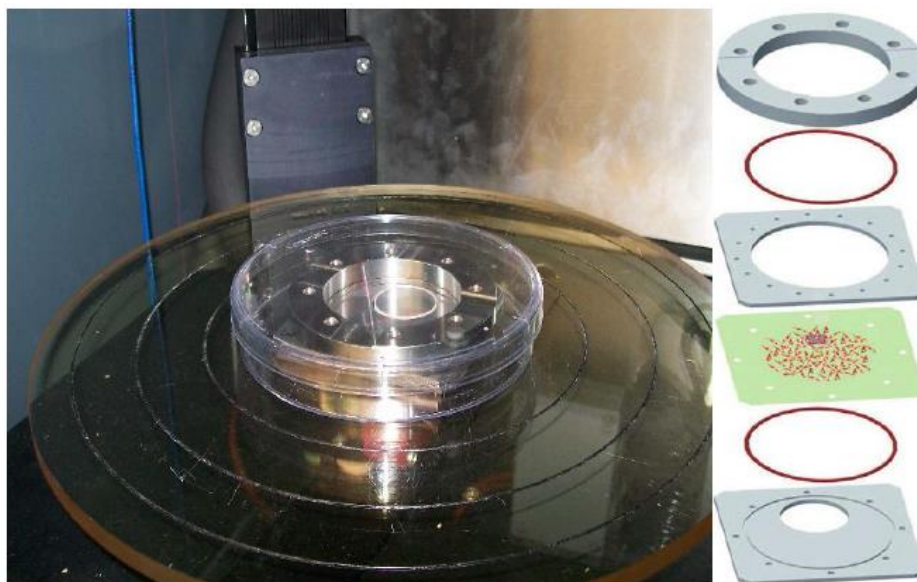


**Figure 2.4:** Experimental setup for X-ray irradiation of cells seeded on Mylar foil in cell containers used for SNAKE microbeam irradiation.

### 2.3.2. Particle irradiation at the ion microbeam SNAKE

Particle irradiation in this study was carried out at the ion microprobe SNAKE (Supraleitendes Nanoskop für angewandte kernphysikalische Experimente = superconducting nanoprobe for applied nuclear physics experiments) at the 14 MV tandem accelerator in Munich (Datzmann *et al.*, 2001) which has been adapted for application in biological studies (Hauptner *et al.*, 2004; Hauptner *et al.*, 2006; Schmid *et al.*, 2011a; Schmid *et al.*, 2012a). The well-established irradiation setup (Hable *et al.*, 2009; Hauptner *et al.*, 2004) as shown in Figure 2.5 has been recently adapted and upgraded to meet the highest requirements for the cell irradiation with ions using a scanned microbeam. The developments which have been made concerning the irradiation procedure at SNAKE are described in the following sections.

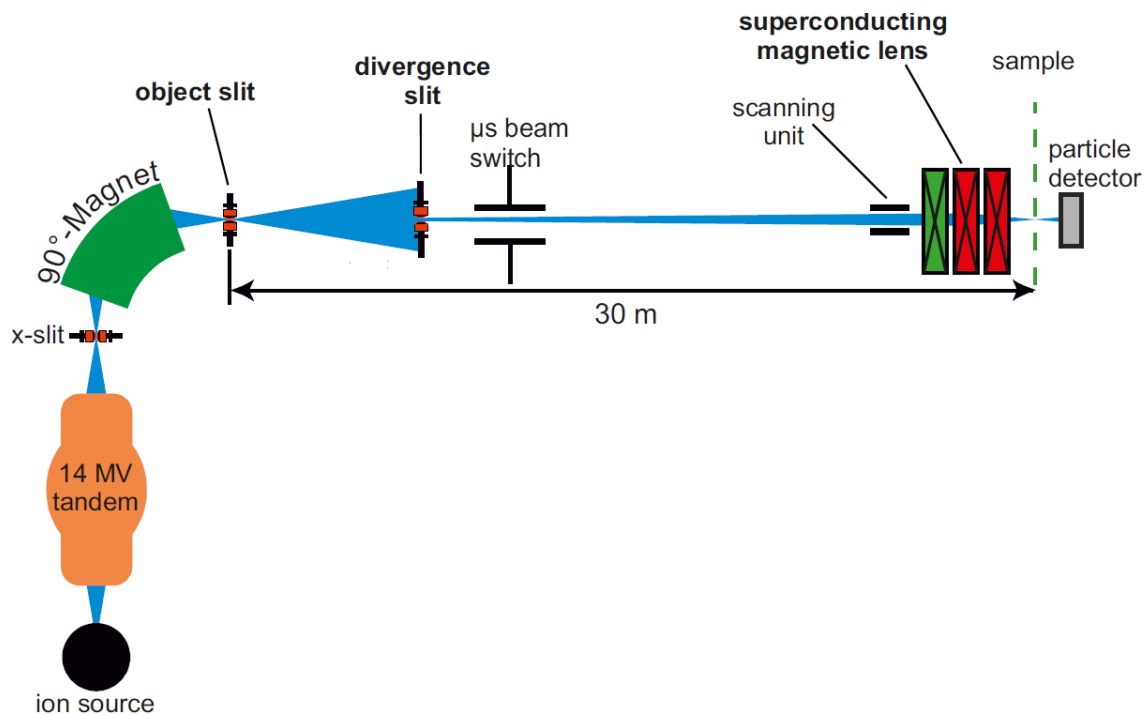


**Figure 2.5:** Set-up of the ion microprobe SNAKE at the Munich tandem accelerator (Courtesy of Judith Reindl).

Recent developments at SNAKE allow focusing of particles to a spot size of about  $0.5 \times 1.0 \mu\text{m}^2$  with a particle rate of 200-500 kHz for protons and 2-3 kHz for 55 MeV carbon ions (Greubel *et al.*, 2017). The ions were focused and transported in a vacuum to the beam exit nozzle, which

was covered with 7.5  $\mu\text{m}$  thick kapton foil. After passing the kapton foil, the ions traversed a 6  $\mu\text{m}$  thin Mylar foil before hitting the cells (Schmid *et al.*, 2012a). Behind the cell sample, a detector, as described in (Hauptner *et al.*, 2004) was placed to count the ions. A single ion preparation method was used to ensure the requested number of particles at each spot. Using electrostatic beam scanning, square fields of  $(500 \times 500) \mu\text{m}^2$  were irradiated with a certain number of ions. The cell container was mounted on the x-y- stage of an inverted optical microscope (Zeiss Axiovert 200 M) (Hable *et al.*, 2009) and by mechanically moving the cell sample, the quadratic fields were stitched together, and the whole cell growth area was covered. For random proton irradiation the microbeam was scanned over an area of  $(500 \times 500) \mu\text{m}^2$  field and protons were counted until a requested number of particles were reached.

Shortly before the cell irradiation, radiochromic films were irradiated to test if the field stitching shows gaps between the fields. The gaps between the fields would mean that cells in these fields would not be irradiated. To avoid the problem of unirradiated cells, a safety margin of 2% overlap between the fields was introduced (Greubel *et al.*, 2017). To irradiate the whole cell growth area of a cell sample about 80 fields of  $(500 \times 500) \mu\text{m}^2$  were stitched together and the irradiation took about 15 to 20 minutes. Prior to irradiation, the exact position of the irradiation field has to be determined. Using a phase contrast microscope, the coordinates of the center and radius of the irradiation field could be set (Greubel *et al.*, 2017).

In this work CHO-K1 cells were irradiated with 20 MeV ( $\text{LET} = 2.66 \text{ keV}/\mu\text{m}$ ) protons, 33 MeV lithium ions ( $\text{LET} = 81 \text{ keV}/\mu\text{m}$ ) and 55 MeV carbon ions ( $\text{LET} = 338 \text{ keV}/\mu\text{m}$ ). The size of the irradiated spots was analyzed and measured for each experiment as described in detail in (Greubel *et al.*, 2017). For cell survival experiments, cells were irradiated with a mean dose of 1.7 Gy either by focusing a defined number of particles to spots in a certain grid-like pattern or by homogeneously applied particles. All irradiation modalities deposited the same mean dose to the cells. An overview of all utilized irradiation modes used in cell survival experiments is given in Table 2.1. To investigate radiation induced apoptosis and DNA damage repair the cells were irradiated with a mean dose of 3.4 Gy.



**Table 2.1:** Overview of all applied particles used in SNAKE experiments and all irradiation modalities

Ion species	Grid pattern ( $\mu\text{m}^2$ )	Particles per point (ppp)
<b>20 MeV Protons</b> LET = (2.66 $\pm$ 0.13) keV/ $\mu\text{m}$	random	-
	5.4 x 5.4	117
	7.6 x 7.6	234
	10.8 x 10.8	468
<b>33 MeV Lithium ions</b> LET = (81 $\pm$ 8) keV/ $\mu\text{m}$	random	-
	3.82 x 3.82	2
	5.4 x 5.4	4
	7.6 x 7.6	8
	10.8 x 10.8	16
<b>55 MeV Carbon ions</b> LET = (338 $\pm$ 34) keV/ $\mu\text{m}$	5.4 x 5.4	1
	7.6 x 7.6	2
	10.7 x 10.7	4

### 2.3.3. Geometrical measurement of cell nucleus area for calculation of the hit statistics

The irradiation of cells using a microbeam in this work was carried out sequentially in a regular pattern. The probability for hitting a cell nucleus using different grid sizes was calculated, as the number of particles to hit a cell depends strongly on the current cell position relative to the utilized irradiation grid pattern. In a first step, the size of the cell nucleus was determined as described previously (Greubel *et al.*, 2017). For this purpose, CHO-K1 cells were seeded using the same cell cultivation setup (Figure 2.2) in parallel to irradiation experiments. 4 hours after seeding, cells were fixed with 2 % paraformaldehyde (PFA) (158127, Sigma- Aldrich) for 15 minutes at room temperature and subsequently washed once with phosphate-buffered saline (PBS) to get rid of the fixative. The cells were stained with DAPI by adding a drop of Vectashield (H-1200, Vector Laboratories), in order to make cell nuclei visible for detection. After DAPI-staining, z-stacks were acquired using confocal laser scanning microscopy. To obtain the largest shape of each cell nucleus, a projection along the z-axis was performed in all z-slices. The nuclei were outlined manually to determine the maximal area. For this approximation, the

cell nucleus is assumed to be a circle with the determined area that corresponds to a certain radius.

Monte Carlo simulation was performed in order to evaluate the hit statistics and determine the frequency of hits per cell nucleus. The individual nucleus shapes were placed randomly on each of the irradiation grid patterns used in our experiments and the number of hits inside the nuclei shape was evaluated (Greubel *et al.*, 2017).

## **2.4. DNA DSB repair**

### **2.4.1. Immunofluorescence staining of $\gamma$ -H2AX**

The  $\gamma$ -H2AX immunofluorescence assay was used in this work for the detection of radiation induced DNA DSBs in cells, since phosphorylated H2AX is a well-known marker of DNA DSBs. For this purpose, the cells were seeded on a large surface area of Mylar foil, labelled with coordinates. This allowed for the irradiation of just few cells from one cell sample using different irradiation modalities and performing immunofluorescence staining for all irradiation modalities at once under the same experimental conditions. After irradiation, the culture medium was replaced by fresh medium and the cell sample was brought back to the cell incubator where cells were incubated at 37°C for further 30 minutes. The culture medium was removed and cells were washed shortly once with PBS. In the following step, cells were fixed with 2% paraformaldehyde (PFA) for 15 minutes at room temperature and subsequently washed once with PBS to get rid of the fixative. The permeabilization step occurred by three washing steps in PBS + 0.15% Triton X-100 (X100, Sigma- Aldrich), each step for 5 minutes. Blocking of the unspecific epitopes was carried out by three washing steps in PBS<sup>+</sup> [0.15% glycine and 1% bovine albumin serum (BSA) (A7030, Sigma- Aldrich) in PBS], each for 10 minutes. After this blocking step, 75  $\mu$ l of the primary mouse anti-phospho-Histone H2A.X (Ser139) antibody (clone JBW301, Millipore), diluted 1:350 in PBS<sup>+</sup>, was pipetted on the cell irradiated area and cell samples were incubated overnight at 4°C. On the next day, antibody solution was removed and cells were washed once with PBS for 5 minutes. Subsequently, cell sample was permeabilized again with PBS + 0.15% Triton-X 100 for 10 minutes and blocked by washing in PBS<sup>+</sup> for 7 minutes. F(ab')<sub>2</sub>-Goat anti-Mouse IgG (H+L) Cross-Adsorbed conjugated with Alexa Fluor 488 (A-11017, Invitrogen) was diluted 1:500 in PBS<sup>+</sup> and the antibody was used as a secondary antibody. Finally, the nuclear

DNA was stained with DAPI and a cover slip was mounted with a drop of Vectashield (H-1200, Vector Laboratories). The microscopy images were acquired using a fluorescence microscope (AxioObserver Z1, Zeiss), with a 40x objective and an AxioCam (CCD MRm, Zeiss) for the multidimensional acquisition we used the Z-stack tool in order to process an extended depth focus.

#### **2.4.2. $\gamma$ -H2AX repair kinetics measured by flow cytometry**

For the experiment of  $\gamma$ -H2AX repair kinetics cells were seeded as previously described in Section 2.2. After irradiation, cells were detached from the Mylar foil by trypsinization and the cell suspension was transferred to a 15 ml falcon tube (9180323, Greiner Bio-One GmbH). After centrifugation at 300 g for 5 minutes the cell pellet was resuspended in 0.5 ml of PBS. Subsequently, 4.5 ml of ice-cold 70% ethanol was added and cell samples were stored at  $-20^{\circ}\text{C}$  overnight or for several days.

On the day of the  $\gamma$ -H2AX-staining, cell samples were centrifuged once again and the cell pellet was resuspended in 0.5 ml PBS in order to remove the fixative. In the following step, cells were permeabilized by washing in 1 ml of 0.15% Triton X-100 solution for 15 minutes. For flow cytometric evaluation, cells were resuspended in 0.1 ml of PBS + 10% FCS and 2  $\mu\text{l}$  of the gamma H2AX antibody (2F3) labeled with Alexa 488 fluorophore (NB100-78356AF488, Novus Biologicals) was added to the cells for 20 minutes on ice. This antibody reacts with Ser139-phosphorylated H2AX. After incubation with the antibody, cells were washed once with PBS + 10% FCS to get rid of the excess Alexa 488 conjugated antibody before the flow cytometric analysis. The flow cytometry data were acquired using a BD FACSCalibur flow cytometer equipped with the CellQuest software (Becton-Dickinson, USA) and the argon-ion laser, which produces 15 mW of 488 nm light. The cellular incorporation of Alexa Fluor 488 anti- $\gamma$ -H2AX was presented by use of fluorescence intensity histograms, as shown in Figure 2.6. For each irradiated cell sample, the  $\gamma$ -H2AX mean fluorescence intensity was determined and analyzed relative to the mean  $\gamma$ -H2AX fluorescence intensity of the corresponding unirradiated cell sample. The graphs represent mean values of technical replicates  $\pm$  standard error of the mean (SEM). The statistical analysis was performed using the GraphPad Prism7 software and statistical significance was evaluated using the two-tailed Student's t-test for unpaired samples ( $*p \leq 0.05$ ,  $**p \leq 0.01$ ,  $***p \leq 0.001$ ).

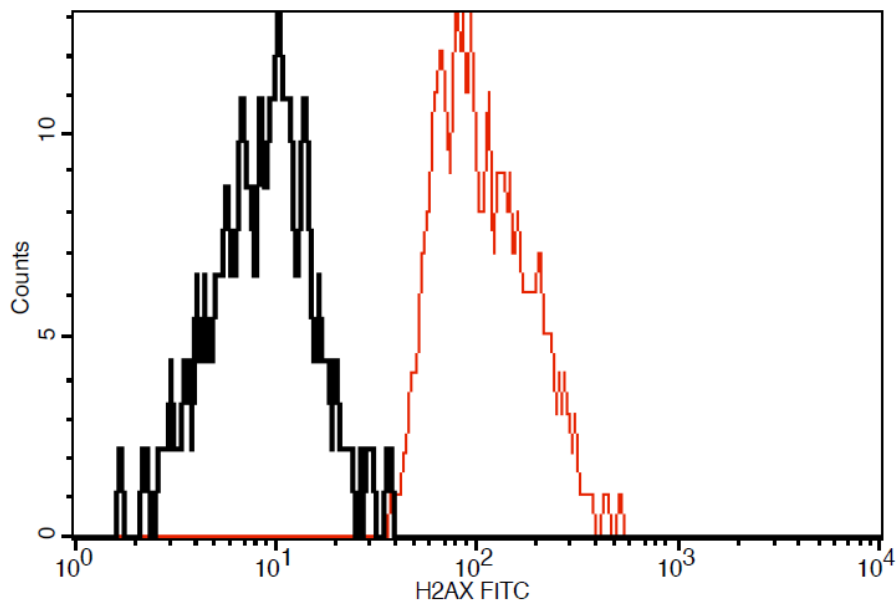


**Figure 2.6:** Representative flow cytometry histograms representing the  $\gamma$ -H2AX fluorescence intensity of unirradiated (black histogram) and proton irradiated cells (red histogram). After irradiation the  $\gamma$ -H2AX fluorescence intensity shifts to the right, showing increased  $\gamma$ -H2AX fluorescence intensity.

## 2.5. Analysis of caspase 3/7 activity using flow cytometry

Apoptotic cells were analyzed by evaluating the extent of activation of caspases 3 and 7 as response to ionizing radiation. After irradiation of cells, which were seeded on the Mylar foil as described previously in chapter 2.2, culture medium was replaced by fresh medium and cells were incubated for further 24 hours. After this incubation time, culture medium was collected out of the irradiation container and cells were washed once with PBS. PBS wash step was also retained, so that floating cells were pooled together with attached cells. 0.5 ml trypsin was pipetted directly on cells and cell samples were incubated for 4 minutes at 37°C. Subsequently, 4.5 ml medium was added to cells to neutralize the trypsin reaction and cell suspension was transferred into a 15 ml falcon tube. The remaining cells were washed out from the Mylar foil by adding 1 ml culture medium and cell suspension was transferred into the falcon tube, which already contained cells. In the next step, cells in falcon tubes were centrifuged at 500 g for 5 minutes at room temperature. The supernatant was removed and cell pellet was resuspended in 0.5 ml PBS. 0.5  $\mu$ l Caspase-3/7 Green Detection Reagent from the CellEvent<sup>®</sup> Caspase-3/7 Green Flow Cytometry Assay Kit (C10427, Invitrogen) was added to the cells and cell samples were incubated for 30 minutes at 37°C, protected from light. In addition to the detection of caspase

activation, the SYTOX<sup>®</sup> AADvanced dead cell dye was used as well in this assay in order to discriminate between live, apoptotic and necrotic cells. During the final 5 minutes of incubation with Caspase 3/7 Detection Reagent, 0.5  $\mu$ l of the 1 mM SYTOX<sup>®</sup> AADvanced dead cell stain solution in DMSO was added to the cells and cell samples were incubated for further 5 minutes at 37°C. Subsequently, stained cells were measured on the FACSCalibur flow cytometer. The fluorescence emission was collected using a 530/30 bandpass filter (FL1) for Caspase-3/7 Green Detection Reagent and a 670 longpass filter (FL3) for SYTOX<sup>®</sup> AADvanced dead cell stain.

The data analysis was performed using CellQuest software. The data are represented as dot plots as shown in Figure 2.7. Dot plots provide a two-parameter data display. With this kind of analysis, four different cell populations in each sample could be analyzed and classified as follows: caspase 3/7 and SYTOX negative (lower left panel), caspase 3/7 positive and SYTOX negative (lower right panel), caspase 3/7 and SYTOX positive or double positive (upper right panel) and caspase 3/7 negative and SYTOX positive (upper left panel) cells. From each quadrant the percentage of cells was evaluated.

The graphs represent mean values of biological or technical replicates  $\pm$  standard error of the mean (SEM). The statistical analysis was performed using GraphPad Prism7 software and statistical significance was evaluated using the two-tailed Student's t-test for unpaired samples ( $*p \leq 0.05$ ,  $**p \leq 0.01$ ,  $***p \leq 0.001$ ).

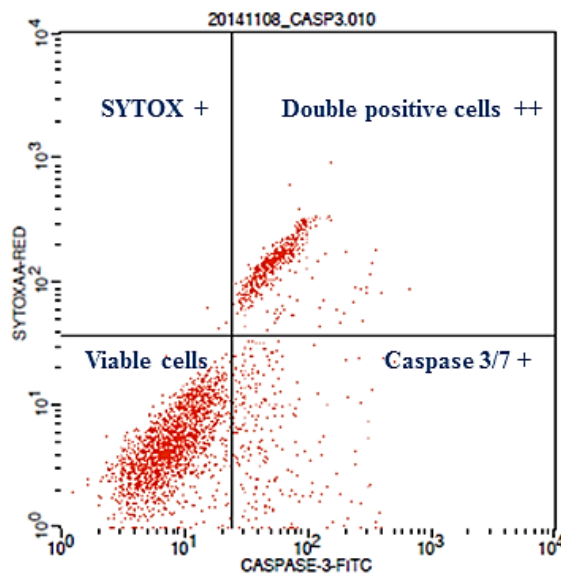


**Figure 2.7:** Flow cytometry analysis of data obtained for CHO-K1 cells 24 hours after irradiation using Caspase 3/7 and SYTOX staining in form of a dot plot.

## 2.6. Modified colony forming assay for cell irradiation at SNAKE

In order to determine the cell survival immediately after irradiation the clonogenic cell survival assay also called colony forming assay (CFA) was performed. Using cell cultivation setup which was designed for particle irradiation at SNAKE (cf. Figure 2.2) the cell growth area was limited to roughly 15 mm<sup>2</sup> and comprised about 10.000-20.000 cells to ensure cell irradiation in a reasonable time. Due to only small cell numbers that could be irradiated, the conventional CFA assay was modified in order to meet the requirements needed for microbeam particle irradiation of cells.

The cells were trypsinized from the Mylar foil using chambers, similar to those used for cell seeding. 0.3 ml of trypsin (T4299, Sigma-Aldrich) was added to the cells and cell samples were incubated for 4 minutes at 37°C. The trypsinization reaction was stopped by adding 0.6 ml culture medium. Mylar foil was washed out with additional 0.1 ml culture medium in order to collect the remaining cells from the foil. Subsequently, the cells from each sample were counted using the C-Chip, a disposable Fuchs-Rosenthal cell counting chamber (E63508-03, NanoEnTek), which is particularly well adapted for counting small cell numbers. The cell counting was performed four times for each cell sample and each time the whole hemocytometer area of 3.2 mm<sup>3</sup> was counted. After counting and determining the cell concentration per ml for each sample, the cell suspension was diluted in a dose-specific manner, and 1 ml of the diluted cell suspension was pipetted into the wells of 12 well plates (Costar # 3513, Corning). In case of unirradiated (sham) samples 100 cells were plated per well, while for the irradiated cell samples 200 cells were reseeded per well. For each sample, cells were re-seeded into wells of two to three 12 well plates, depending on the determined cell concentration.

12 well plates with seeded cells were incubated at 37°C until cells have formed sufficiently large colonies, which consist of at least 50 cells (Franken *et al.*, 2006). CHO-K1 cells formed colonies already after 5 days. On fifth day after irradiation medium was removed from the wells and cells were rinsed once with PBS (D8537, Sigma-Aldrich,). In the next step, cells were fixed with methanol (CP43.2, Carl Roth) for 5 minutes and stained with 0.1% crystal violet (from clinical pharmacy) for 2 minutes. Plates were washed with water and then left for drying at room temperature. The counting of stained colonies was performed by an automatic counting bioreader (BIO-SYS GmbH). Colonies consisting of 50 or more cells were counted. After this the plating efficiency (PE) and surviving fraction (S) were determined.

### 2.6.1. Statistical analysis of cell survival

The PE of a replicate ( $PE_i$ ) can be calculated as a ratio of the number of counted colonies and the number of cells seeded per well:

$$PE_i = N_{col} / N_{seed} \quad \text{Eq. 2.1}$$

where  $N_{seed}$  is the number of cells seeded per well ( $N_{seed/well} * N_{well}$ ) and  $N_{col}$  the total number of colonies in all seeded wells,  $N_{well}$ .

The plating efficiency of a data point ( $\overline{PE}$ ) can be calculated as:

$$\overline{PE} = \frac{1}{N_{rep}} \sum_i^{N_{rep}} PE_i \quad \text{Eq. 2.2}$$

$$\text{with } N_{rep} \text{ as the number of replicates and } \Delta PE = t(N_{rep}) \cdot \frac{SD(PE_i)}{\sqrt{N_{rep}}} \quad \text{Eq. 2.3}$$

as the standard error of the mean PE.

The cell survival,  $S$ , of irradiated cells was calculated as the relative  $\overline{PE}$  taking into account the PE of control cells,  $\overline{PE_0}$ :

$$S = \overline{PE} / \overline{PE_0} \quad \text{Eq. 2.4}$$

Performing the clonogenic cell survival assay, different errors due to cell handling can occur. Therefore, the cell survival is assumed to be normally distributed within a confidence interval of 68%. The uncertainty for the cell survival was calculated using the Gaussian error propagation:

$$\Delta S = S \sqrt{\left(\frac{\Delta PE}{PE}\right)^2 + \left(\frac{\Delta PE_0}{PE_0}\right)^2} \quad \text{Eq. 2.5}$$

If the errors from different experiments or beam times are similar the mean value for cell survival can be calculated:

$$S = \sum_{Exp=1}^{N_{Exp}} S_{Exp} \quad \text{Eq. 2.6}$$

whereas the error for the mean cell survival  $\Delta S$ , was calculated using the Gaussian error propagation:

$$\Delta S = \sqrt{\frac{1}{N_{Exp}} \sum_{Exp=1}^{N_{Exp}} (\Delta S_{Exp})^2} \quad \text{Eq. 2.7}$$

Averaged cell survival after X-ray irradiations and particle irradiations was calculated from two data sets from two different beam times. Graphs represent mean cell survival  $\pm$  SD (standard error). The statistical analysis was performed using GraphPad Prism7 software and statistical significance was evaluated using the two-tailed Student's t-test for unpaired samples (\*p value  $\leq$  0.05, \*\*p  $\leq$  0.01, \*\*\*  $\leq$  0.001).

### 2.6.2. RBE calculation for cell survival

The dose response curve of X-ray irradiation was used in order to evaluate RBE for cell survival after irradiation with protons, lithium and carbon ions. The definition of the RBE is the ratio of the dose of reference radiation and the applied dose of a test radiation quality necessary to induce the same effect (cf. equation 1.5).

The X-ray dose response curve for cell survival  $S(D)$  can be described by Eq. 1.1.

The linear quadratic coefficients  $\alpha$ ,  $\beta$  and the corresponding error and covariance were evaluated from the fit to the data points.

The equivalent dose of the reference radiation was determined by inverting the fitted dose effect curve:

$$D(S) = \frac{-\alpha + \sqrt{\alpha^2 - 4\beta \ln S}}{2\beta} \quad \text{Eq. 2.8}$$

The error determination of the equivalent dose,  $\Delta_{\alpha,\beta} D$ , was calculated as:

$$(\Delta_{\alpha,\beta} D)^2 = \left(\frac{\partial D}{\partial \alpha} \Delta \alpha\right)^2 + \left(\frac{\partial D}{\partial \beta} \Delta \beta\right)^2 + \left(\frac{\partial D}{\partial S} \Delta S\right)^2 + 2 \frac{\partial D}{\partial \alpha} \frac{\partial D}{\partial \beta} \text{cov}(\alpha, \beta) \quad \text{Eq. 2.9}$$



### 3. Results

#### 3.1. Hit statistics

In a first step, the frequency for hitting a cell nucleus using different grid pattern was determined, since the microbeam irradiation in this work was performed sequentially in a regular pattern. For the evaluation of the hit probability for the particle irradiation using the microbeam, the nuclear area of the cells was of special importance. The nuclear size distribution of CHO-K1 cells measured from 128 cell nuclei is shown in Figure 3.1. The nuclear area had a mean value of  $(67.6 \pm 2.2) \mu\text{m}^2$  and a standard deviation of the distribution was  $24.8 \mu\text{m}^2$  (Friedrich *et al.*, Submitted). Assuming that the cell nucleus is geometrically formed as a circle with the measured area, the corresponding diameter was  $9.28 \mu\text{m}$ .

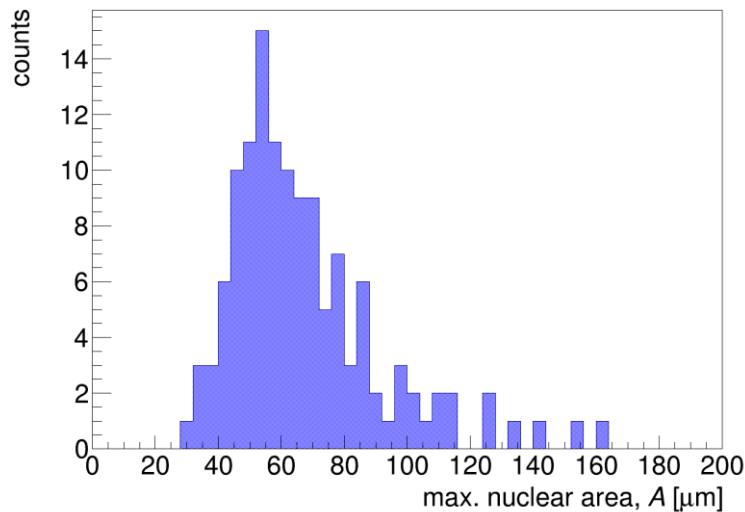


**Figure 3.1:** Nuclear size distribution of CHO-K1 cells measured from 128 cells.

The distribution of number of hits per cell nucleus was determined by Monte Carlo simulation and the results are shown in Figure 3.2. For the smallest grid size used in our irradiation experiments  $(3.82 \times 3.82) \mu\text{m}^2$  on average about 4.6 spots were applied to a cell nucleus. The exposure to the  $(5.4 \times 5.4) \mu\text{m}^2$  grid or to the  $(7.6 \times 7.6) \mu\text{m}^2$  grid resulted in a mean number of 2.3 or 1.2 hits per cell nucleus. The evaluated probability for the  $(7.6 \times 7.6) \mu\text{m}^2$  grid for unhit cells was 12 %,

whereas for the largest grid ( $10.8 \times 10.8$ )  $\mu\text{m}^2$  on average only 0.58 spots hit a cell nucleus and this irradiation grid pattern resulted in 44% of unhit cells.

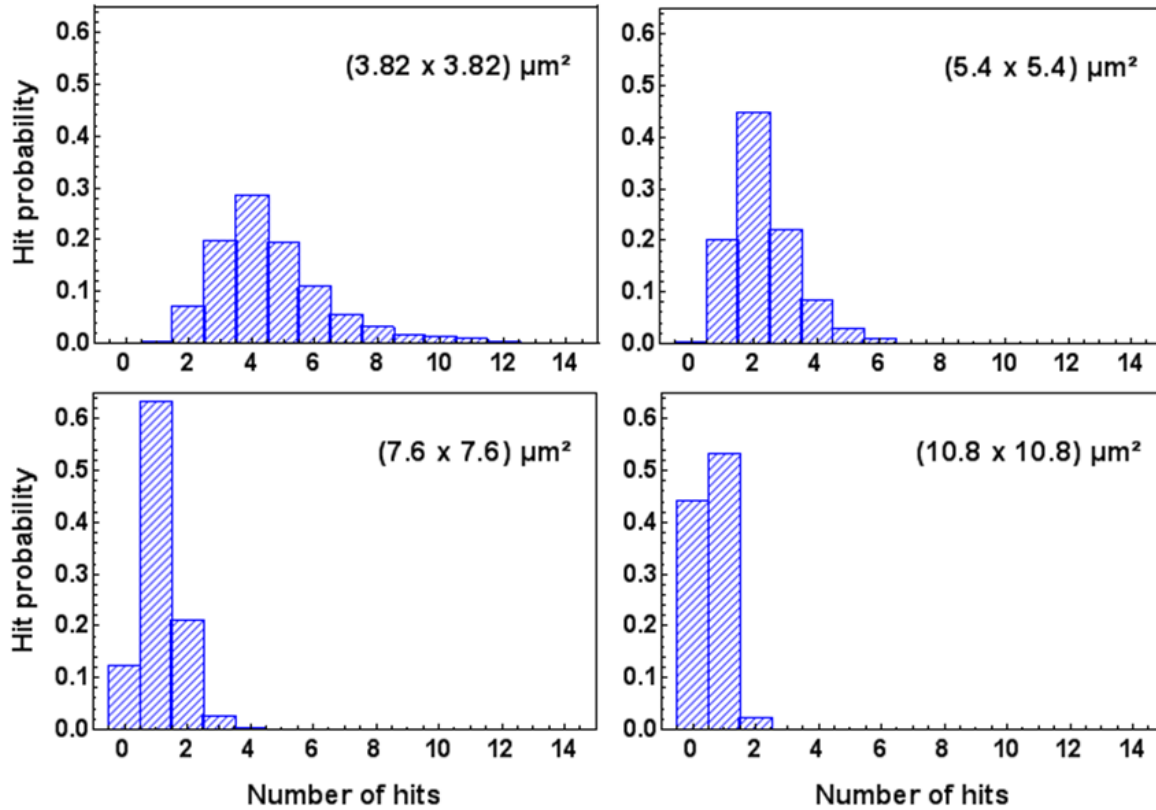


**Figure 3.2:** Distribution of number of hits for CHO- K1 cells using different grid pattern for the microbeam particle irradiation experiments at SNAKE.

Table 3.1 gives an overview of all used grid patterns with corresponding number of particles applied per point (ppp), the calculated average number of hits per cell nucleus and the percentage of unhit cells for each grid pattern.

The resulting hit statistics are essential data for all investigated end points in this work, thus this data have to be considered for the interpretation of the targeted effects of the microbeam irradiation.

**Table 3.1:** Overview of grid pattern used in the microbeam irradiation experiments at SNAKE with corresponding hit statistics.

Ion species	Grid pattern ( $\mu\text{m}^2$ )	Av. # spots/ nucleus	% of unhit cell nuclei
	random	-	0
<b>20 MeV protons</b>	5.4 x 5.4	2.32 $\pm$ 0.08	0.29
LET = (2.66 $\pm$ 0.13) keV/ $\mu\text{m}$	7.6 x 7.6	1.16 $\pm$ 0.04	12.2
	10.8 x 10.8	0.58 $\pm$ 0.02	44.4
	random	-	0
<b>33 MeV lithium ions</b>	3.82 x 3.82	4.63 $\pm$ 0.16	0
LET = (81 $\pm$ 8) keV/ $\mu\text{m}$	5.4 x 5.4	2.32 $\pm$ 0.08	0.29
	7.6 x 7.6	1.16 $\pm$ 0.04	12.2
	10.8 x 10.8	0.58 $\pm$ 0.02	44.4
<b>55 MeV carbon ions</b>	5.4 x 5.4	2.32 $\pm$ 0.08	0.29
LET = (338 $\pm$ 34) keV/ $\mu\text{m}$	7.6 x 7.6	1.19 $\pm$ 0.04	12.2
	10.7 x 10.7	0.60 $\pm$ 0.02	44.4

## 3.2. Analysis of DNA DSB repair after microbeam particle irradiation at SNAKE

### 3.2.1. Immunofluorescence staining of $\gamma$ -H2AX

Qualitative verification of the radiation induced DNA damage within cell nuclei was performed by the immunofluorescence staining of DNA DSBs using the antibody against phosphorylated H2AX (Friedrich *et al.*, Submitted). Figure 3.3 shows immunofluorescence staining of the  $\gamma$ -H2AX foci pattern after proton irradiation with a mean dose of 1.7 Gy obtained 30 minutes post-irradiation. CHO-K1 cells shown in Figure 3.3 (a) were exposed to a homogeneous proton irradiation, and the obtained  $\gamma$ -H2AX foci pattern was randomly distributed within the cell nuclei. The  $\gamma$ -H2AX foci pattern shown in Figure 3.3 (b, c, d) represents the DNA DSB distribution after exposure to

protons focused to spots of three different grid patterns. Figure 3.3 (b) represents the  $\gamma$ -H2AX foci pattern obtained after focusing 117 protons to spots of the  $(5.4 \times 5.4) \mu\text{m}^2$  grid. Here, the  $\gamma$ -H2AX foci within a cell nucleus were localized to irradiation spots and a similar damage pattern was observed also after irradiation using wider grids (cf. Figure 3.3 c- d). The size of the localized DNA damage spots increased slightly with increasing the number of focused protons per spot. The DNA DSB pattern as shown by  $\gamma$ -H2AX staining reflected qualitatively the irradiation pattern using different spot applications.

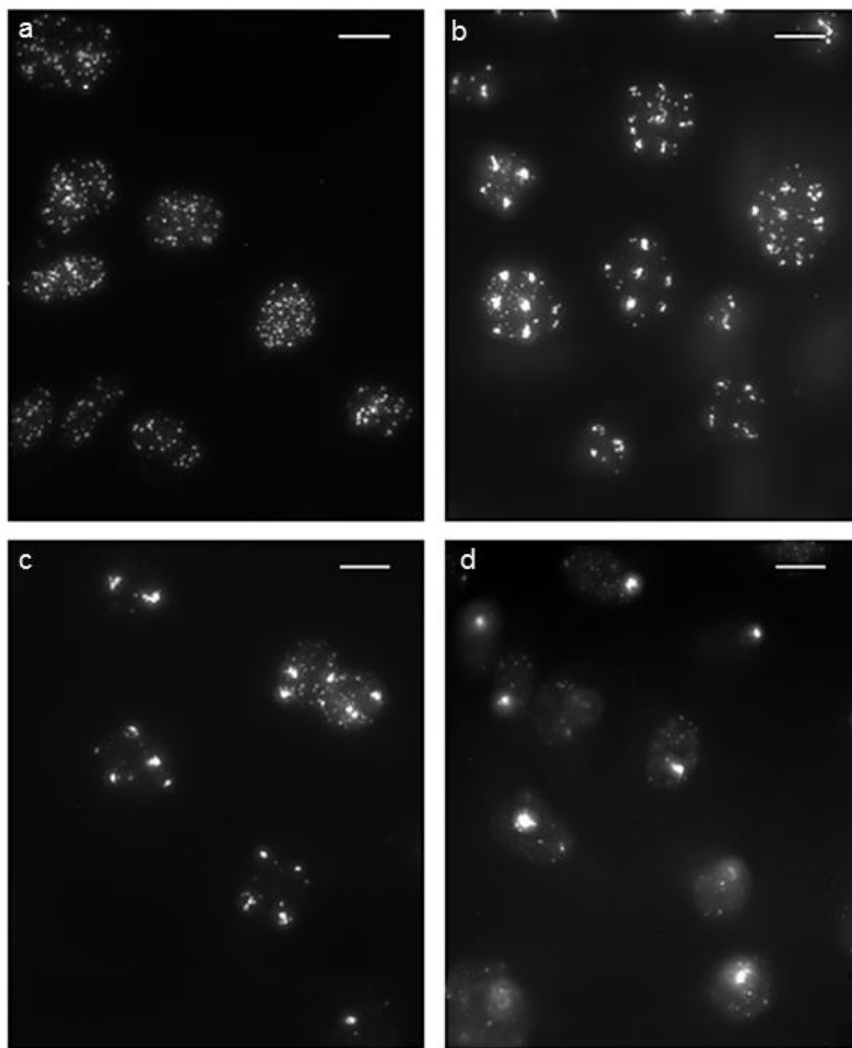


**Figure 3.3:** CHO-K 1 cells after immunofluorescence staining of  $\gamma$ -H2AX 30 minutes after irradiation with an average dose of 1.7 Gy (scale bar: 10  $\mu\text{m}$ ): a)  $\gamma$ -H2AX foci pattern from 20 MeV protons applied quasi homogeneously, b)  $\gamma$ -H2AX foci pattern from 117 protons focused to spots of the  $(5.4 \times 5.4) \mu\text{m}^2$  grid, c)  $\gamma$ -H2AX foci pattern from 234 protons focused to spots of the  $(7.6 \times 7.6) \mu\text{m}^2$  grid and d)  $\gamma$ -H2AX foci from 468 protons focused to spots of the  $(10.8 \times 10.8) \mu\text{m}^2$  grid.

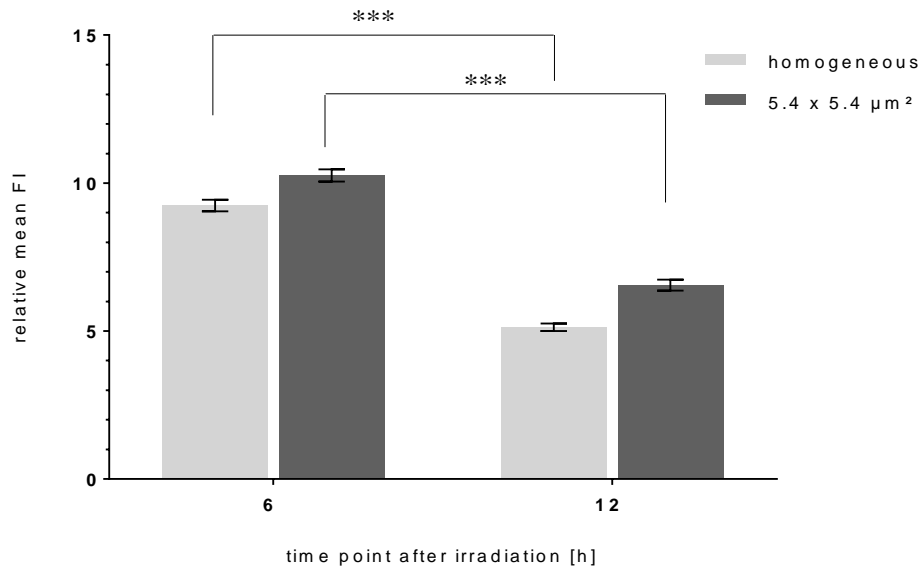
### **3.2.1.1. Flow cytometric analysis of $\gamma$ -H2AX repair kinetics**

High LET radiation is densely ionizing radiation, which induces multiple DSBs in close proximity along the ion track. These enhanced local densities of DSBs induced after irradiation with heavy ions make the analysis of  $\gamma$ -H2AX repair by foci counting impossible. In order to quantify the  $\gamma$ -H2AX repair kinetics after irradiation with protons and carbon ions, a more appropriate kind of analysis has been chosen, namely flow cytometric measurement of the mean  $\gamma$ -H2AX fluorescence intensity (FI). To analyze DSB repair in cells after homogeneous and focused proton irradiation, the  $\gamma$ -H2AX mean FI was measured 6 and 12 hours after irradiation. For the cell irradiation with carbon ions the full  $\gamma$ -H2AX repair kinetics at six different time points was assessed.

### **3.2.1.2. Effects of focused low LET proton irradiation on $\gamma$ -H2AX repair kinetics**

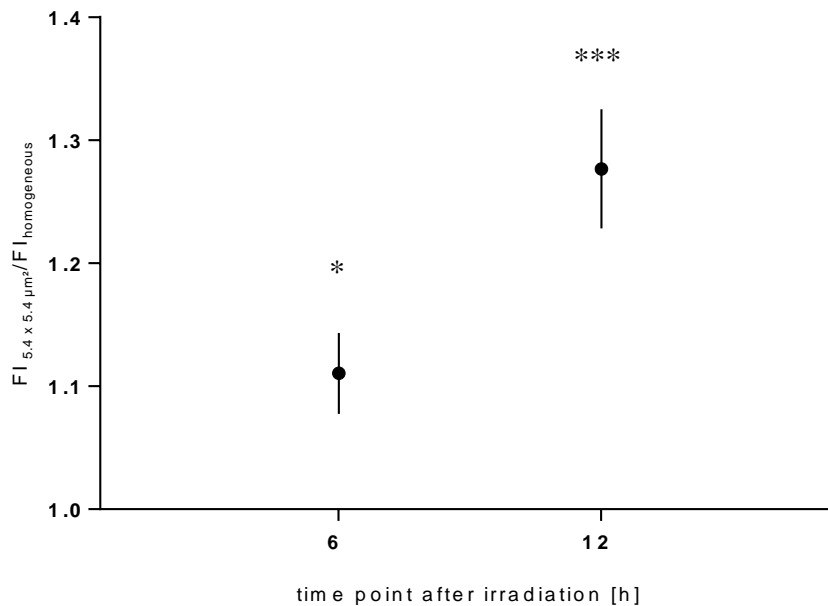
CHO-K1 cells were irradiated either with homogeneously applied protons or with protons focused to spots of the (5.4 x 5.4)  $\mu\text{m}^2$  grid. In both irradiation cases a mean dose of 3.4 Gy was used. The  $\gamma$ -H2AX FI was measured in unirradiated (sham) and irradiated cells, 6 and 12 hours post-irradiation. For each radiation mode four technical replicates were measured.

Figure 3.4 shows the mean  $\gamma$ -H2AX FI measured in irradiated cells which was normalized to the background expression of  $\gamma$ -H2AX obtained from unirradiated cells. A time-dependent reduction of the mean  $\gamma$ -H2AX FI could be observed after cell irradiation with random and focused protons. For both irradiation modalities less  $\gamma$ -H2AX FI was detected 12 hours after irradiation than after 6 hours ( $p$ -value < 0.0001).



**Figure 3.4:** The mean  $\gamma$ -H2AX fluorescence intensity (FI) relative to the unirradiated samples measured 6 and 12 hours after exposure to homogeneous and focused proton irradiation using a mean radiation dose of 3.4 Gy. Error bars for the data points represent the standard error of the mean (SEM) of four technical repeats. Significance: \*\*\* $p \leq 0.001$ .

To further elucidate the effects of the focused proton irradiation in comparison to a homogeneous irradiation, the ratio of the mean FI between these two irradiation modalities was evaluated as shown in Figure 3.5. The residual mean  $\gamma$ -H2AX FI measured 6 hours after irradiation with focused protons was 11% higher ( $p$ -value = 0.0122) as compared to homogeneous proton irradiation. The difference in loss of  $\gamma$ -H2AX between focused and random proton irradiation became even more pronounced with time. The residual mean  $\gamma$ -H2AX FI measured in cells 12 hours after focused proton irradiation was 28% higher ( $p$ -value = 0.0008) than the residual mean  $\gamma$ -H2AX FI in cells after homogeneous proton irradiation.



**Figure 3.5:** The ratio of the mean  $\gamma$ -H2AX fluorescence intensity (FI) measured in cells 6 and 12 h after focused and homogeneous proton irradiation using a mean radiation dose of 3.4 Gy. Error bars for the data points represent SEM of four technical repeats. Significance: \* $p$ -value  $\leq 0.05$ ; \*\*\* $p \leq 0.001$ .

### 3.2.1.3. Effects of high LET carbon ion irradiation on $\gamma$ -H2AX repair kinetics

A similar experiment was performed with high LET carbon ions using the same mean dose of 3.4 Gy as for proton irradiation. Two carbon ions per point were applied to spots of the (5.4 x 5.4)  $\mu\text{m}^2$  grid and cells were fixed at six different time points after irradiation, from 15 minutes to 24 hours. For each time point at least three replicates were measured from which a mean value was calculated. The background mean  $\gamma$ -H2AX FI measured in unirradiated cell samples was subtracted from the irradiated cell samples. Figure 3.6 displays the mean  $\gamma$ -H2AX FI measured in cells over time after focused carbon ion irradiation. A time-dependent reduction of the mean  $\gamma$ -H2AX FI could be observed. The mean  $\gamma$ -H2AX FI measured 24 hours after irradiation with carbon ions was still detectable. The relative mean  $\gamma$ -H2AX FI measured 6 and 12 hours after focused carbon ion irradiation was much higher as compared to the focused proton irradiation as shown in Figure 3.4.

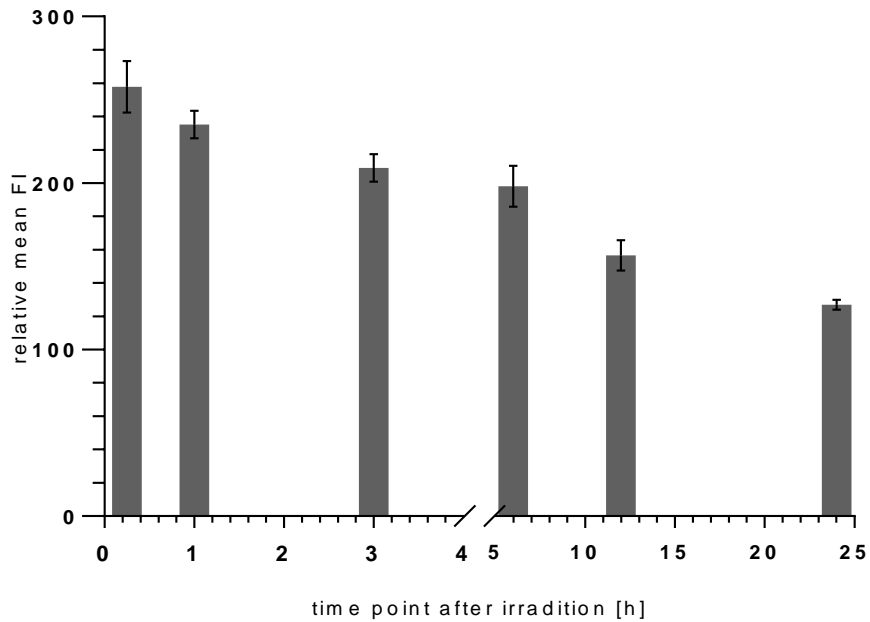


**Figure 3.6:** Relative mean  $\gamma$ -H2AX fluorescence intensity (FI) measured in CHO-K1 cells at different time points after carbon ion irradiation with a mean dose of 3.4 Gy. Error bars for the data points represent SEM of three technical repeats.

In order to describe quantitatively the fluorescence intensity reduction of  $\gamma$ -H2AX with time, the following bi-exponential equation has been chosen:

$$I(t) = \left[ r \cdot \exp\left(-\frac{t-15 \text{ min}}{\tau_1}\right) + (1-r) \cdot \exp\left(-\frac{t-15 \text{ min}}{\tau_2}\right) \right] \quad \text{Eq. 3.1}$$

The  $\gamma$ -H2AX FI reduction is a two phase decay process, with two different constant rates: the slow repair kinetics, which is linked to the repair of complex DNA damage and fast repair kinetics related to simple DNA damage. Correspondingly,  $r$  represents the amount of simpler damage with its decay rate  $\tau_1$ , whereas  $(1-r)$  represents the more complex damage with a decay rate  $\tau_2$ . The data shown in Figure 3.6 were normalized to the maximum FI found to be reached 15 min after irradiation in CHO-K1 cells and biphasic repair kinetics of CHO-K1 cells after irradiation with carbon ions is shown in Figure 3.7. The evaluated value for  $\tau_1$  and  $\tau_2$  was  $(9.8 \pm 0.8)$  h and  $(3 \pm 51) 10^6$  h, respectively. The calculated decay rate representing the slow repair  $\tau_2$  is very high.



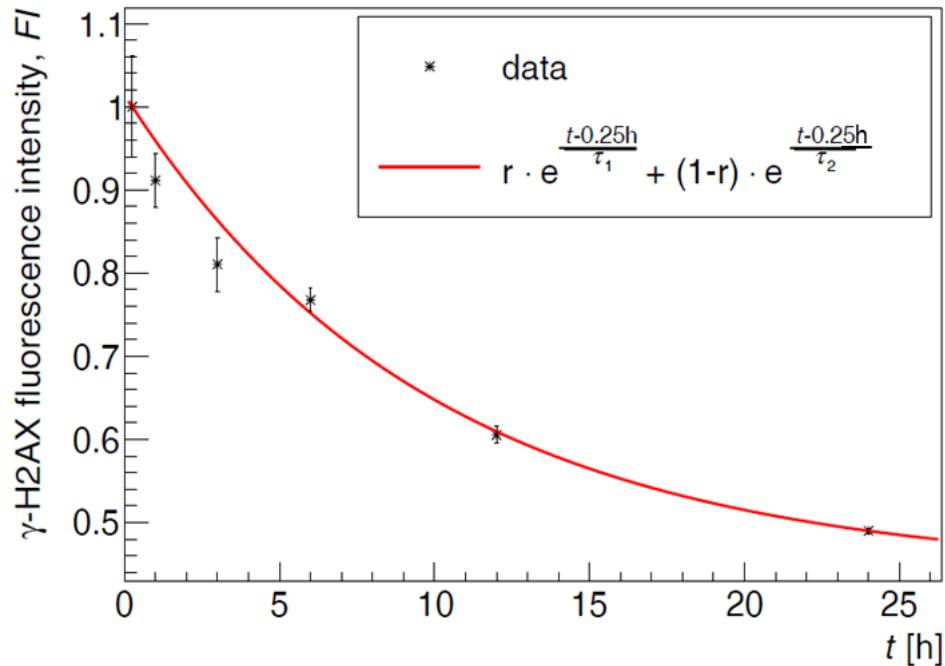


**Figure 3.7:**  $\gamma$ -H2AX fluorescence intensity measured after carbon ion radiation over time relating to 15 min post radiation with a mean dose of 3.4 Gy. The data points are fitted by a bi-exponential decrease function with one fast and one slow repair component. Error bars for the data points represent SEM of three technical repeats.

### 3.3. Analysis of radiation induced apoptosis by flow cytometric measurement of Caspase 3/7 activity

A further question to be assessed in this work is whether changing spatial dose distribution by focusing protons affects apoptosis induction. Focused proton application was compared to homogeneous proton and carbon ion irradiation. In order to investigate apoptosis induction in CHO-K1 cells the activation of caspase 3/7 following irradiation was measured using flow cytometry.

Flow cytometric investigation of apoptotic cells was carried out by measuring the percentage of cells containing activated caspase 3/7 in their cytoplasm. The assay works with non-fixed cells, therefore the analysis of caspase 3/7 activity can be combined with live/dead cell staining dye SYTOX, which is incorporated into the DNA of dead cells. This allows a clear distinction of apoptotic cells from dead cells.

### 3.3.1. Measurement of Caspase 3/7 activity after X-ray irradiation

The percentage of caspase 3/7 positive cells, SYTOX positive cells and cells positive for both caspase 3/7 and SYTOX (double positive) was evaluated 24 and 48 hours after irradiation with 3.4 Gy and 5.1 Gy of 200 kV X-rays. The radiation dose for the microbeam irradiation at SNAKE was limited due to technical properties of the microbeam to 3.4 Gy for protons and 5.1 Gy for carbon ions. Therefore, the same radiation doses were also used in the experiments with X-rays in order to compare the effects of different radiation qualities at the same radiation dose.

The data from the X-ray irradiation are presented in Figure 3.8. For both examined time points the percentage of caspase 3/7 positive, double positive and SYTOX positive cells was evaluated in the unirradiated cell samples (sham). The rate of caspase 3/7 positive cells did not change with incubation time. However, the percentage of double positive cells measured after 48 hours increased from 2.2 % to 7 % ( $p$ -value = 0.0038).

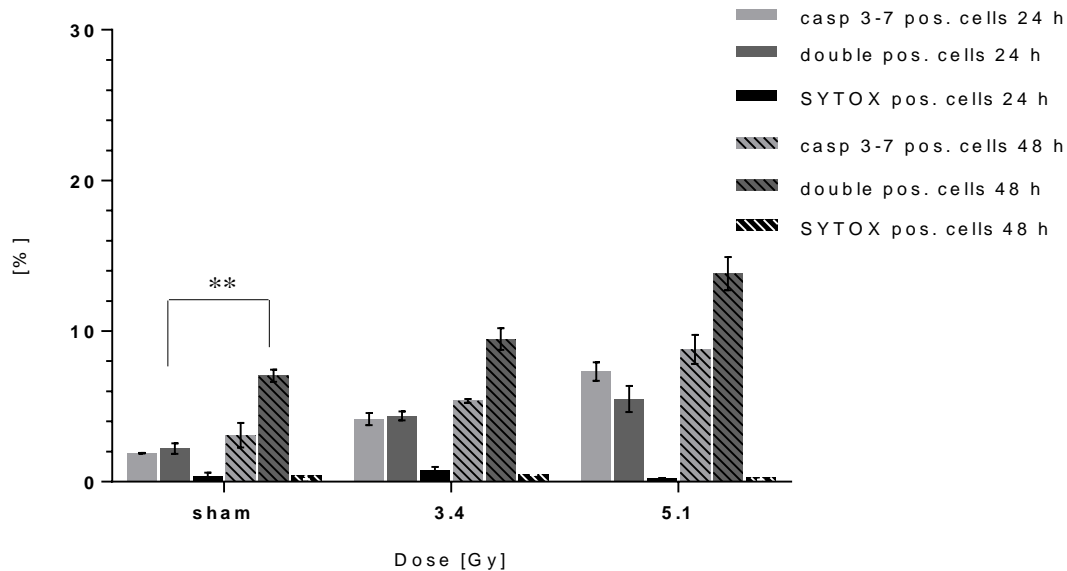


**Figure 3.8:** Percentage of caspase 3/7 positive, double (caspase 3/7 and SYTOX) positive and SYTOX positive cells 24 and 48 hours after irradiation with 3.4 and 5.1 Gy of 200 kV X-Rays. Sham cell samples were used as negative control without radiation treatment. Error bars for the data points represent SEM of two independent experiments. Significance: \*\* $p \leq 0.01$ .

In order to elucidate solely the radiation effects on apoptosis induction in CHO-K1 cells, the evaluated apoptotic rate from the unirradiated cell samples was subtracted from the irradiated cell samples.

The relative percentage of caspase 3/7 positive, SYTOX positive and double positive cells for both examined time points after irradiation with X-rays are shown in Figure 3.9. After irradiation with 3.4 Gy of X-rays, there was no difference in the apoptotic rate with regard to the incubation time. For both time points about 2.3 % of caspase 3/7 positive and double positive cells were measured. When increasing the radiation dose to 5.1 Gy, the percentage of caspase 3/7 positive cells measured at 24 and 48 hours after irradiation increased to 5.4 % ( $p$ -value = 0.0125) and 5.7 % ( $p$ -value = 0.0842), respectively. The percentage of double positive cells changed only 48 hours after irradiation with 5.1 Gy, as the percentage of double positive cells increased from 2.4% to 6.8% ( $p$ -value = 0.0392). SYTOX positive cells were almost not detectable throughout the experiment.

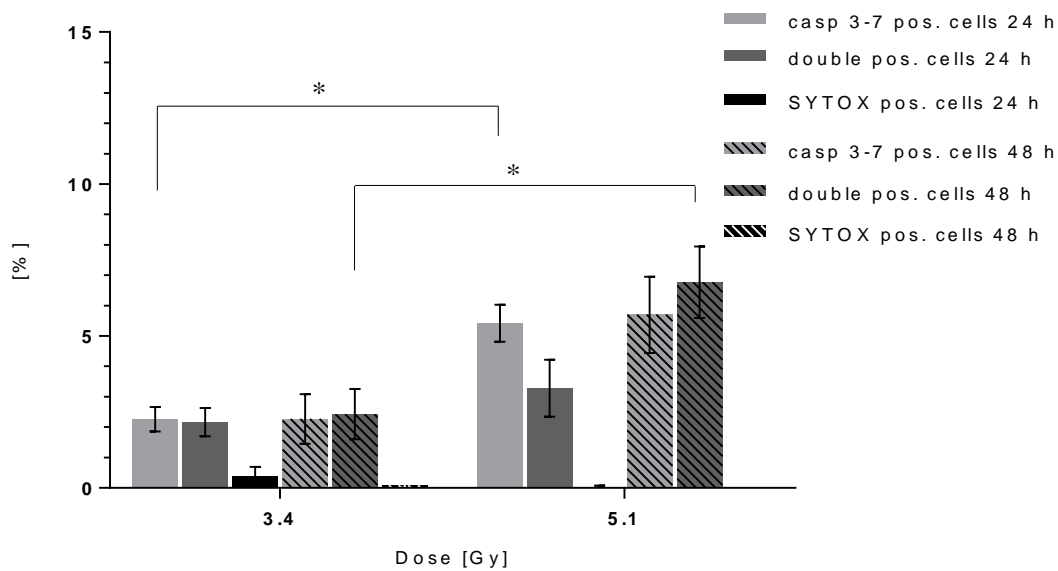


**Figure 3.9:** Percentage of caspase 3/7 positive, double (caspase 3/7 and SYTOX) positive and SYTOX positive cells relative to unirradiated cell samples 24 and 48 hours after irradiation with 3.4 and 5.1 Gy of 200 kV X-Rays. Error bars for the data points represent SEM of two independent experiments. Significance: \* $p$ -value  $\leq 0.05$ .

### 3.3.2. Measurement of Caspase 3/7 activity after irradiation with 20 MeV protons

CHO-K1 cells were irradiated with 20 MeV protons, which were applied either homogeneously or focused using three different combinations of grid patterns. The mean dose used for all four irradiation modalities in the experiment was 3.4 Gy. The flow cytometric analysis of apoptosis induction in cells was measured 24 hours after irradiation. The obtained data from the proton irradiation are shown in Figure 3.10. In unirradiated cells 4% of caspase 3/7 positive and roughly 20 % of double positive cells were measured.

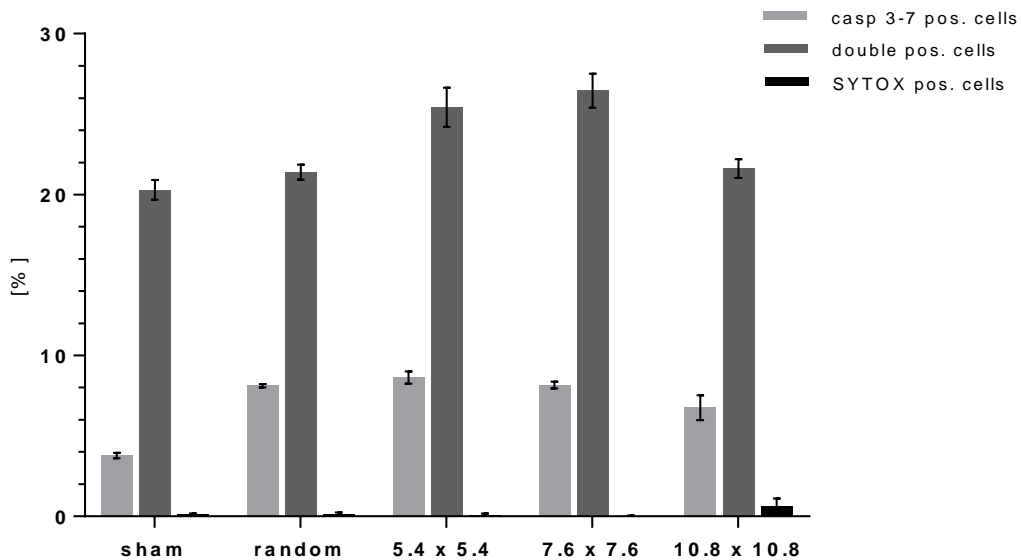


**Figure 3.10:** Percentage of caspase 3/7 positive, double (caspase 3/7 and SYTOX) positive and SYTOX positive cells evaluated 24 hours after irradiation with homogeneous or focused 20 MeV protons (by focusing 234, 468, 936 protons in the (5.4 x 5.4), (7.6 x 7.6) and (10.8 x 10.8)  $\mu\text{m}^2$  grid). For all irradiation modalities a mean dose of 3.4 Gy was used. Sham cell samples were used as negative control without radiation treatment. Error bars for the data points represent SEM of five technical replicates.

The caspase values for unirradiated cells were subtracted from those obtained from the irradiated cell samples in order to obtain relative values for each irradiation modality as shown in Figure 3.11. After exposure of CHO-K1 cells to homogeneous proton irradiation the percentage of caspase 3/7 positive cells increased by ~ 4 % as compared to the unirradiated cells. However, no increase in the percentage of double positive cells was seen. After focused proton irradiation using three different grid patterns the percentage of double positive cells increased to 5.1 % (5.4 x 5.4)

( $p$ -value = 0.034), 6.2% (7.6 x 7.6) ( $p$ -value = 0.0082) and to 1.3% (10.8 x 10.8) ( $p$ -value = 0.851) as compared to random proton irradiation. The highest percentage of double positive cells was measured after focused proton irradiation using the (5.4 x 5.4)  $\mu\text{m}^2$  and (7.6 x 7.6)  $\mu\text{m}^2$  grids. There was no difference when comparing the effect of the focused proton irradiation to random irradiation considering only the caspase 3/7 positive cell population. The percentage of double positive cells after irradiation with 468 protons focused to spots of the (7.6 x 7.6)  $\mu\text{m}^2$  grid remained almost unchanged in comparison with the narrower grid. Using the widest grid with (10.8 x 10.8)  $\mu\text{m}^2$  for cell irradiation the evaluated apoptotic rate showed a decreasing tendency as compared to both narrower grids. The percentage of SYTOX positive cells in all measured cell samples was below 1%.

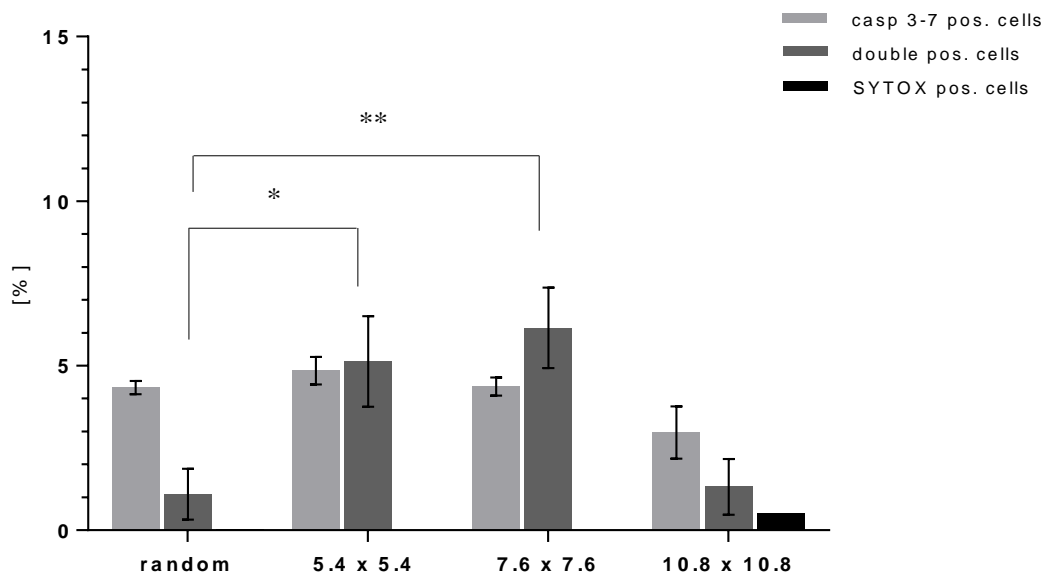


**Figure 3.11:** Percentage of caspase 3/7 positive, double (caspase 3/7 and SYTOX) positive and SYTOX positive cells relative to unirradiated cell samples 24 hours after irradiation with 20 MeV protons, applied either randomly or by focusing protons in the (5.4 x 5.4), (7.6 x 7.6) and (10.8 x 10.8)  $\mu\text{m}^2$  grid. For all irradiation modalities a mean dose of 3.4 Gy was used. Error bars for the data points represent SEM of five technical replicates. Significance: \* $p$ -value  $\leq 0.05$ , \*\* $p$ -value  $\leq 0.01$ .

### 3.3.3. Measurement of Caspase 3/7 activity after irradiation with 55 MeV carbon ions

Caspase 3/7 activity was analyzed in cells after exposure to carbon ion radiation in order to compare the effects of homogeneous and focused proton irradiation with high LET radiation effects. Two and three carbon ions were applied to spots of the (5.4 x 5.4)  $\mu\text{m}^2$  grid, resulting in a mean radiation dose of 3.4 Gy and 5.1 Gy. About 4% caspase 3/7 positive and about 9% double positive cells were evaluated in the unirradiated cell samples as shown in Figure 3.12.

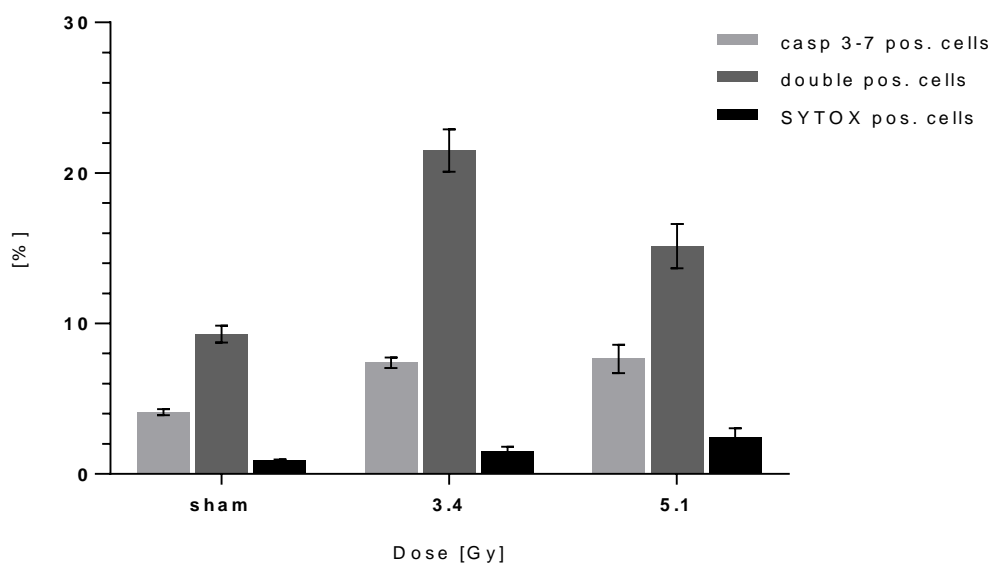


**Figure 3.12:** Percentage of caspase 3/7 positive, double (caspase 3/7 and SYTOX) positive and SYTOX positive cells evaluated 24 hours after irradiation with 55 MeV carbon ions, applied by focusing two or three carbon ions in the (5.4 x 5.4)  $\mu\text{m}^2$  grid using a mean dose of 3.4 Gy or 5.1 Gy. Sham cell samples were used as negative control without radiation treatment. Error bars for the data points represent SEM of two independent experiments.

Figure 3.13 presents caspase 3/7 data of irradiated samples relative to their unirradiated matched samples. Cell irradiation with two carbon ions per point and a mean dose of 3.4 Gy resulted in 3.3 % caspase 3/7 positive, and 12.2 % double positive cells. Increasing the radiation dose to 5.1 Gy did not show a change in the percentage of caspase 3/7 positive cells, whereas the percentage of double positive cells decreased to 5.8 % ( $p$ -value = 0.0236). For both radiation doses no significant change in the percentage of SYTOX positive cells could be observed.

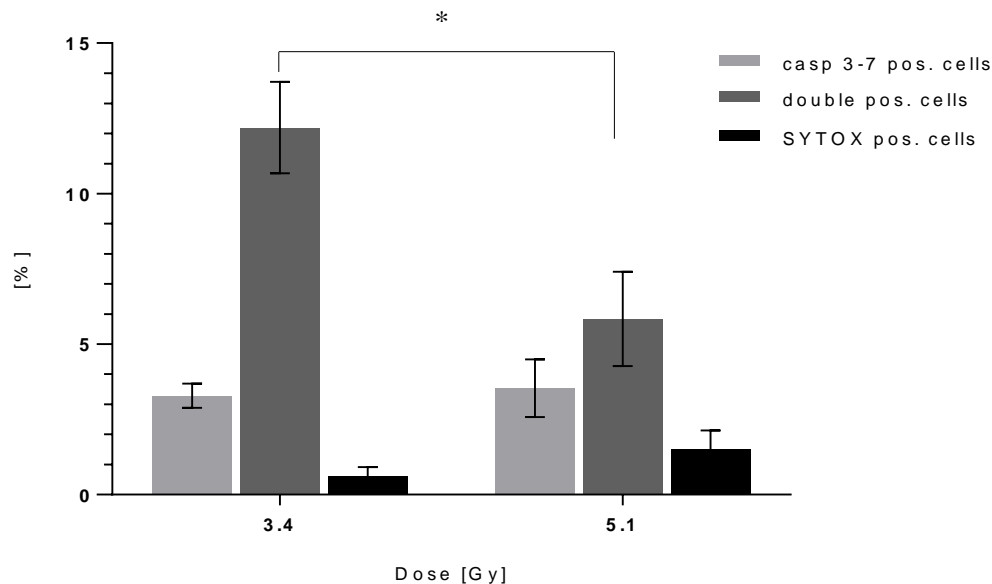


**Figure 3.13:** Percentage of caspase 3/7 positive, double (caspase 3/7 and SYTOX) positive and SYTOX positive cells relative to the unirradiated cells 24 hours after irradiation with 55 MeV carbon ions, applied by focusing two or three carbon ions in a 5.4 x 5.4 grid using a mean dose of 3.4 Gy or 5.1 Gy. Error bars for the data points represent SEM of two independent experiments. Significance: \* $p \leq 0.05$ .

### 3.3.4. Comparison of measured apoptosis induction using different radiation qualities

Figure 3.14 shows caspase 3/7 results evaluated 24 hours after irradiation with a mean dose of 3.4 Gy X-rays, 20 MeV protons (applied either randomly or focused), and focused 55 MeV carbon ions. The results were normalized to the corresponding sham background values obtained in each irradiation experiment. Using radiation qualities with various LET values, significant differences in the percentage of double positive cells only could be observed. A higher frequency of double positive cells was measured after focused proton (6.2 %) ( $p$ -value = 0.0034) and carbon ion irradiation (12.2 %) ( $p$ -value = 0.0002) as compared to random proton irradiation (1.1%). However, the percentage of double positive cells after high LET carbon ion irradiation was significantly higher as compared to focused proton irradiation ( $p$ -value = 0.0106).

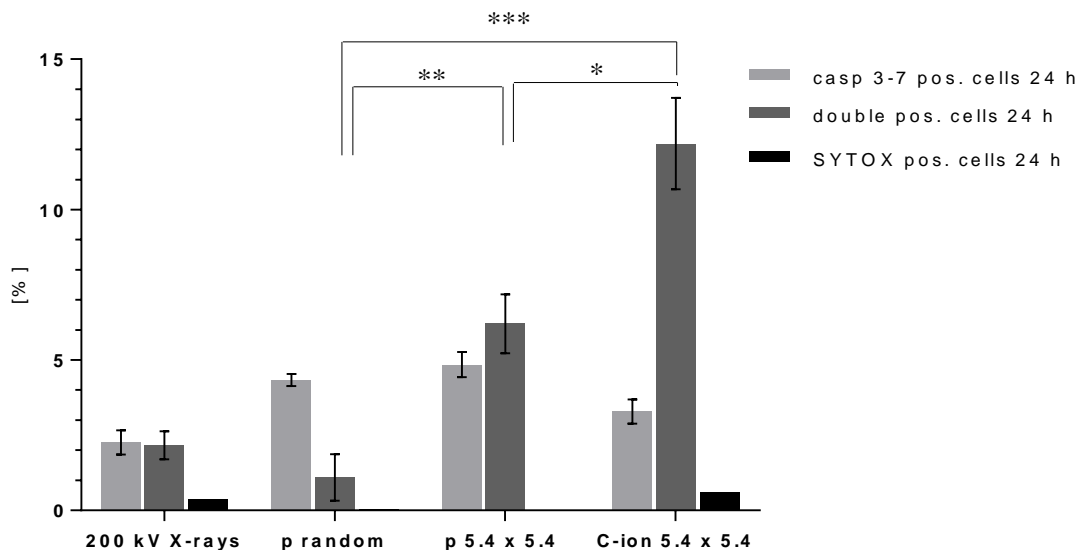


**Figure 3.14:** Percentage of caspase 3/7 positive, double (caspase 3/7 and SYTOX) positive and SYTOX positive cells relative to the unirradiated cells 24 hours after irradiation with 200 kV X-rays, 20 MeV protons (applied randomly and focused) and focused 55 MeV carbon ions, using a mean dose of 3.4 Gy. Error bars for the data points represent SEM of either two independent experiments (X-ray and carbon ion irradiation) or five technical repeats (proton irradiation). Significance: \*  $p \leq 0.05$ ; \*\*  $p \leq 0.01$ ; \*\*\*  $p \leq 0.001$ .

### 3.4. Clonogenic cell survival

One of the most important biological end points used in radiobiological research is clonogenic cell survival. This assay describes the relation between the radiation dose and the fraction of cells that survive the radiation treatment. In the following section the cell survival data after particle irradiation using the microbeam at SNAKE as well as the data obtained from the reference radiation with X-rays are presented. Microbeam irradiation was performed using protons, lithium ions and carbon ions. Cells were exposed to a random particle irradiation or to a grid-like irradiation pattern where a certain number of particles were focused to spots in cell nuclei. The varying patterns were used to assess the influence of the different spatial dose distribution on the RBE, with respect to the clonogenic cell survival. The measured cell survival was compared with the model predictions obtained using the biophysical local effect model (LEM)(Friedrich *et al.*, Submitted).



### 3.4.1. Dose response curve with X- rays

In order to characterize the radiation sensitivity of CHO-K1 cells, the dose-response curves using 200 kV X-rays were generated. The dose-response curve with X-rays was used as a reference irradiation type in this work for the calculation of the RBE. Furthermore, the dose-response coefficients were used as input parameters for the calculation of the LEM predictions. Figure 3.15 shows the survival fraction of CHO-K1 cells, evaluated after exposure of cells to doses from 0.5 Gy to 8 Gy obtained from two independent experiments from different beam times. From each experiment at least 3 replicates were measured for the same radiation dose.

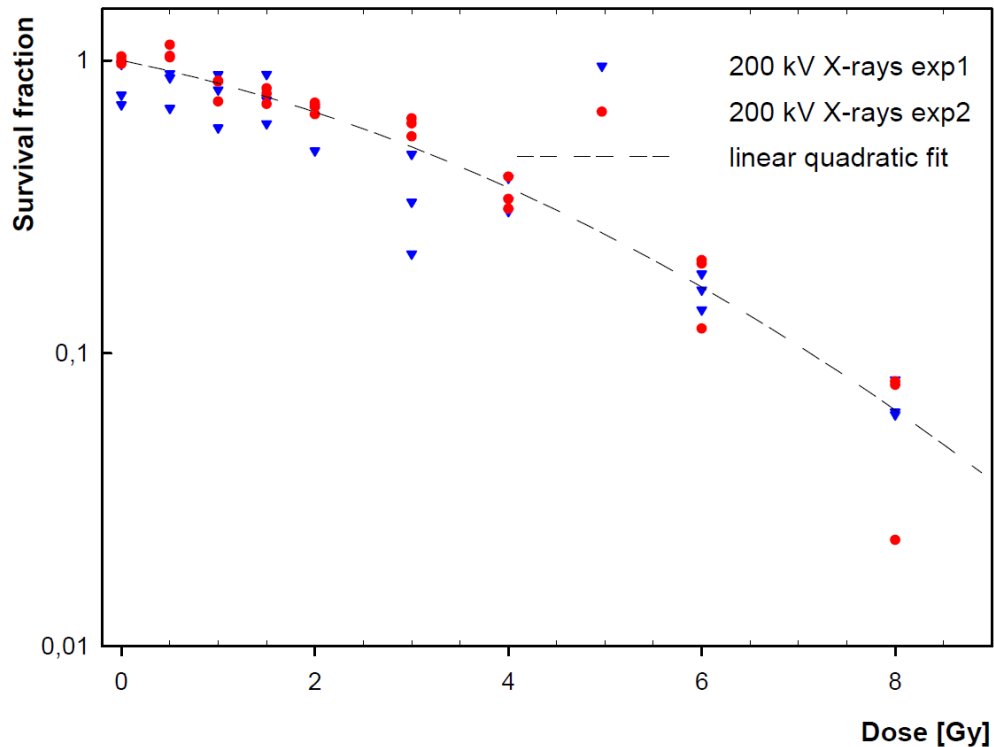


**Figure 3.15:** Cell survival curves of CHO-K1 cells obtained after exposure to different X-ray doses in two independent experiments (red and blue data points) from at least three replicates. A common linear quadratic fit curve derived from mean linear quadratic parameters is marked by a dashed line.

The data of replicates from two experiments were fitted individually using a second degree polynomial equation (cf. Eq. 1.4). The linear quadratic coefficients,  $\alpha$ ,  $\beta$  and covariance were determined from each experiment (Table 3.2). The calculated linear quadratic parameters were averaged and mean values  $\alpha = 0.1559 \pm 0.0449 \text{ Gy}^{-1}$ ,  $\beta = 0.02347 \pm 0.00552 \text{ Gy}^{-2}$ ,  $\text{cov}(\alpha, \beta) = -0.000238192 \text{ Gy}^{-3}$  were later used for the calculation of the RBE and LEM predictions.

**Table 3.2:** Calculated linear-quadratic parameters of the dose- response cell survival curve for CHO-K1 cells.

	Exp 1	Exp 2	Averaged values Exp 1 and Exp 2
$\alpha$	$0.190535 \pm 0.0600058 \text{ Gy}^{-1}$	$0.121315 \pm 0.0668485 \text{ Gy}^{-1}$	$0.15592 \pm 0.044915 \text{ Gy}^{-1}$
$\beta$	$0.016126 \pm 0.0073737 \text{ Gy}^{-2}$	$0.030833 \pm 0.008214 \text{ Gy}^{-2}$	$0.02347 \pm 0.005519 \text{ Gy}^{-2}$
$\text{cov}(\alpha, \beta)$	$-0.000425139 \text{ Gy}^{-3}$	$-0.000527629 \text{ Gy}^{-3}$	$-0.000238192 \text{ Gy}^{-3}$
$\text{cor}(\alpha, \beta)$	-0.960832	-0.960832	-0.960832

### 3.4.2. Microbeam particle irradiation at SNAKE

Clonogenic cell survival experiments were performed with low LET 20 MeV protons (LET= 2.66 keV/ $\mu\text{m}$ ), intermediate LET 33 MeV lithium ions (LET= 81 keV/ $\mu\text{m}$ ) and high LET 55 MeV carbon ions (LET=338 keV/ $\mu\text{m}$ ). Since these three particles differ in their LET, the entire range from low- to high LET radiation has been covered. CHO-K1 cells were exposed at SNAKE either to a homogeneous particle irradiation or to a grid-like irradiation pattern, where at each spot a certain number of particles were focused to a spot size of about (0.6 x 1.2)  $\mu\text{m}^2$ . Several variations of grid patterns were chosen with a different number of particles applied per point (ppp), while maintaining a mean dose of  $\sim 1.7 \text{ Gy}$  in all irradiation modalities. The mean dose was the same in all irradiation cases, however the spatial distribution of DSBs was varied. Table 3.3 gives an overview of the grid patterns used for particle irradiation with their corresponding LET, number of particles applied per spot and the applied dose to the cell nucleus.

**Table 3.3:** Overview of grid pattern used in the microbeam irradiation experiments at SNAKE with detailed information on the number of particles per point (ppp), spot LET and the applied dose to the cell nucleus.

Ion species	Grid pattern ( $\mu\text{m}^2$ )	Particles per point (ppp)	Spot LET (keV/ $\mu\text{m}$ )	Dose to nucleus (Gy)
<b>20 MeV protons</b> LET = (2.66 $\pm$ 0.13) keV/ $\mu\text{m}$	random	-	-	1.70 $\pm$ 0.09
	5.4 x 5.4	117	311 $\pm$ 16	1.71 $\pm$ 0.09
	7.6 x 7.6	234	621 $\pm$ 31	1.71 $\pm$ 0.09
	10.8 x 10.8	468	1242 $\pm$ 62	1.71 $\pm$ 0.09
<b>33 MeV lithium ions</b> LET = (81 $\pm$ 8) keV/ $\mu\text{m}$	random	-	-	1.70 $\pm$ 0.17
	3.82 x 3.82	2	161 $\pm$ 16	1.77 $\pm$ 0.18
	5.4 x 5.4	4	322 $\pm$ 32	1.77 $\pm$ 0.18
	7.6 x 7.6	8	645 $\pm$ 65	1.77 $\pm$ 0.18
<b>55 MeV carbon ions</b> LET = (338 $\pm$ 34) keV/ $\mu\text{m}$	10.8 x 10.8	16	1290 $\pm$ 130	1.77 $\pm$ 0.18
	5.4 x 5.4	1	338 $\pm$ 34	1.86 $\pm$ 0.19
	7.6 x 7.6	2	676 $\pm$ 68	1.90 $\pm$ 0.19
	10.7 x 10.7	4	1353 $\pm$ 135	1.91 $\pm$ 0.19

### 3.4.2.1. Proton irradiation

Figure 3.16 represents cell survival after irradiation with protons applied either homogeneously or by focusing a certain number of protons to sub-micrometer spots. Here, the cell survival is plotted against the spot LET, i.e. the sum of the LET of all particles within a microbeam spot. The data points are the mean values from two independently performed experiments from different beam times. For each irradiation modality at least nine replicates were measured.

Cell exposure to a mean dose of 1.7 Gy of homogeneously applied protons resulted in 75 % cell survival. After focusing 117 protons to spots of the (5.4 x 5.4)  $\mu\text{m}^2$  grid, the cell survival rate was significantly reduced to 39 % ( $p$ -value  $\leq 0.0001$ ). For focused proton irradiation using wider grids (7.6 x 7.6)  $\mu\text{m}^2$  and (10.8 x 10.8)  $\mu\text{m}^2$  the cell survival remained almost unchanged with 41 % and 42 % with respect to the narrow grid, (5.4 x 5.4)  $\mu\text{m}^2$ . The decrease in cell survival was significant for both wide grids in comparison to homogeneous proton irradiation ( $p$ -value  $\leq 0.0001$ ).

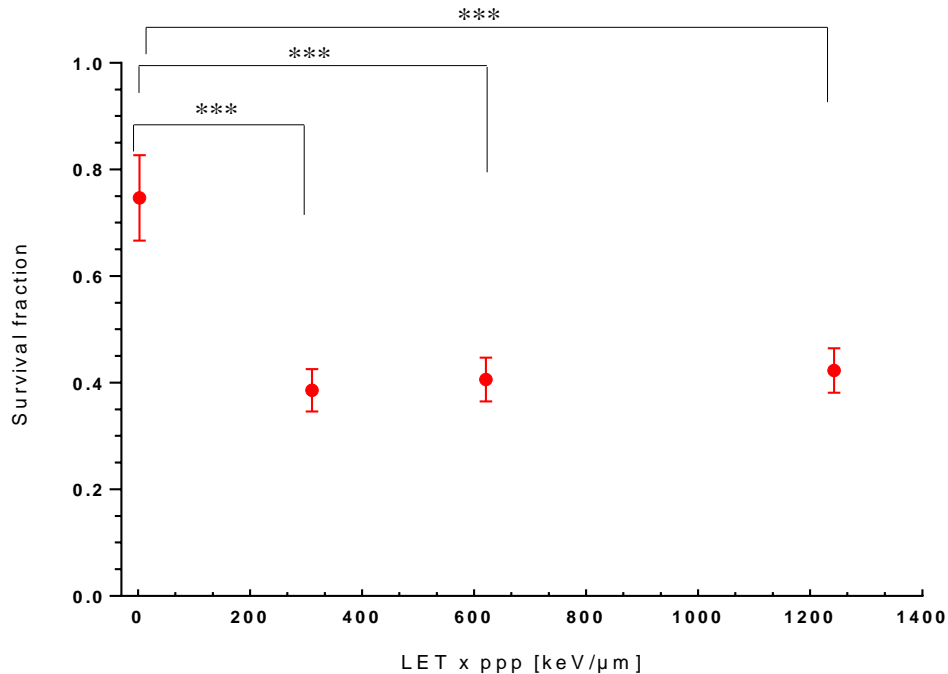


**Figure 3.16:** Cell survival of CHO-K1 cells after exposure to 20 MeV protons applied either randomly or focused using different grid-like pattern (with pattern width of 5.4  $\mu\text{m}$ , 7.6  $\mu\text{m}$  and 10.8  $\mu\text{m}$ ). A mean dose of 1.7 Gy was used for all irradiation modalities. Data points represent mean values from two independently performed experiments. Significance: \*\*\* $p \leq 0.001$

### 3.4.2.2. Lithium ion irradiation

The cell survival data obtained after irradiation with lithium ions applied either randomly or focused to microbeam spots using four different grid patterns resulting in a mean dose of 1.7 Gy are shown in Figure 3.17. The mean values were calculated from two beam times, each with at least eight replicates, except for the widest grid, which has been measured only in one beam time with five replicates. The cell survival measured for the randomly distributed lithium irradiation was 19 %. An additional narrow grid pattern (3.82 x 3.82)  $\mu\text{m}^2$  grid was used for cell irradiation with lithium ions, with two lithium ions applied per point. Focusing of two lithium ions in the (3.82 x 3.82)  $\mu\text{m}^2$  grid resulted in a significantly decreased cell survival with 11 % ( $p$ -value  $\leq 0.0001$ ) as compared to the random lithium ion irradiation. A significant decrease in cell survival of 9 % ( $p$ -value  $\leq 0.0001$ ) was also shown for the (5.4 x 5.4)  $\mu\text{m}^2$  grid with four lithium ions per point. Using the (7.6 x 7.6)  $\mu\text{m}^2$  grid with 8 lithium ions per spot, the cell survival was 12 % ( $p$ -value  $\leq 0.0001$ ). The exposure of cells to 16 lithium ions per point in the (10.8 x 10.8)  $\mu\text{m}^2$  grid

resulted in an increased cell survival of 28 % as compared to narrow grids and to random lithium irradiation.

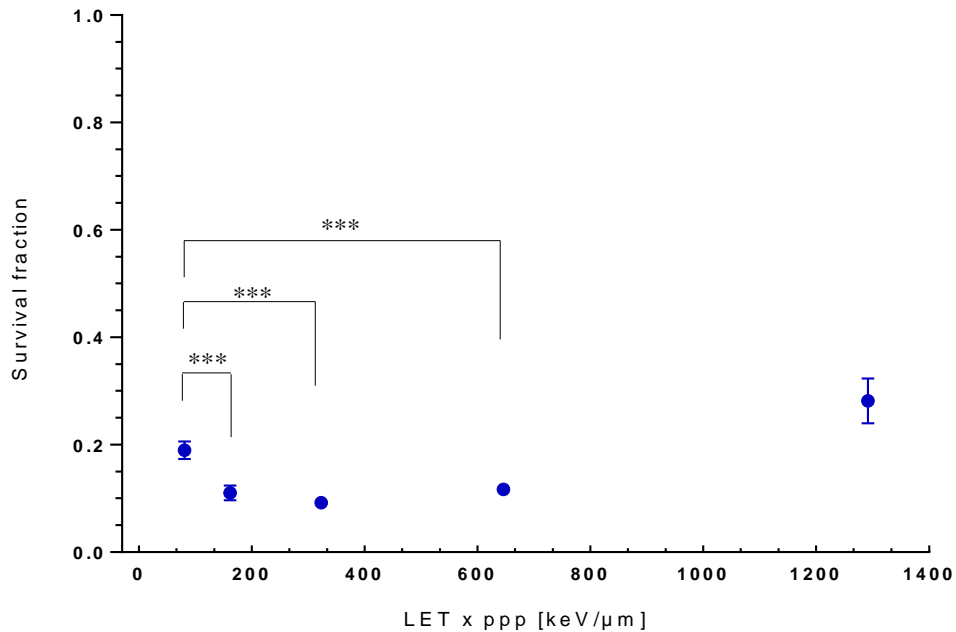


**Figure 3.17:** Cell survival of CHO-K1 cells after exposure to 33 MeV lithium ions applied either randomly or focused using different grid-like pattern (with pattern width of 3.8  $\mu\text{m}$ , 5.4  $\mu\text{m}$ , 7.6  $\mu\text{m}$  and 10.8  $\mu\text{m}$ ). A mean dose of approximately 1.7 Gy was used for all irradiation modalities. Data points represent mean values from two independently performed experiments except for the (10.8 x 10.8)  $\mu\text{m}^2$  grid. Significance: \*\*\* $p \leq 0.001$

### 3.4.2.3. Carbon ion irradiation

As in the case of proton and lithium irradiation the mean values for cell survival after carbon ion irradiation were calculated from two experiments, which were performed in different beam times. The cell survival measured in CHO-K1 cells after carbon ion irradiation is shown in Figure 3.18. 11 % of the cells survived the exposure to a mean dose of 1.7 Gy after focusing one carbon ion to spots of the (5.4 x 5.4)  $\mu\text{m}^2$  grid. For the cell irradiation using spot application with two carbon ions focused to spots of the (7.6 x 7.6)  $\mu\text{m}^2$  grid the evaluated cell survival increased significantly to 17 % ( $p$ -value  $\leq 0.0001$ ). The cell survival rate for the widest grid with four carbon ions per spot increased further to 39 % ( $p$ -value  $\leq 0.0001$ ).

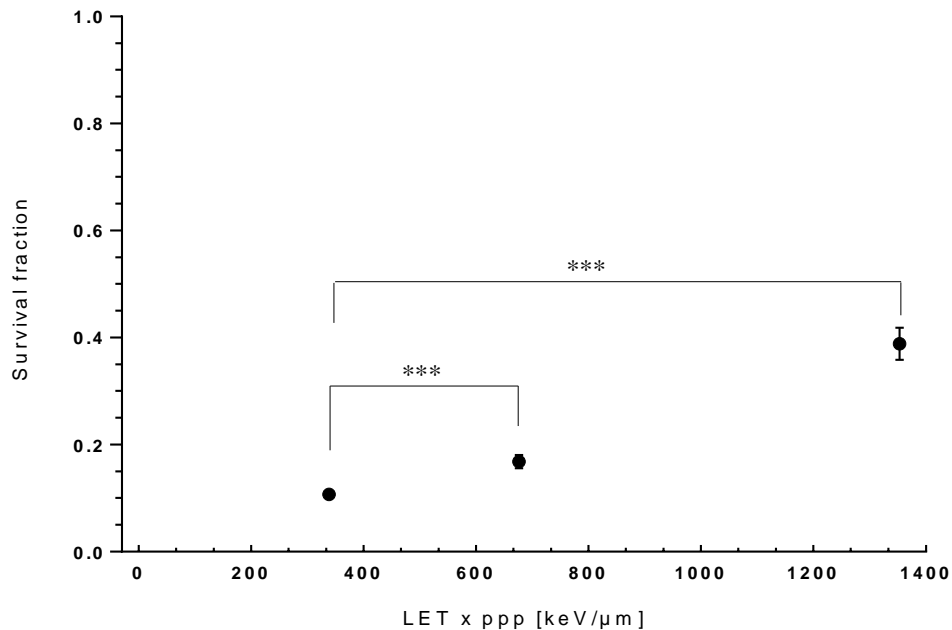


**Figure 3.18:** Cell survival of CHO-K1 cells after exposure to 55 MeV carbon ions applied focused using different grid-like pattern (with pattern width of 5.4  $\mu\text{m}$ , 7.6  $\mu\text{m}$  and 10.7  $\mu\text{m}$ ). A mean dose of approximately 1.7 Gy was used for all irradiation modalities. Data points represent mean values from two independently performed experiments. Significance: \*\*\* $p \leq 0.001$

#### 3.4.2.4. Determination of the RBE for cell survival

The cell survival data from the irradiation with protons, lithium ions and carbon ions obtained from different beam times were averaged in order to calculate the RBE. The pooling of the survival data from different beam times was justified, since all culture and irradiation conditions were comparable in the independent experiments. The cell survival data from the reference radiation with 200 kV X-rays were fitted with a linear-quadratic model and the evaluated linear quadratic coefficients as shown in Table 3.2 were used in order to calculate the equivalent dose of the reference radiation, which is needed to induce the same level of cell killing as the radiation dose of 1.7 Gy from the particle irradiation. The resulting equivalent doses of X-ray irradiation and the calculated RBE values for cell survival after particle irradiation are summarized in Table 3.4.

**Table 3.4:** Calculated cell survival, equivalent dose of the reference radiation and RBE values for the microbeam particle radiation at SNAKE.

Ion species	Grid pattern( $\mu\text{m}^2$ )	Dose (Gy)	Survival	Equivalent dose, $D_{\text{reference}}$	RBE
<b>20 MeV protons</b> LET = (2.66 ± 0.13) keV/ $\mu\text{m}$	random	1.70 ± 0.09	0.75 ± 0.09	1.52 ± 0.53	0.90 ± 0.32
	5.4 x 5.4	1.71 ± 0.09	0.39 ± 0.04	3.86 ± 0.42	2.27 ± 0.29
	7.6 x 7.6	1.71 ± 0.09	0.41 ± 0.05	3.71 ± 0.42	2.18 ± 0.29
	10.8 x 10.8	1.71 ± 0.09	0.42 ± 0.05	3.58 ± 0.42	2.11 ± 0.29
<b>33 MeV Li ions</b> LET = (81±8) keV/ $\mu\text{m}$	random	1.70 ± 0.17	0.19 ± 0.02	5.72 ± 0.31	3.37 ± 0.25
	3.82 x 3.82	1.77 ± 0.18	0.11 ± 0.01	6.92 ± 0.32	4.07 ± 0.28
	5.4 x 5.4	1.77 ± 0.18	0.09 ± 0.01	7.29 ± 0.26	4.29 ± 0.27
	7.6 x 7.6	1.77 ± 0.18	0.12 ± 0.01	6.80 ± 0.28	3.99 ± 0.26
<b>55 MeV C ions</b> LET = (338±34) keV/ $\mu\text{m}$	10.8 x 10.8	1.77 ± 0.18	0.28 ± 0.04	4.74 ± 0.47	2.79 ± 0.31
	5.4 x 5.4	1.86 ± 0.19	0.11 ± 0.01	6.98 ± 0.28	4.11 ± 0.49
	7.6 x 7.6	1.90 ± 0.19	0.17 ± 0.01	6.00 ± 0.28	3.53 ± 0.43
	10.7 x 10.7	1.91 ± 0.19	0.39 ± 0.03	3.84 ± 0.37	2.26 ± 0.33

Figure 3.19 represents the RBE for cell survival after random or focused particle irradiation at SNAKE. The RBE values for 20 MeV protons, 33 MeV lithium ions and 55 MeV carbon ions were evaluated according to the Eq. 1.5 as the ratio between the equivalent dose of the reference radiation with X-rays ( $D_{\text{reference}}$ ) and the dose of 1.7 Gy from the irradiation with charged particles ( $D_{\text{test}}$ ).

The RBE for random proton irradiation was  $0.90 \pm 0.32$  and it increased significantly to  $2.27 \pm 0.29$  ( $p$ -value  $\leq 0.0001$ ) after focusing 117 protons to spots of the (5.4 x 5.4)  $\mu\text{m}^2$  grid. For wider grids, (7.6 x 7.6)  $\mu\text{m}^2$  and (10.8 x 10.8)  $\mu\text{m}^2$ , the RBE was significantly increased to  $2.18 \pm 0.29$  and  $2.11 \pm 0.29$  ( $p$ -value  $\leq 0.0001$ ), respectively.

For the cell irradiation with randomly applied lithium ions a RBE of  $3.37 \pm 0.25$  was calculated. For focused lithium irradiation in narrow grids (3.82 x 3.82)  $\mu\text{m}^2$  and (5.4 x 5.4)  $\mu\text{m}^2$  the RBE increased significantly to  $4.07 \pm 0.28$  and  $4.29 \pm 0.27$  ( $p$ -value  $\leq 0.0001$ ), respectively. However, the RBE value calculated for wider grids (7.6 x 7.6)  $\mu\text{m}^2$  and (10.8 x 10.8)  $\mu\text{m}^2$  decreased to  $3.99 \pm 0.26$  and  $2.8 \pm 0.3$ , respectively.

The irradiation of cells with one carbon ion focused to spots of the  $(5.4 \times 5.4) \mu\text{m}^2$  grid resulted in a RBE of  $4.11 \pm 0.49$ , whereas focusing of two and four carbon ions led to a decreased RBE of  $3.53 \pm 0.43$  and  $2.26 \pm 0.33$ , respectively.

The calculated RBE value for the irradiation with carbon ions focused to spots of the  $(5.4 \times 5.4) \mu\text{m}^2$  grid was significantly higher as compared to focused proton irradiation ( $p$ -value  $\leq 0.0001$ ) using the same radiation dose and the same grid pattern. However, the RBE for focused carbon ion irradiation did not differ significantly from the RBE calculated from the focused lithium irradiation ( $p$ -value  $\leq 0.3411$ ).

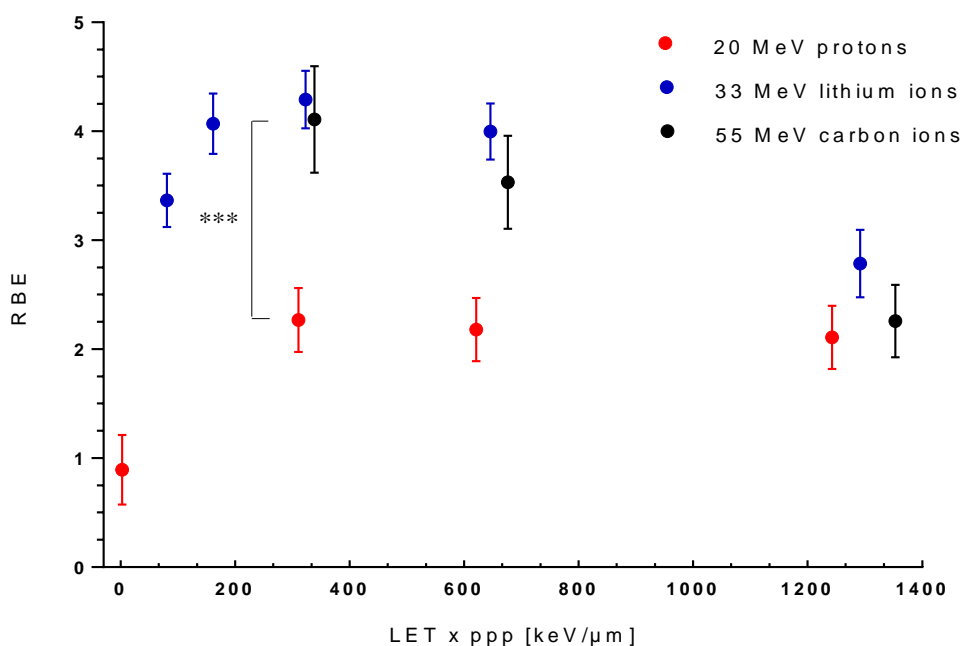


**Figure 3.19:** RBE values for cell survival after exposure to randomly and focused applied protons (red data points) and lithium ions (blue dots) in comparison to focused carbon ion radiation (black dots). Significance: \*\*\* $p \leq 0.001$

### 3.4.2.5. LEM prediction in comparison to experimental data

The experimental cell survival data were accompanied with predictions obtained using the LEM model in order to gain a better theoretic understanding of the importance of the relevant spatial scales of DNA damage for the cell survival. The LEM calculations were performed by our collaborators Dr. Michael Scholz and Dr. Thomas Friedrich from the Department of Biophysics at



GSI Helmholtz Center for Heavy Ion Research in Darmstadt. The LEM model is used as a therapy planning prediction model to calculate the required equivalent doses when using heavy ions for therapy treatment, e.g. radiotherapy with carbon ions.

The modelling calculations using the LEM were performed in a predictive way, independently from the experimental performance and the outcome. For the quantification of the DNA damage complexity different spatial scales of the DNA damage (nm and  $\mu\text{m}$ ) were implemented in LEM as described in detail in Section 1.5. These scales are hypothesized to be relevant for the cell survival after irradiation. The calculations for the local effect probability have been based on the reference data obtained from the X-ray irradiation. As input information the LEM used the coefficients ( $\alpha$  and  $\beta$ ) obtained from the dose response curve with X-rays and the experimental restrictions such as type of the particle, energy, LET, spot beam sizes. The adaptation of the LEM model to the experimental conditions of this work was carried out by an implementation of the 2D Gaussian beam spots of a specified number of ions delivered to the cell nuclei. The geometric parameters as evaluated from the nuclear size distribution as shown in Figure 3.1 were considered in the LEM calculations in order to calculate the overall cell survival.

Figure 3.20 represents the modelling results along with the experimental cell survival data. A good agreement can be observed between the experimental cell survival data and predictive simulation data (Friedrich *et al.*, Submitted).

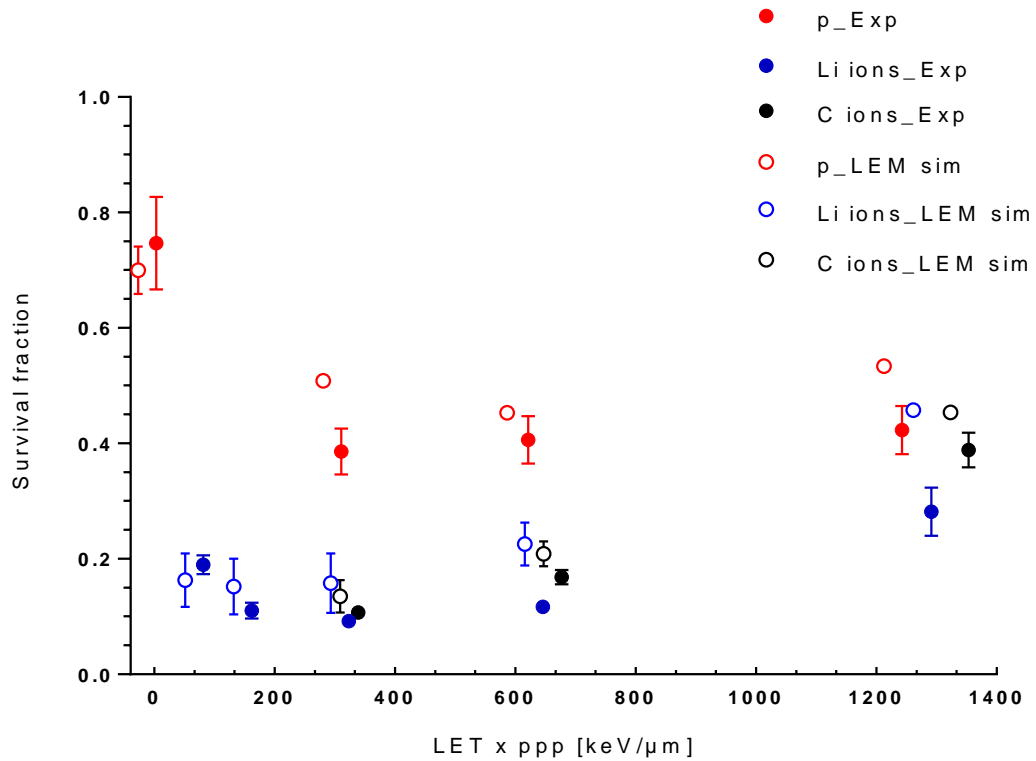


**Figure 3.20:** Cell survival versus the product of the LET and particles per point obtained from experimental measurements (closed symbols) and LEM model simulations (open symbols) in comparison for protons (red), lithium ions (blue) and carbon ions (black). For better visibility, the LEM prediction data points are shifted about 30 keV/μm to the left.

## 4. Discussion

### 4.1. Increased RBE for cell survival after focused particle irradiation

A better knowledge of the biological effects of charged particles would be a great advantage for the future clinical use of particle beams in tumor radiotherapy. High LET radiation, such as carbon ions has several advantages compared to conventional radiotherapy with X-rays. This includes an increased RBE at the end of the particle range and a beneficial depth dose distribution to a normal tissue and tumor. The main physical difference between low LET and high LET radiation is related to their dose deposition in space and time. In order to gain a better understanding of the enhanced RBE of high LET radiation in earlier studies the impact of the temporal dose deposition on the RBE has been investigated (Schmid *et al.*, 2011b; Schmid *et al.*, 2010; Schmid *et al.*, 2009). Here, the effects on the RBE for different biological end points were studied after application of low LET protons, which were focused in time to one nanosecond. It was shown that the time course alone has no influence on the RBE of several biological end points, e.g. the induction of micronuclei in HeLa cells (Schmid *et al.*, 2009) and human keratinocytes from a 3D skin model (Schmid *et al.*, 2010). Also, no change in RBE for the induction of chromosome aberrations in human-hamster hybrid cells (Schmid *et al.*, 2011b) and for the most relevant radiobiological end point of cell survival using HeLa cells (Auer *et al.*, 2011) could be shown. The authors have concluded that the time course of dose deposition has seemingly no influence on the RBE (Schmid *et al.*, 2012a).

Recently, using ion microbeam particle irradiation at SNAKE, protons were applied to cells randomly or focused to sub-micrometer spots and the influence of spatial dose distribution on RBE with respect to induction of dicentric chromosomes and micronuclei was investigated (Schmid *et al.*, 2015; Schmid *et al.*, 2012a). In these studies, the authors have found enhanced radiation effectiveness for the induction of chromosome aberrations by focusing of protons and lithium ions.

In the present work, we concentrated on the influence of the spatial dose distribution on the RBE with respect to cell survival, since this is a more representative radiobiological *in vitro* end point. The end point of cell survival reflects the full dimension of radiation effects to the cells, depending on whether the irradiated cell will fail to repair the DNA damage and die or the cell

will retain its reproductive integrity and therefore will survive the radiation. Thus, the maintenance of the reproductive integrity is a crucial characteristic of the surviving cells which enables cell proliferation and the formation of colonies.

The RBE for cell survival from spot-like dose distribution obtained after focused proton irradiation was compared with that from homogeneously distributed protons. In addition, the effects of focused protons were compared with high LET radiation effects using lithium and carbon ions. The cell survival data demonstrated that simply by focusing 117 protons to sub-micrometer spots the RBE for cell survival (Figure 3.19) was significantly increased as compared to homogeneous proton irradiation. Notably, the evaluated RBE for homogeneous proton irradiation ( $0.90 \pm 0.32$ ) was consistent with the generally assumed RBE of 1.1, which is implemented in proton therapy (Paganetti, 2002; Paganetti, 2003). By focusing high LET 33 MeV lithium ions to spots of narrow grids ( $3.8 \times 3.8$  and  $5.4 \times 5.4$ ) the same effect enhancement could be achieved as compared to the random lithium irradiation. This result demonstrated that changing of dose deposition patterns strongly influence the resulting effect. Focused dose deposition within the cell nuclei is supposed to induce multiple DNA DSBs in close proximity, resulting in the formation of complex DSBs at the irradiated spots. Such complex DSBs are well-known as more severe DNA lesions which are more difficult to repair than isolated, well separated DSBs (Goodhead, 1994; Goto, 2002; Hill *et al.*, 2011; Lomax, 2013; Ward, 1994). Furthermore, interaction of adjacent DSBs in close spatial proximity enhances the probability of connecting the wrong ends. Although the total number of induced DSBs is supposed not to be altered by redistribution of dose deposition, the inaccurate DNA repair is meant to result in more chromosome aberrations and thus less cell survival after focused irradiation. A higher frequency of chromosome aberrations and micronuclei after focused dose deposition has been experimentally shown in a previous study using the same experimental approach (Schmid *et al.*, 2012a). The cell survival data from the present work align very well with the data obtained there.

However, the calculated RBE for focused proton irradiation ( $2.27 \pm 0.29$ ) was significantly lower than that of high LET 55 MeV carbon ions ( $4.11 \pm 0.49$ ) or 33 MeV lithium ions ( $4.29 \pm 0.27$ ) using the same grid pattern and same mean dose of 1.7 Gy. This additional enhancement of the resulting effect can be attributed to the extremely high local doses that come from the inner core of the lithium and carbon ion tracks. Focusing even more than one carbon ion to spots resulted in an increased cell survival and thus a decreased RBE (cf. Figure 3.19). An explanation for this

finding could be that by focusing more than one carbon ion to spots and thus applying a higher local dose, there may be a saturation of the damage. The local dose applied from one carbon ion seemed to be sufficient to induce the maximal cell killing. Therefore, the application of more dose locally by focusing more carbon ions per spot was not expected to further enhance the effectiveness with respect to cell killing.

#### **4.1.1. Influence of the nuclear size distribution on the cell survival**

The determination of the nuclear area and of the probability for hitting a cell nucleus using different irradiation grid patterns is of special importance, since the microbeam irradiation of cells at SNAKE has been performed sequentially using a regular pattern. The results have shown that CHO-K1 cells possess a relatively small cell nucleus compared to other cell lines such as HeLa cells. The mean nuclear area of CHO-K1 cells determined in this work was  $(67.6 \pm 2.2)$   $\mu\text{m}^2$  and this result differs from the results obtained from other studies (Konishi, 2005; Weyrather *et al.*, 1999). For the same cell line, Weyrather *et al.* measured an average nuclear area of  $(87.8 \pm 11.1)$   $\mu\text{m}^2$  (Weyrather *et al.*, 1999), whereas Konishi *et al.* evaluated a cell nucleus area of  $(127 \pm 1.2)$   $\mu\text{m}^2$  (Konishi, 2005). One reason for this discrepancy could be attributed to different cell cultivation methods used in these experiments. In this work CHO-K1 cells were seeded in a 4 mm diameter area on Mylar foil 4 hours prior to irradiation experiment. Using this cell cultivation setup (see Figure 2.2) in our experiments the cells reached 100 % confluency prior to irradiation on a very small cell growth area and it seemed that this high cell density might have an effect the size of the cell nucleus.

By knowing the nuclear area of CHO-K1 cells, the probability for unhit cells could be determined for each grid pattern. The probability for unhit cells increased with increasing distance between the spots within a grid. As a result, the highest probability for unhit cells was found for the two widest grids  $(7.6 \times 7.6)$   $\mu\text{m}^2$  and  $(10.8 \times 10.8)$   $\mu\text{m}^2$ , namely 12% and 44%, respectively (see Table 3.1). If a cell nucleus remains unhit, the cell may survive in our experimental setup. This has to be taken into account when interpreting the data. For the widest grid used in the experiments this would mean that cells which are hit will certainly be killed, as the evaluated cell survival is less than 44%, regardless which of the three particles have been used for the irradiation. If hit statistics is considered, the saturation effect resulting from the focused spot

application of carbon ions was not observable after proton irradiation. Focusing of protons using narrow grids enhanced the effect, while for the wider grids cell survival recovered again due to the unhit cell population.

#### **4.1.2. Comparison of experimental cell survival data with LEM predictions**

While for proton radiotherapy, a generic RBE value of 1.1 is employed (Friedland *et al.*, 2017; Paganetti, 2002; Paganetti, 2003), for the use of heavy ions the variations of the RBE along the ion beam penetration in tissue have to be considered and the biological effects need to be simulated. Therefore, an accurate understanding of RBE effects is essential for the optimal application of heavy ions for radiotherapy. The biological modelling approach LEM that has been implemented in treatment planning systems for cancer particle therapy with heavy ions was developed at GSI (Scholz, 1997). This model allows for the prediction of the biological effects of ion beams. Over the last years it has been further developed and extensively tested by comparison with experimental *in-vitro* and *in-vivo* data. The latest version of the LEM model (LEM IV) is based on the assumption that the initial spatial DNA damage distribution represents the determining factor for the final cellular biological response after radiation (Elsässer, 2010; Friedrich *et al.*, 2012).

In this study we compared the experimental cell survival data with LEM predictions performed at GSI by Thomas Friedrich in order to analyze how precisely LEM can validate the experimental outcome. Furthermore, in our recent study the relevance of different spatial scales on the overall radiation damage was analyzed, both experimentally and theoretically (Friedrich *et al.*, Submitted). Focusing of protons to sub-micrometer spots in cells was used as an experimental approach to study the dependence of the radiation effectiveness with respect to cell survival on different spatial scales. In parallel, LEM calculations were performed based on the assumptions that three spatial scales, namely the size of the DNA (nm scale), the size of multiple chromatin loops ( $\mu\text{m}$  scale) and finally the size of cell nuclei (10  $\mu\text{m}$ ) contribute to the overall radiation DNA damaging (Friedrich *et al.*, Submitted).

Moreover, the comparison of the experimental cell survival data with LEM predictions allowed for a more precise interpretation of the obtained results. The independently performed LEM predictions on cell survival were in good agreement with the obtained experimental data, as

shown in Figure 3.20. A slight difference could be observed in the case of lithium ion irradiation with the widest grid, (10.8 x 10.8)  $\mu\text{m}^2$  grid. This discrepancy could be explained by the fact that the data for this grid irradiation were measured in one lithium beam time and further experiments are needed in order to validate this result.

As discussed above, focusing of protons to sub-micrometer spots in cell nuclei resulted in significantly increased radiation effectiveness as compared to a random irradiation and thus high LET radiation effects could be approximated. A good correlation of the experimental data with theoretical LEM predictions provides evidence that the enhanced effectiveness caused by focused dose deposition could be explained by the interaction of DNA lesions on the micrometer ( $\mu\text{m}$ ) scale within a chromatin loop. This interaction leads to formation of even more complex lesions which cannot be repaired easily. Herewith, the  $\mu\text{m}$  scale which is hypothesized to be relevant for the radiation induced DNA damage could be confirmed.

The cell survival after high LET carbon and lithium ion irradiation using the same radiation dose and the same focusing level was significantly higher as compared to focused proton irradiation. As can be seen from the 2D simulations of the microscopic dose deposition from focused proton and carbon ion beam spots (cf. Figure 1.1 and Figure 1.2), the outer region of the beam spots is similar. However, the inner region of the carbon beam spot provides much higher local doses than in the case of a focused proton beam spot. Consequently, this extremely high local dose in the core of high LET particle track results in the interaction of SSBs on the nanometer (nm) scale, leading to the formation of additional DSBs, and thus to an enhanced DSB yield. With this observation, the interaction of DNA lesions on the nm scale could be verified.

The dependence of the 10  $\mu\text{m}$  scale on the cell survival was tested using the widest grid, (10.8 x 10.8)  $\mu\text{m}^2$  where the probability for a cell to remain unhit was high (44%). Here, it has been experimentally proven that only those cells, which are not hit, will survive. Thus, the 10  $\mu\text{m}$  spatial scale was given by the size of the cell nucleus, reflecting a damping of the effects due to the hit probability (Friedrich *et al.*, Submitted).

Experimental cell survival data from this work strongly support the assumption of LEM that the spatial dose distribution is the determining factor of the RBE. Moreover, these data have confirmed the existence of three spatial scales, namely nm- $\mu\text{m}$ - and 10  $\mu\text{m}$  scale, as well as their contribution to the high LET radiation induced DNA damage and the consequent cell killing.

Finally, the accuracy of LEM predictions based on mechanisms associated with these three spatial scales could be verified.

#### **4.2. DNA DSB repair after low LET proton irradiation and high LET carbon ion irradiation**

The influence of the spatial dose distribution on the induction of DNA DSBs and their repair has also been studied in this work. In general, DSBs are the most serious DNA lesions induced by ionizing radiation to cells, which can result in the formation of chromosome aberrations, induction of cell death or carcinogenesis (Wyman, 2006). A widely used method for measuring DSB repair is detection of  $\gamma$ -H2AX (the phosphorylated form of histone H2AX) foci by immunofluorescence. The number of  $\gamma$ -H2AX foci correlates with the induced DSBs and the disappearance of  $\gamma$ -H2AX foci is related to the DSB repair at low radiation doses (Rothkamm, 2003), if not more than 100-150 DSBs are induced in the cell nucleus (Bouquet *et al.*, 2006).

The DSB formation and processing after exposure of cells to either focused or random proton irradiation was analyzed in this work based on the use of the  $\gamma$ -H2AX assay and flow cytometric measurement. A microscopy analysis of  $\gamma$ -H2AX foci, which was performed in parallel to the  $\gamma$ -H2AX flow cytometry experiments, allowed for the qualitative validation of the DNA DSB distribution pattern after random and focused proton irradiation with a mean dose of 1.7 Gy. A quantitative analysis by counting individual  $\gamma$ -H2AX foci was not possible due to a high local density of DNA DSBs obtained after focused proton irradiation and the lack of markers sensitive enough for such a task (Figure 3.9 b-d).

A higher residual  $\gamma$ -H2AX fluorescence intensity (FI) was measured after the focused proton irradiation as compared to the homogeneous proton irradiation (Figure 3.5), particularly at later time point (12 hours), as the residual  $\gamma$ -H2AX FI was 28% higher than in the case of a homogeneous dose application. This result indicated that a focused dose deposition might induce more complex DSBs, which are difficult for cells to repair. These findings could be confirmed by a qualitative visualization of  $\gamma$ -H2AX foci distribution 30 minutes post-irradiation, as focused spots of protons resulted in the induction of an increased local density of DSBs at the irradiation spots (Figure 3.3). Applying more protons to spots, it becomes gradually more difficult to distinguish between the individual  $\gamma$ -H2AX foci, since multiple DSBs were encompassed within



the nuclear domains. These highly localized and dense damage clusters induced by focused protons are comparable to the DNA damage induced after radiation with high LET particles as reported by others (Costes, 2006; Reindl *et al.*, 2015; Reindl *et al.*, 2017), where almost no individual foci could be observed along the track of a high LET particle. Such complex DNA damage, which consists of several DNA lesions in close proximity are considerably more difficult to repair than spatially isolated lesions (Goto, 2002; Hada, 2008; Lomax, 2013; Ward, 1985). Moreover, our results are consistent with the simulation results of Kreipl *et al* (Kreipl, 2009). In this theoretical study the authors investigated the influence of spatial and temporal proximity of ion particle tracks on the yield of clustered lesions using Monte-Carlo based modelling approach. Their simulation results indicated that a higher yield of clustered lesions could be induced by 20 MeV protons when applied within small spatial proximity.

In order to compare the DNA DSB repair after focused low LET proton irradiation with that of high LET carbon ions, the flow cytometric analysis of the residual  $\gamma$ -H2AX FI was performed also with high LET carbon ions. The  $\gamma$ -H2AX FI was evaluated for the same time points as for proton irradiation, together with other time points to characterize in more detail the  $\gamma$ -H2AX repair kinetics after high LET radiation. As a result, the relative  $\gamma$ -H2AX FI measured 6 and 12 hours after irradiation with carbon ions (Figure 3.6) was 19-times and 24-times higher than after focused proton irradiation. This result suggested that after carbon ion irradiation, a much higher fraction of DSBs remains unrepaired as compared to proton irradiation, probably due to a higher proportion of complex DSBs. Leatherbarrow and Harper investigated the induction and rejoining of DSBs in Chinese hamster V79-4 cells after irradiation with high LET  $\alpha$ -particles and low LET  $\gamma$ -rays.. Their results have shown slower repair kinetics of  $\gamma$ -H2AX loss after irradiation with  $\alpha$ -particles as compared to the irradiation using the same dose of  $\gamma$ -rays, indicating that high local doses from the  $\alpha$ -tracks induce more complex DNA damage (Leatherbarrow, 2006). In general, the observed differences in the repair of the DNA damage from different radiation qualities can be attributed to the complexity of the DNA damage (Jenner, 1993).

On the basis of several studies it could be shown that a much higher frequency of clustered DSBs can be induced by high LET radiation than in the case of low LET radiation (Schipler, 2013). More precisely, high LET radiation accounts for about 90 % of clustered DNA damage in comparison to low LET radiation, after which only about 30% of clustered DNA DSBs are induced (Eccles, 2011; Lomax, 2013; Nikjoo, 1999). Goodhead proposed that the observed

increase of RBE for cell killing with increasing LET is due to the formation of complexes of clustered DNA damage, which more likely arise from a densely ionizing particle of higher LET (Goodhead, 1994). In the present study we could show that simply by focusing protons to sub-micrometer spots in cell nuclei, an increased RBE for cell killing could be achieved as shown in Figure 3.19. Therefore, this observed effect enhancement in cell killing can be explained as a result of an increased DNA damage complexity and thus diminished DNA damage repair capacity of the irradiated cells caused by a focused dose deposition.

Most of the DSBs are repaired by NHEJ pathway (Ma, 2005), a very fast but also an error-prone repair process (Khanna, 2001), which occurs mainly in the G1 phase of the cell cycle, since it does not require sequence homology. In contrast, the HR repair represents a more complex and slower process, employed mainly in S and G2 phase of the cell cycle (Shibata, 2011; Wyman, 2006). The DNA damage complexity is one of the determining factors which has an influence on the DNA repair pathway choice (Shibata, 2011). It is well known that complex DSBs induced by high LET radiation during the late S and G2 phase of the cell cycle are repaired mostly by HR, ensuring most accurate repair (Schmid *et al.*, 2012b). As DSB repair can be processed through two repair pathways, the disappearance of  $\gamma$ -H2AX fluorescence over time can be described by a bi-exponential function with one fast and one slow component. Description of the  $\gamma$ -H2AX reduction over time by a bi-exponential function has been implemented successfully by Schmid *et al.* in their study with the aim to investigate the kinetics of  $\gamma$ -H2AX fluorescence reduction in HeLa cells after exposure to low LET X-rays and high LET 55 MeV carbon ions (Schmid, 2010). In the present work the same evaluation method was used in order to describe the DSB repair kinetics in CHO-K1 cells after high LET radiation using carbon ions. The examined decay time  $\tau_2 = (3 \pm 51) 10^6$  h represents the decay rate of the slow repair after carbon ion irradiation and it seemed to be very high and inaccurate. This result would mean that about 45% of the  $\gamma$ -H2AX signal is still detectable 24 hours after irradiation with two carbon ions per spot focused in the  $(5.4 \times 5.4) \mu\text{m}^2$  grid, and it represents the fraction of the residual unrepaired DSBs. In the study performed by Schmid *et al.* much shorter decay times for slow and fast repair were evaluated after carbon ion irradiation. One possible explanation for the discrepancies could be that the chosen radiation dose in our case (3.4 Gy) was rather excessive, so the repair of the induced DNA DSBs would take even longer. Another reason could be that the radiation dose of 3.4 Gy resulted in irreparable lethal DNA damage so that the induced DSBs remained unrejoined.

The fast proliferating characteristics of CHO-K1 cells are another problematic aspect in this experiment which might have an influence on the experimental outcome. The cells that are less damaged proliferate better and faster than highly damaged cells, which might be arrested in the G2 phase of the cell cycle for a certain period of time. Consequently, this would mean that the fraction of cells with high  $\gamma$ -H2AX FI would decline, thus decreasing the mean  $\gamma$ -H2AX signal. Therefore, it would be conceivable that a cell line with slower proliferating activity might be more appropriate in this experiment.

MacPhil *et al.* reported that the background  $\gamma$ -H2AX level varies as a function of the cell cycle (Macphil *et al.*, 2003). Therefore, it would be necessary to perform a bivariate analysis of  $\gamma$ -H2AX expression relative to the DNA content in order to measure cell cycle-specific expression of  $\gamma$ -H2AX. Furthermore, the analysis have to be restricted only to G1 cells in order to minimize the bias introduced by spontaneous foci measured in S and G2 phase cells, since the expression of  $\gamma$ -H2AX in unirradiated cells is associated with DNA replication (Macphil *et al.*, 2003).

The preliminary data obtained so far suggest that focusing of protons to spots in cell nuclei might induce more complex DNA damage, resulting in slower DSB repair kinetics, thus approximating high LET radiation damaging.

### **4.3. Induction of apoptosis in cells using microbeam particle irradiation**

The main goal of radiotherapy cancer treatment is to inhibit the proliferation of tumor cells. This can be achieved by inducing cell death in tumor cells (Eriksson, 2010). It is well known that ionizing radiation used for cancer treatment results in DNA damage and that the severity of the DNA damage is the determining factor whether the cells will fail to repair the DNA damage. Failure of the cell to repair the DNA damage can lead to mutations and chromosome aberrations or cell death. In order to prevent the accumulation of damaged and mutated cells, programmed cell death pathway can be activated, namely apoptosis (Borges, 2008; Matt, 2016). Thus, apoptosis activation following radiation-induced DNA damage represents a protective cellular strategy to prevent carcinogenesis (Roos, 2013).

In the present work, apoptosis induction in CHO-K1 cells was analyzed after irradiation with focused or randomly applied protons and carbon ions in order to investigate whether change in

spatial dose distribution affects apoptotic response. This is the first study that investigates the effect of different spatial dose distribution on apoptosis induction in cells.

Flow cytometric analysis of caspase 3/7 activity together with SYTOX staining allows to differentiate between apoptotic (only caspase 3/7 positive cells), necrotic (only SYTOX positive cells) and double positive cells (caspase 3/7 positive and SYTOX positive cells). The double positive cells in this analysis are supposed to be secondary necrotic cells (Berghe, 2010; Denecker *et al.*, 2001; Krysko, 2008; Silva, 2010). Secondary necrotic cells are characterized by active caspases as a marker of apoptosis and disintegrated plasma membrane, which is a characteristic feature of necrotic cells. The process of secondary necrosis has been well described by several studies which indicate that in the absence of phagocytosis, apoptotic cells proceed to secondary necrosis, a stage which possesses many characteristics of primary necrosis (Krysko, 2008). The occurrence of secondary necrotic cells is often regarded as an *in vitro* artifact, because of the absence of phagocytic capacity (Berghe, 2010). Therefore, we assume that secondary necrotic cells (double positive cells) are actually late apoptotic cells, which are not cleared by phagocytosis.

In a preliminary experiment with 200 kV X-rays the induction of apoptosis at two time points, 24 and 48 hours after irradiation was analyzed. The obtained results indicated that the unirradiated cells show a higher percentage of double positive cells 48 hours after irradiation compared to the unirradiated cells measured 24 hours after irradiation. One possible reason for the high apoptotic rate in unirradiated cells could be the high cell density observed 48 hours after starting the experiment. The observation that high cell density alone can trigger apoptotic response in unirradiated cells was also reported by others, e.g. in CHO cells (Fiore, 1999), in primary rat hepatocytes (Maeda, 1993) and human myeloblastic HL-60 cells (Saeki, 1997). Consequently, 24 hours seemed to be a more appropriate time point for analyzing apoptotic response in CHO-K1 cells using the cell cultivation setup as shown in Figure 2.2. Trypsinization of cells after irradiation and reseeding in a new culture dish was not an option, because the cells were already trypsinized once prior to irradiation. Detaching cells from the Mylar foil by trypsinization for the second time on the same day might evoke additional cellular stress and contribute to a non-radiation specific apoptotic or necrotic response.

The flow cytometric measurements of caspase 3/7 activity after irradiation with a mean dose of 3.4 Gy using particles with different LET demonstrated that apoptosis in CHO-K1 cells seems to be induced in a LET-dependent manner. After high LET carbon ion irradiation more apoptotic cells could be observed than after proton and X-ray irradiation (Figure 3.14). There are several studies that have reported on a higher efficiency of high-LET radiation to induce apoptosis (Iwadate *et al.*, 2001; Meijer *et al.*, 1998; Takahashi *et al.*, 2004; Tsuchida, 1998). Iwadate *et al.* investigated induction of apoptosis after irradiation with high LET carbon ions and low LET X-ray irradiation in glioma cancer cell lines with wild-type *p53* and mutated *p53*, respectively (Iwadate *et al.*, 2001). Their results provided evidence that carbon ion irradiation can induce apoptosis in glioma cells more efficiently than X-rays regardless of *p53* gene status. Therefore, radiotherapy using high LET particles, e.g. carbon ions is supposed to be a promising radiotherapy approach to target cancer cells harboring mutated *p53* gene. For CHO-K1 cells used in this work, it is known that the *p53* sequence carries a single missense mutation in codon 211 (Hu, 1999; Tzang, 1999). However, it has been shown that this mutation has no effect on the functional properties of the p53 protein (Tzang, 1999).

Furthermore, our data suggested that protons applied randomly and X-rays may induce a similar apoptotic response in cells after irradiation with 3.4 Gy. This result was expected, because low LET protons are very similar to X-rays with respect to their radiation effectiveness. Furthermore, these results are in good accordance with the obtained cell survival data.

After focusing protons to spots in cell nuclei, the percentage of caspase 3/7 positive cells remained unchanged. However, a higher percentage of late apoptotic cells and thus more apoptotic cells in total could be observed after a focused dose application (Figure 3.17). This finding can be interpreted as an indication that focused proton irradiation might trigger apoptotic response in cells more rapidly than random proton irradiation, as the fraction of late apoptotic cells was much higher. A more rapid induction of apoptosis after focused proton irradiation could be interpreted as a consequence of clustered DNA damage, which is supposed to be higher than in the case of a random proton irradiation. The apoptosis results are consistent with the cell survival and DSB repair results from this work, as significantly higher cell killing and more unrepaired DSBs could be measured after focused proton irradiation. Using wider grids for microbeam irradiation at SNAKE, the hit statistics become important and this has to be considered for the interpretation of the results. The irradiation with the narrow (5.4 x 5.4)  $\mu\text{m}^2$

grid resulted in almost no unhit cell nuclei, while using wider grids the probability for unhit cells increased to 12 % and 44 %. This high percentage of unhit cells could be the reason for the decreased apoptotic rate in cells after irradiation using the widest grid (10.8 x 10.8)  $\mu\text{m}^2$ .

Rapid apoptotic response became even more pronounced after high LET radiation with carbon ions, as the percentage of early apoptotic cells decreased and the fraction of late apoptotic cells increased as compared to the focused proton irradiation (Figure 3.14). Therefore, high LET carbon ion irradiation is supposed to promote apoptosis induction efficiently and even more rapidly than low LET protons and X-rays. This result is in a good agreement with our cell survival and DSB repair results, since a significantly higher cell killing and a higher fraction of unrepaired DNA DSBs after carbon ion irradiation could be shown as compared to low LET radiation with protons or X-rays. Meijer *et al.* could also show a faster apoptotic response in human peripheral lymphocytes after high LET radiation (Meijer *et al.*, 1998). This leads to the conclusion, that analysis of apoptotic response for different radiation qualities at only one time point may not represent the realistic outcome. The fact that apoptosis is a time-dependent process was reported also by Holgersson *et al.* (Holgersson *et al.*, 2003). In this study the authors observed different apoptotic response after exposure of human glioma cells to low LET  $\gamma$ -rays and high LET nitrogen ions. Irradiation of cells with 4 Gy of nitrogen ions resulted in a more rapid induction of apoptosis as compared to irradiation with low LET  $\gamma$ -rays using the same radiation dose (Holgersson *et al.*, 2003).

Furthermore, the results from this work suggested that radiation induces apoptosis is a dose-dependent manner as could be shown for irradiation with X-rays. By increasing the radiation dose from 3.4 Gy to 5.1 Gy, the frequency of apoptotic cells increased (Figure 3.9). Unfortunately, radiation doses higher than 3.4 Gy were technically not feasible in the case of focused proton irradiation due to the technical setup at SNAKE. However, the irradiation with 5.1 Gy of carbon ions resulted in no further increase in apoptotic rate as compared to the radiation dose of 3.4 Gy. This can be explained by the saturation effect which has been observed already for the endpoint of cell survival, as more than one carbon ion was applied per spot and cell survival tended to increase. Therefore, the same saturation effect is expected to be seen also with regard to apoptosis induction.

It has to be mentioned that apoptosis cannot fully account for the cell killing measured by clonogenic cell survival assay. For example, carbon ion irradiation with a mean dose of 1.7 Gy resulted in about 11% of cell survival, while the irradiation with twice the dose (3.4 Gy) resulted in only 13 % apoptotic cells. Some other types of cell death pathways, such as mitotic catastrophe or senescence, which were not analyzed in this work, may well also participate in cell killing.

One important observation was made concerning the unirradiated samples from proton and carbon ion radiation experiments at SNAKE. A remarkably high percentage of secondary necrotic cells was measured in unirradiated cells from both proton and carbon ion irradiations at SNAKE, unlike in unirradiated cells from the experiments with X-rays. A possible reason for this outcome might be the transport of cell samples from the irradiation location in Garching to our department where flow cytometry measurements were carried out. The irradiated cell samples were transported by car and the cell transport did not take longer than half hour and immediately after the transport, cells were placed again into the incubator at 37 °C. These fluctuations of the incubating temperature could be the reason for different percentage of caspase 3/7 positive cells in unirradiated cell samples from the irradiation experiments at SNAKE and at the X-ray irradiation facility.

Because of the limited available beam time, we had to prioritize our experiments. Since other biological end points e.g. cell survival and chromosomal aberrations (not part of this work) were much more important for the joint project, we decided collectively not to pursue apoptosis experiments any further. Therefore, the apoptosis analysis here is based on a single data set from one proton beam time and the obtained data suggest that focusing protons to spots in cell nuclei increases apoptosis induction due to an increased DNA damage complexity. As already discussed above, complex DSBs are more severe lesions repaired with less accuracy. Therefore, the severity of DNA damage is a deciding factor in the cell's fate. If DNA is severely damaged by ionizing radiation, the probability that cells will undergo apoptosis is higher.





## 5. Conclusion and Outlook

The clinical use of charged particles for tumor radiotherapy offers many benefits in comparison to conventional photon radiotherapy. All accelerated charged particles show an inverse depth dose profile with the characteristic Bragg Peak, which provides a very precise dose deposition to the tumor. By achieving the same tumor control this leads to reduced damage in the surrounding normal tissue and therefore less acute or late side effects. Additionally, charged particles have a higher RBE in the region of the maximal dose deposition and may offer biological advantages such as enhanced cell killing. In this PhD work one of the most important physical properties of the high LET radiation, namely the inhomogeneous spatial dose distribution was investigated in order to contribute to a better understanding of the increased RBE of high LET particles. This question was examined using a unique experimental approach at the ion microprobe SNAKE whereby sub-micrometer focused protons were applied to cell nuclei in several variations, thus changing the spatial dose and DNA DSB distribution. The effect of the spatial dose distribution on the biological effectiveness was analyzed with regard to different biological end points such as DNA DSB repair, apoptosis induction and the most relevant radiobiological end point of cell survival.

From the data obtained in this work the general conclusion can be drawn, that the spatial focused dose application manifests itself as a significant increase in the RBE with respect to cell survival (Figure 3.19). These results demonstrate evidence that high LET radiation effects can be approached by focusing low LET radiation. In addition, it could be shown that experimental cell survival data are in good agreement with independently performed LEM predictions (Figure 3.20), supporting the theoretical assumptions that spatial dose distribution has a great impact on the RBE. Moreover, the comparison of experimental cell survival data with LEM predictions allows for better understanding of the DNA damage induced by high LET radiation. Finally, it provides a substantial evidence for a coexistence of three spatial scales of DNA damage (nm,  $\mu\text{m}$  and 10  $\mu\text{m}$  scale), which all together contribute to the overall radiation damage.

The preliminary DSB repair data have shown a trend that focusing of protons may result in a higher amount of persistent unrepaired DSBs as evaluated by the mean fluorescence intensity of

$\gamma$ -H2AX. This result indicated that the radiation induced DNA damage after focused proton irradiation might be more complex than in the case of a random proton irradiation. However, further improvement of the method and additional experimental work are needed in order to gain a better insight into the radiation induced DNA damaging and the underlying complexity of DSBs. Although there are several benefits of using flow cytometry for the quantitative analysis of  $\gamma$ -H2AX fluorescence intensity, a similar method might be even more suitable for our irradiation experiments, namely the slide-based laser scanning cytometry (LSC). Using this method, it would be possible to irradiate different regions on a single cell sample, thus ensuring identical conditions for cell cultivation and cell staining for all irradiated fields from the same cell sample. Additionally, a cell line with slower proliferating activity than CHO-K1 cells should be considered, and radiation doses which would be most appropriate for this experiment should be ascertained.

The results relating to radiation induced apoptosis have shown a trend that focused dose application could induce a higher percentage of late apoptotic cells when compared to a random proton irradiation and X-ray irradiation (Figure 3.14). Moreover, our data suggested a more rapid apoptotic response after a focused proton application due to the DSB clustering. Induction of apoptosis in CHO-K1 cells seemed to be LET- dependent. A dose-dependent increase in apoptosis rate could be shown after X-ray irradiation; however this was not the case after high LET radiation with carbon ions.

Further research is however necessary to better understand the increased RBE of high LET radiation and is of great importance for a biological understanding. Since heavy ions show inhomogeneous spatial and temporal dose deposition, a combination of both aspects should be investigated in a future research project. However, the implementation of such irradiation experiments using the ion microbeam SNAKE to apply protons in different time courses, from nanoseconds to hours focused at sub-micrometer spots in cell nuclei represents a very demanding task, from both the physical and the biological side. The same biological end points of cell survival, DSB repair and induction of chromosomal aberrations would be of special interest in order to investigate how the changing of the temporal as well as spatial dose deposition affects the interaction of radiation induced DSBs.

## Bibliography

- ALBERTS, B., JOHNSON, A., LEWIS, J., *Molecular Biology of the Cell*. New York, Garland Science (2002).
- AUER, S., HABLE, V., GREUBEL, C., DREXLER, G. A. *et al.*, *Survival of tumor cells after proton irradiation with ultra-high dose rates*. *Radiation oncology (London, England)* **6** (2011) 139
- BERGHE, T., VANLANGENAKKER, N., PARTHOENS, E., *Necroptosis, necrosis and secondary necrosis converge on similar cellular disintegration features*. *Cell Death and Differentiation* **17** (2010) 922-930
- BETHE, H., *Zur Theorie des Durchgangs schneller Korpuskularstrahlen durch Materie*. *Annalen der Physik* **397** (1930) 325-400
- BORGES, H., LINDEN, R., WANG, J., *DNA damage-induced cell death: lessons from the central nervous system*. *Cell research* **18** (2008) 17-26
- BOUQUET, F., MULLER, C., SALLES, B., *The loss of gamma-H2AX signal is a marker of DNA double strand breaks repair only at low levels of DNA damage*. *Cell Cycle* **5** (2006) 1116-1122
- BRANZEI, D., FOIANI, M., *Regulation of DNA repair throughout the cell cycle*. *Nature reviews. Molecular cell biology* **9** (2008) 297
- BROWN, A., SUIT, H., *The centenary of the discovery of the Bragg peak*. *Radiotherapy and Oncology* **73** (2004) 265-268
- CHANG, H. H. Y., PANNUNZIO, N. R., ADACHI, N., LIEBER, M. R., *Non-homologous DNA end joining and alternative pathways to double-strand break repair*. *Nature Reviews Molecular Cell Biology* (2017)
- CHEUNG, K., *Intensity modulated radiotherapy: advantages, limitations and future developments*. *Biomedical Imaging and Intervention Journal* **2** (2006) 19
- COMBS, S. E., NIKOGHOSYAN, A., JAEKEL, O., KARGER, C. P. *et al.*, *Carbon ion radiotherapy for pediatric patients and young adults treated for tumors of the skull base*. *Cancer* **115** (2009) 1348-1355

- COSTES, S., BOISSIÈRE, A., RAVANI, S., ROMANO, R., *Imaging features that discriminate between foci induced by high-and low-LET radiation in human fibroblasts*. Radiation research **165** (2006) 505-515
- DATZMANN, G., DOLLINGER, G., GOEDEN, C., HAUPTNER, A. *et al.*, *The Munich microprobe SNAKE: First results using 20 MeV protons and 90 MeV sulfur ions*. Nuclear Instruments and Methods in Physics Research B **181** (2001) 20-26
- DENECKER, G., VERCAMMEN, D., STEEMANS, M., BERGHE, V. T. *et al.*, *Death receptor-induced apoptotic and necrotic cell death: differential role of caspases and mitochondria*. Cell death and differentiation **8** (2001) 829
- DURANTE, M., LOEFFLER, J. , *Charged particles in radiation oncology*. Nat. Rev. Clin. Oncol. **7** (2010) 37–43
- ECCLES, L., O'NEILL, P., LOMAX, M., *Delayed repair of radiation induced clustered DNA damage: friend or foe?* Mutation Research/Fundamental and Molecular Mechanisms of Mutagenesis **711** (2011) 134-141
- ELSÄSSER, T., KRÄMER, M., SCHOLZ, M., *Accuracy of the local effect model for the prediction of biologic effects of carbon ion beams in vitro and in vivo*. Int. J. Radiation Oncology Biol. Phys. **71** (2008) 866-872
- ELSÄSSER, T., WEYRATHER, W., FRIEDRICH, T., *Quantification of the relative biological effectiveness for ion beam radiotherapy: Direct experimental comparison of proton and carbon ion beams and a novel approach for treatment planning* Int. J. Radiation Oncology Biol. Phys. **78** (2010) 1177-1183
- ERIKSSON, D., STIGBRAND, T., *Radiation-induced cell death mechanisms*. Tumor Biology **31** (2010) 363-372
- FIGLIORE, M., DEGRASSI, F., *Dimethyl sulfoxide restores contact inhibition-induced growth arrest and inhibits cell density-dependent apoptosis in hamster cells*. Experimental Cell Research **251** (1999) 102-110
- FRANKEN, N. A., RODERMOND, H. M., STAP, J., HAVEMAN, J. *et al.*, *Clonogenic assay of cells in vitro*. Nat Protoc **1** (2006) 2315-9
- FRIEDLAND, W., SCHMITT, E., KUNDRÁT, P., DINGFELDER, M. *et al.*, *Comprehensive track-structure based evaluation of DNA damage by light ions from radiotherapy-relevant energies down to stopping*. Scientific Reports **7** (2017) 45161

- FRIEDRICH, T., DURANTE, M., SCHOLZ, M., *Simulation of DSB yield for high LET radiation* Radiation protection dosimetry (2015) 1-5
- FRIEDRICH, T., ILICIC, K., GREUBEL, C., GIRST, S. *et al.*, *DNA damage interaction on both nanometer and micrometer scale determine overall cellular damage.* (Submitted)
- FRIEDRICH, T., SCHOLZ, U., ELSÄSSER, T., DURANTE, M. *et al.*, *Calculation of the biological effects of ion beams based on the microscopic spatial damage distribution pattern.* International Journal of Radiation Biology (2012)
- FRIT, P., BARBOULE, N., YUAN, Y., GOMEZ, D. *et al.*, *Alternative end-joining pathway (s): Bricolage at DNA breaks.* DNA repair (2014)
- GERELCHULUUN, A., MANABE, E., ISHIKAWA, T., SUN, L. *et al.*, *The Major DNA Repair Pathway after Both Proton and Carbon-Ion Radiation is NHEJ, but the HR Pathway is More Relevant in Carbon Ions.* Radiation Research **183**, (2015) 345–356
- GOODHEAD, D., NIKJOO, H., *Track structure analysis of ultrasoft X-rays compared to high- and low-LET radiations.* International journal of radiation biology **55** (1989) 513-529
- GOODHEAD, D. T., *Energy deposition stochasticity and track structure: What about the target?* Radiation Protection Dosimetry **122** (2006) 3-15
- GOODHEAD, D. T., *Initial events in the cellular effects of ionizing radiations: clustered damage in DNA.* International journal of radiation biology **65** (1994) 7-17
- GOTO, S., WATANABE, M., YATAGAI, F., *Delayed cell cycle progression in human lymphoblastoid cells after exposure to high-LET radiation correlates with extremely localized DNA damage.* Radiation research **158** (2002) 678-686
- GREUBEL, C., HABLE, V., DREXLER, G. A., HAUPTNER, A. *et al.*, *Quantitative analysis of DNA-damage response factors after sequential ion microirradiation.* Radiation and environmental biophysics **47** (2008) 415-422
- GREUBEL, C., ILICIC, K., RÖSCH, T., REINDL, J. *et al.*, *Low LET proton microbeam to understand high-LET RBE by shaping spatial dose distribution.* Nuclear Instruments and Methods in Physics Research Section B: Beam Interactions with Materials and Atoms **404** (2017) 155-161
- GUDKOV, A., KOMAROVA, E., *The role of p53 in determining sensitivity to radiotherapy.* Nature reviews. Cancer **3** (2003) 117-129

- HABERMEHL, D., ILICIC, K., DEHNE, S., RIEKEN, S. *et al.*, *The Relative Biological Effectiveness for Carbon and Oxygen Ion Beams Using the Raster-Scanning Technique in Hepatocellular Carcinoma Cell Lines*. PLOS ONE **9** (2014) e113591
- HABLE, V., GREUBEL, C., BERGMAIER, A., REICHART, P. *et al.*, *The live cell irradiation and observation setup at SNAKE*. Nuclear Instruments and Methods in Physics Research Section B: Beam Interactions with Materials and Atoms **267** (2009) 2090-2097
- HADA, M., GEORGAKILAS, A., *Formation of clustered DNA damage after high-LET irradiation: a review*. Journal of radiation research **49** (2008) 203-210
- HALL, E. J., GIACCIA, A. J., *Radiobiology for the Radiologist*. Philadelphia, USA, Lippincott Williams & Wilkins (2006).
- HAUPTNER, A., DIETZEL, S., DREXLER, G. A., REICHART, P. *et al.*, *Microirradiation of cells with energetic heavy ions*. Radiat Environ Biophys **42** (2004) 237-45
- HAUPTNER, A., KRUCKEN, R., GREUBEL, C., HABLE, V. *et al.*, *DNA-repair protein distribution along the tracks of energetic ions*. Radiat Prot Dosimetry **122** (2006) 147-9
- HEILMANN, J., TAUCHER-SCHOLZ, G., HABERER, T., *Measurement of intracellular DNA double-strand break induction and rejoining along the track of carbon and neon particle beams in water*. Int. J. Radiation Oncology Biol. Phys. **34** (1996) 599-608
- HILL, M. A., GRIFFIN, C. S., PYKE, E. L., STEVENS, D. L., *Chromosome aberration induction is dependent on the spatial distribution of energy deposition through a cell nucleus*. Radiation protection dosimetry **143** (2011) 172-176
- HOLGERSSON, A., JERNBERG, R. M. A., PERSSON, L. M., EDGREN, M. R. *et al.*, *Low and high LET radiation-induced apoptosis in M059J and M059K cells*. International journal of radiation biology (2003) 611-621
- HU, T., MILLER, C., RIDDER, G., AARDEMA, M., *Characterization of p53 in Chinese hamster cell lines CHO-K1, CHO-WBL, and CHL: implications for genotoxicity testing*. Mutation Research **426** (1999) 51-62
- IAEA, *Relative Biological Effectiveness in Ion Beam Therapy*. IAEA, Technical reports series (2008)
- ILIAKIS, G., MURMANN, T., SONI, A., *Alternative end-joining repair pathways are the ultimate backup for abrogated classical non-homologous end-joining and homologous recombination repair: Implications for the formation of chromosome translocations*.

- Mutation Research/Genetic Toxicology and Environmental Mutagenesis **793** (2015) 166-175
- IWADATE, Y., MIZOE, J. E., OSAKA, Y., YAMAURA, A. *et al.*, *High linear energy transfer carbon radiation effectively kills cultured glioma cells with either mutant or wild-type p53*. Int. J. Radiation Oncology Biol. Phys. **50** (2001) 803-808
- JAFFRAY, D. A., *Image-guided radiotherapy: from current concept to future perspectives*. Nat Rev Clin Oncol **9** (2012) 688-699
- JENNER, T., DELARA, C., O'NEILL, P., *Induction and rejoining of DNA double-strand breaks in V79-4 mammalian cells following  $\gamma$ - and  $\alpha$ -irradiation*. International Journal of Radiation Biology **64** (1993) 265-273
- KHANNA, K., JACKSON, S., *DNA double-strand breaks: signaling, repair and the cancer connection*. Nature genetics **27** (2001)
- KONISHI, T., TAKEYASU, A., YASUDA, N., *Number of Fe ion traversals through a cell nucleus for mammalian cell inactivation near the Bragg peak*. Journal of Radiation Research **46** (2005) 415-424
- KRAFT, G., *Tumor therapy with heavy charged particles*. Progress in Particle and Nuclear Physics **45** (2000) 473-544
- KRAFT, G., KRÄMER, M., SCHOLZ, M., *LET, track structure and models*. Radiation and environmental biophysics **31** (1992) 161-180
- KREIPL, M., FRIEDLAND, W., PARETZKE, H., *Interaction of ion tracks in spatial and temporal proximity*. Radiation and environmental biophysics **48** (2009) 349-359
- KRYSKO, D., BERGHE, T., D'HERDE, K., VANDENABEELE, P., *Apoptosis and necrosis: detection, discrimination and phagocytosis*. Methods **44** (2008) 205-221
- LAUBER, K., ERNST, A., ORTH, M., HERRMANN, M., *Dying cell clearance and its impact on the outcome of tumor radiotherapy*. Frontiers in Oncology **2** (2012)
- LEA, D., CATCHESIDE, D., *The mechanism of the induction by radiation of chromosome aberrations in Tradescantia*. Journal of genetics **44** (1942) 216-245
- LEATHERBARROW, E., HARPER, J., CUCINOTTA, F., O'NEILL, P., *Induction and quantification of  $\gamma$ -H2AX foci following low and high LET-irradiation*. International Journal of Radiation Biology **82** (2006) 111-118
- LOEFFLER, J., DURANTE, M., *Charged particle therapy—optimization, challenges and future directions*. Nat. Rev. Clin. Oncol. **10** (2013) 411–424

- LOMAX, M., FOLKES, L., O'NEILL, P., *Biological consequences of radiation-induced DNA damage: relevance to radiotherapy*. *Clinical Oncology* **25** (2013) 578-585
- MA, Y., LU, H., SCHWARZ, K., LIEBER, M. , *Repair of double-strand DNA breaks by the human nonhomologous DNA end joining pathway: the iterative processing model*. *Cell Cycle* **4** (2005) 1193-1200
- MACPHIL, S. H., BANATH, J. P., YU, Y., CHU, E. *et al.*, *Cell cycle-dependent expression of phosphorylated histone H2AX: reduced expression in unirradiated but not X-irradiated G1-phase cells*. *Radiation Research* **159** (2003) 759-767
- MAEDA, S., KIMURA, H., KOGA, N., LIN, K., SAITO, T., *Cell density-dependent DNA fragmentation and its suppression by heparin in primary culture of adult rat hepatocytes*. *Biochemical and biophysical research communications* **195** (1993) 270-275
- MARTINEZ, J. D., *Restoring p53 tumor suppressor activity as an anticancer therapeutic strategy*. *Future Oncol.* **6** (2010) 1857–1862
- MATT, S., HOFMANN, T., *The DNA damage-induced cell death response: a roadmap to kill cancer cells*. *Cellular and molecular life sciences* **73** (2016) 2829-2850
- MAVRAGANI, N., SOULI, AZIZ, NOWSHEEN, ROGAKOU AND GEORGAKILAS, *Complex DNA Damage: A Route to Radiation-Induced Genomic Instability and Carcinogenesis*. *Cancers* **9** (2017)
- MEIJER, KRONQVIST, LEWENSOHN, HARMIS-RINGDAHL, M., *RBE for the induction of apoptosis in human peripheral lymphocytes exposed in vitro to high-LET radiation generated by accelerated nitrogen ions*. *International Journal of Radiation Biology* **73** (1998) 169-177
- MLADENOV, E., ILIAKIS, G., *Induction and repair of DNA double strand breaks: the increasing spectrum of non-homologous end joining pathways*. *Mutation Research/Fundamental and Molecular Mechanisms of Mutagenesis* **711** (2011) 61-72
- MORI, E., TAKAHASHI, A., YAMAKAWA, N., KIRITA, T. *et al.*, *High LET heavy ion radiation induces p53-independent apoptosis*. *Journal of radiation research* **50** (2009) 37-42
- NAKAGAWA, Y., TAKAHASHI, A., KAJIHARA, A., YAMAKAWA, N. *et al.*, *Depression of p53-independent Akt survival signals in human oral cancer cells bearing mutated p53 gene after exposure to high-LET radiation*. *Biochemical and biophysical research communications* **423** (2012) 654-660



- NEARY, G. J., *Chromosome aberrations and the theory of RBE: 1. General considerations.* International Journal of Radiation Biology and Related Studies in Physics, Chemistry and Medicine (1965)
- NIKJOO, H., O'NEILL, P., TERRISSOL, M., *Quantitative modelling of DNA damage using Monte Carlo track structure method.* Radiat Environ Biophys **38** (1999) 31-38
- OHNO, T., *Particle radiotherapy with carbon ion beams.* EPMA Journal **4** (2013) 9
- PAGANETTI, H., *Significance and implementation of RBE variations in proton beam therapy.* Technology in Cancer Research & Treatment **2** (2003)
- PAGANETTI, H., NIEMIERKO, A., ANCUKIEWICZ, M., *Relative biological effectiveness (RBE) values for proton beam therapy.* Int. J. Radiation Oncology Biol. Phys. **53** (2002) 407-421
- POLYAK, K., XIA, Y., ZWEIER, J. L., KINZLER, K. W. *et al.*, *A model for p53-induced apoptosis.* Nature **389** (1997)
- PUCK, T. T., MARCUS, P. I., *Action of x-rays on mammalian cells.* The Journal of experimental medicine **103** (1956)
- REINDL, J., DREXLER, G., GIRST, S., GREUBEL, C. *et al.*, *Nanoscopic exclusion between Rad51 and 53BP1 after ion irradiation in human HeLa cells.* Physical Biology **12** (2015) 066005
- REINDL, J., GIRST, S., WALSH, D., GREUBEL, C. *et al.*, *Chromatin organization revealed by nanostructure of irradiation induced  $\gamma$ H2AX, 53BP1 and Rad51 foci.* Scientific Reports **7** (2017)
- ROGAKOU, E. P., PILCH, D. R., ORR, A. H., IVANOVA, V. S. *et al.*, *DNA Double-stranded Breaks Induce Histone H2AX Phosphorylation on Serine 139.* The Journal of Biological Chemistry **273** (1998) 5858-5868
- ROOS, W., KAINA, B., *DNA damage-induced cell death: from specific DNA lesions to the DNA damage response and apoptosis.* Cancer letters **332** (2013) 237-248
- ROTHKAMM, K., LÖBRICH, M., *Evidence for a lack of DNA double-strand break repair in human cells exposed to very low x-ray doses.* PNAS **100** (2003) 5057-5062
- SAEKI, K., YUO, A., KATO, M., MIYAZONO, K., YAZAKI, Y., *Cell density-dependent apoptosis in HL-60 cells, which is mediated by an unknown soluble factor, is inhibited by transforming growth factor  $\beta$ 1 and overexpression of Bcl-2.* Journal of Biological Chemistry **272** (1997) 20003-20010

- SANCAR, A., LINDSEY-BOLTZ, L. A., ÜNSAL-KAÇMAZ, K., LINN, S., *Molecular mechanisms of mammalian DNA repair and the DNA damage checkpoints*. Annual Review of Biochemistry **73** (2004) 39-85
- SCHARDT, D., ELSÄSSER, T., SCHULZ-ERTNER, D., *Heavy-ion tumor therapy: physical and radiobiological benefits*. Reviews of modern physics **82** (2010)
- SCHIPLER, A., ILIAKIS, G., *DNA double-strand-break complexity levels and their possible contributions to the probability for error-prone processing and repair pathway choice*. Nucleic acids research **41** (2013) 7589-7605
- SCHMID, T., DOLLINGER, G., BEISKER, W., HABLE, V., GREUBEL, C., AUER, S., MITTAG, A., TARNOK, A., FRIEDL, A., MOLLS, M., RÖPER, B., *Differences in the kinetics of gamma-H2AX fluorescence decay after exposure to low and high LET radiation*. International Journal of Radiation Biology (2010)
- SCHMID, T. E., DOLLINGER, G., HABLE, V., GREUBEL, C. *et al.*, *The effectiveness of 20 MeV protons at nanosecond pulse lengths in producing chromosome aberrations in human-hamster hybrid cells*. Radiat Res **175** (2011a) 719-27
- SCHMID, T. E., DOLLINGER, G., HABLE, V., GREUBEL, C. *et al.*, *The effectiveness of 20 MeV protons at nanosecond pulse lengths in producing chromosome aberrations in human-hamster hybrid cells*. Radiation research **175** (2011b) 719-727
- SCHMID, T. E., DOLLINGER, G., HABLE, V., GREUBEL, C. *et al.*, *Relative biological effectiveness of pulsed and continuous 20 MeV protons for micronucleus induction in 3D human reconstructed skin tissue*. Radiotherapy and Oncology : Journal of the European Society for Therapeutic Radiology and Oncology **95** (2010) 66-72
- SCHMID, T. E., DOLLINGER, G., HAUPTNER, A., HABLE, V. *et al.*, *No evidence for a different RBE between pulsed and continuous 20 MeV protons*. Radiat Res **172** (2009) 567-74
- SCHMID, T. E., FRIEDLAND, W., GREUBEL, C., GIRST, S. *et al.*, *Sub-micrometer 20MeV protons or 45MeV lithium spot irradiation enhances yields of dicentric chromosomes due to clustering of DNA double-strand breaks*. Mutat Res Genet Toxicol Environ Mutagen **793** (2015) 30-40
- SCHMID, T. E., GREUBEL, C., HABLE, V., ZLOBINSKAYA, O. *et al.*, *Low LET protons focused to submicrometer shows enhanced radiobiological effectiveness*. Phys Med Biol **57** (2012a) 5889-907

- SCHMID, T. E., ZLOBINSKAYA, O., MULTHOFF, G., *Differences in Phosphorylated Histone H2AX Foci Formation and Removal of Cells Exposed to Low and High Linear Energy Transfer Radiation*. *Current Genomics* **13** (2012b) 418-425
- SCHOLZ, M. 2003. Effects of ion radiation on cells and tissues. *Radiation effects on polymers for biological use*. Springer, Berlin, Heidelberg.
- SCHOLZ, M., KELLERER, A, KRAFT-WEYRATHER, W., *Computation of cell survival in heavy ion beams for therapy*. *Radiat. Environ. Biophys.* **36** (1997) 59-66
- SCHOLZ, M., KRAFT, G., *Track structure and the calculation of biological effects of heavy charged particles*. *Advances in Space Research* **18** (1996) 5-14
- SCHULZ-ERTNER, D., TSUJII, H., *Particle Radiation Therapy Using Proton and Heavier Ion Beams*. *Journal of Clinical Oncology* **25** (2007) 953-964
- SHIBATA, A., CONRAD, S., BIRRAUX, J., GEUTING, V., *Factors determining DNA double-strand break repair pathway choice in G2 phase*. *The EMBO Journal* **30** (2011) 1079-1092
- SHRIVASTAV, M., HARO, DE L., NICKOLOFF, J., *Regulation of DNA double-strand break repair pathway choice*. *Cell research* **18** (2008) 134-147
- SILVA, M., *Secondary necrosis: the natural outcome of the complete apoptotic program*. *FEBS letters* **584** (2010) 4491-4499
- TAKAHASHI, A., MATSUMOTO, H., YUKI, K., YASUMOTO, J. I., *High-LET radiation enhanced apoptosis but not necrosis regardless of p53 status*. *Int. J. Radiation Oncology Biol. Phys.* **60** (2004) 591-597
- TAYLOR, POWELL, *Intensity-modulated radiotherapy—what is it?* *Cancer Imaging* **4** (2004) 68-73
- TSUCHIDA, Y., TSUBOI, K., OHYAMA, H., OHNO, T., NOSE, T., *Cell death induced by high-linear-energy transfer carbon beams in human glioblastoma cell lines*. *Brain Tumor Pathology* **15** (1998) 71-76
- TZANG, B., LAI, Y., HSU, M., CHANG, H., *Function and sequence analyses of tumor suppressor gene p53 of CHO. K1 cells*. *DNA and Cell Biology* **18** (1999)
- WARD, J. F., *Biochemistry of DNA lesions*. *Radiation research* (1985)
- WARD, J. F., *The complexity of DNA damage: relevance to biological consequences*. *International journal of radiation biology* **66** (1994) 427-432

WATSON, J., CRICK, F., *Molecular structure of deoxypentose nucleic acids*. Nature **171** (1953) 737-738

WEYRATHER, W. K., RITTER, S., SCHOLZ, M., KRAFT, G., *RBE for carbon track-segment irradiation in cell lines of differing repair capacity*. International journal of radiation biology **75** (1999) 1357-1364

WILSON, R. R., *Radiological Use of Fast Protons*. Radiology **47** (1946) 487-491

WYMAN, C., KANAAR, R., *DNA double-strand break repair: all's well that ends well*. Annu. Rev. Genet. **40** (2006) 363-383

## List of publications

### 2014

1. THE RELATIVE BIOLOGICAL EFFECTIVENESS FOR CARBON AND OXYGEN ION BEAMS USING THE RASTER-SCANNING TECHNIQUE IN HEPATOCELLULAR CARCINOMA CELL LINES. Habermehl D., **Ilicic K.**, Dehne S., Rieken S., Orschiedt L., Brons S., Haberer T., Weber K.J., Debus J., Combs S.E. PLOS ONE, 2014. 9(12).

### 2015

2. SUB-MICROMETER 20 MEV PROTONS OR 45 MEV LITHIUM SPOT IRRADIATION ENHANCES YIELDS OF DICENTRIC CHROMOSOMES DUE TO CLUSTERING OF DNA DOUBLE-STRAND BREAKS. Schmid T.E., Friedland W., Greubel C., Girst S., Reindl J., Siebenwirth C., **Ilicic K.**, Schmid E., Multhoff G., Schmitt E., Kunderát P., Dollinger G. Mutat Res Genet Toxicol Environ Mutagen, 2015. 793: p. 30-40.

3. ROLE OF MEMBRANE HSP70 IN RADIATION SENSITIVITY OF TUMOR CELLS. Murakami N., Kühnel A., Schmid T.E., **Ilicic K.**, Stangl S., Braun I.S., Gehrman M., Molls M., Itami J. and Multhoff G. Radiation Oncology, 2015. 10(149).

4. MAGNETIC HEATING PROPERTIES AND NEUTRON ACTIVATION OF TUNGSTEN-OXIDE COATED BIOCOMPATIBLE FEPT CORE-SHELL NANOPARTICLES. Seemann K.M., Luysberg M., Révay Z., Kudejova P., Sagué B.S., Cassinelli N., Loidl A., **Ilicic K.**, Multhoff G., Schmid T.E. Journal of Controlled Release, 2015. 197: p131–137.

## 2016

5. PROTON MINIBEAM RADIATION THERAPY REDUCES SIDE EFFECTS IN AN IN VIVO MOUSE EAR MODEL. Girst S., Greubel C., Reindl J., Siebenwirth C., Zlobinskaya O., Walsh D.W.M., **Ilicic K.**, Aichler M., Walch A., Wilkens J.J., Multhoff G, Dollinger G. and Schmid T.E. *International Journal of Radiation Oncology\* Biology\* Physics*, 2016. 96 (1): p234-241.

## 2017

6. LOW LET PROTON MICROBEAM TO UNDERSTAND HIGH-LET RBE BY SHAPING SPATIAL DOSE DISTRIBUTION. Greubel C., **Ilicic K.**, Rösch T., Reindl J., Siebenwirth C., Moser M., Girst S., Walsh D.W.M., Schmid T.E., Dollinger G. *Nuclear Instruments and Methods in Physics Research B*, 2017. 404: p155–161.

7. INCREASED CELL SURVIVAL AND CYTOGENETIC INTEGRITY BY SPATIAL DOSE REDISTRIBUTION AT A COMPACT SYNCHROTRON X-RAY SOURCE. Burger K., **Ilicic K.**, Dierolf M., Guenther B., Walsh D.W.M., Schmid E., Eggl E., Achterhold K., Gleich B., Combs S.E., Molls M., Schmid T.E., Pfeiffer f., Wilkens J.J. *PLoS ONE*, 2017. 12(10): e0186005.

8. LIVE CELL IMAGING OF MITOCHONDRIA FOLLOWING TARGETED IRRADIATION IN SITU REVEALS RAPID AND HIGHLY LOCALIZED LOSS OF MEMBRANE POTENTIAL. Walsh D.W.M., Siebenwirth C., Greubel C., **Ilicic K.**, Reindl J., Girst S., Muggiolu G., Simon M., Barberet P., Seznec H., Zischka H., Multhoff G., Schmid T.E. and Dollinger G. *Sci. Reports*, 2017. 7: 46684.

9. NEW INSIGHTS IN THE RELATIVE RADIOBIOLOGICAL EFFECTIVENESS OF PROTON IRRADIATION. **Ilicic K.**, Combs S.E., Schmid T.E. *Radiation Oncology* (Under review).

10. DNA DAMAGE INTERACTION ON BOTH NANOMETER AND MICROMETER SCALE DETERMINE OVERALL CELLULAR DAMAGE. Friedrich T., **Ilicic K.**, Greubel C., Girst S., Reindl J., Sammer M., Schwarz B., Siebenwirth C., Walsh D.W.M., Schmid T.E., Scholz M., Dollinger G. Manuscript in preparation





## Appendix

### Eidesstattliche Erklärung

Ich erkläre an Eides statt, dass ich die bei der Fakultät Wissenschaftszentrum Weihenstephan für Ernährung, Landnutzung und Umwelt (WZW) der Technischen Universität München zur Promotionsprüfung vorgelegte Arbeit mit dem Titel: “The cellular responses to focused low LET proton irradiation in comparison to high LET irradiation” am Lehrstuhl für Experimentelle Radioonkologie und Strahlentherapie am Klinikum rechts der Isar der TU München unter der Anleitung und Betreuung durch Prof. Dr. Gabriele Multhoff ohne sonstige Hilfe erstellt und bei der Auffassung nur die gemäß § 6 Abs. 6 und 7 Satz 2 angegebenen Hilfsmittel benutzt habe.

Ich habe keine Organisation eingeschaltet, die gegen Entgelt Betreuerinnen und Betreuer für die Anfertigung von Dissertation sucht, oder die mir obliegenden Pflichten hinsichtlich der Prüfungsleistungen für mich ganz oder teilweise erledigt.

Ich habe die Dissertation in dieser oder ähnlicher Form in keinem anderen Prüfungsverfahren als Prüfungsleistung vorgelegt.

Ich habe den angestrebten Doktorgrad noch nicht erworben und bin nicht in einem früheren Promotionsverfahren für den angestrebten Doktorgrad endgültig gescheitert.

Die öffentlich zugängliche Promotionsordnung der TUM ist mir bekannt, insbesondere habe ich die Bedeutung von § 28 (Nichtigkeit der Promotion) und § 29 (Entzug des Doktorgrades) zur Kenntnis genommen.

Ich bin mir der Konsequenzen einer falschen Eidesstattlichen Erklärung bewusst. Mit der Aufnahme meiner personenbezogenen Daten in die Alumni-Datei bei der TUM bin ich einverstanden.

München, den \_\_\_\_\_

\_\_\_\_\_  
Katarina Ilicic



## **Acknowledgments**

At this point, I want to express special gratitude to Prof. Dr. Gabriele Multhoff, for her interest in my work and for undertaking the supervision of the PhD work.

I greatly acknowledge Prof. Angelika Schnieke and Prof. Dr. Johann J. Hauner for undertaking the function of the co- examiner and the chairman of the examining board.

I am especially thankful to PD Dr. Thomas Schmid for giving me the opportunity to work in his group and for his excellent guidance. He was always willing to discuss results and give advices.

I thank Prof. Dr. Günther Dollinger for his great ideas, valuable discussions and his infectious enthusiasm for the research. I also thank Dr. Christoph Greubel, for being not only the physicist but also the statistician in our research project and especially for his patience when explaining me the world of physics.

I am grateful to my fellow PhD student Dieter Walsh for his continuous support during my PhD work, for pleasant lunch hours and fruitful discussions. He made all these long evenings and nights during the beam times bearable. A big “thank you” to all current and former physics group members for performing the irradiation experiments, especially to Judith Reindl for organizing and coordinating the beam times. I also thank our biology group members to share a nice time in good atmosphere. I appreciate skillful help from Andrea Mair and Marlon Stein for helping me before / during / after the beam times and for the good atmosphere in the lab.

I am thankful to our collaborators Dr. Michael Scholz, Dr. Thomas Friedrich, Dr. Werner Friedland, and Dr. Pavel Kundrat for long but very precious discussions. I really liked working on this interdisciplinary research project and I also enjoyed our LET meetings very much.

Also many thanks to my dear friend Aicha, who supported me and cheered me up!

Special thanks to my parents, my brother Marko and my sister- in-law Despina: For your continuous support and encouragement during the last years and for being always there for me. The greatest thanks of all go to my husband Ivan, for his patience, encouragement and his unconditional love. Sretna sam sto Vas imam!



## Curriculum vitae

Katarina Ilicic

Department of Radiation Oncology  
Technische Universität München (TUM)  
Klinikum rechts der Isar  
Ismaninger Str. 22  
D-81675 München  
Mail: katarina.ilicic@tum.de

\* 08. November 1987 in Vinkovci, Croatia

### School education

---

Jun 2007 Abitur (final exams) at the Maria-Theresia school, Munich, Germany

Advanced courses in biology, mathematics and german

### University education

---

Oct 2007 – Sep 2011      Bachelor of Science degree in Biology, Ludwig Maximilians  
University Munich (LMU)

Title of Bachelor`s thesis: *Untersuchung der Effekte auf  
Zellmetabolismus und Zellmorphologie durch Blockieren von  
Na<sup>+</sup>/H<sup>+</sup>-Antiportern der Zellmembran durch Messungen an  
einem neuen Sensor-basierten Testsystem*

Oct 2011 – Oct 2012      Master of Science degree in Biology, Ludwig Maximilians  
University Munich (LMU)

Title of Masters` thesis: *Analyse von Veränderungen der  
mitochondriellen und glykolytischen Aktivität primärer  
Lymphozyten unter Einfluß von Zytokinen und unterschiedlicher  
Glukosekonzentrationen*

## **Professional career**

---

- |                     |   |
|---------------------|---|
| Jul 2013 – May 2017 | PhD student at Department of Radiation Oncology, Klinikum rechts der Isar, Munich, Germany          |
| Since June 2017     | Scientific Assistant at Department of Radiation Oncology, Klinikum rechts der Isar, Munich, Germany |

## **Awards & Grants**

---

- |           |   |
|-----------|---|
| July 2017 | Travel Award ERRS/GBS 2017, Essen Germany   |
| May 2015  | Young Investigators Travel Award ICRR 2015, Kyoto Japan   |
| Feb 2015  | Reisestipendium 24. Symposium Experimentelle Strahlentherapie und Klinische Strahlenbiologie, Hamburg Germany |

